Journal of Electron Spectroscopy and Related Phenomena 178–179 (2010) 2–32

Contents lists available at ScienceDirect

Journal of Electron Spectroscopy and Related Phenomena

journal homepage: www.elsevier.com/locate/elspec

X-ray photoelectron spectroscopy: Progress and perspectives

C.S. Fadley[a,b,*]

[a] Department of Physics, University of California, Davis, CA 95616, USA
[b] Materials Sciences Division, Lawrence Berkeley National Laboratory, Berkeley,CA 94720, USA

ARTICLE INFO

Article history:
Available online 4 February 2010

Keywords:
X-ray photoelectron spectroscopy
Photoemission
XPS
Photoelectron diffraction
Photoelectron holography
Angle-resolved photoemission
ARPES
Synchrotron radiation

ABSTRACT

In this overview, I will briefly explore some of the basic concepts and observable effects in X-ray photoelectron spectroscopy, including references to some key first publications, as well as other papers in this issue that explore many of them in more detail. I will then turn to some examples of several present and promising future applications of this diverse technique. Some of the future areas explored will be the use chemical shifts, multiplet splittings, and hard X-ray excitation in the study of strongly correlated materials; photoelectron diffraction and holography for atomic structure determinations; standing wave and hard X-ray excited photoemission for probing buried interfaces and more bulk-like properties of complex materials; valence-band mapping with soft and hard X-ray excitation; and time-resolved measurements with the sample at high ambient pressures in the multi-torr regime.

1. Introduction

X-ray photoelectron spectroscopy (XPS or ESCA) of course owes its quantification to Einstein's explanation of the photoelectric effect in 1905 [1], and the technique in fact has a long history that can be traced to contemporary measurements in which either X-rays or gamma rays were used to excite photoelectrons from solids [2]. In the period since the late 1950s, the photoelectric effect has been developed into one of our most powerful tools for studying the composition and electronic structure of matter, with Kai Siegbahn receiving the Nobel Prize in 1981 for the development of high-resolution XPS. His group's early pioneering work is documented in the two well-known ESCA books [3,4], with many other reviews and overviews appearing later [e.g. [5–8]. There has been much progress in the intervening decades, and new modes of measurement and more precise theoretical interpretation methodologies continue to be developed, with many of these being discussed in the other articles in this issue.

In this article, I will make brief reference to the history of various measurement modes and effects, but focus primarily on some of the most recent developments, pointing to more detailed discussions elsewhere as appropriate, and attempting in some cases to speculate on future interesting directions that have yet to be exploited. I will also focus on measurements of condensed matter phases (solids, surfaces, interfaces, and to some degree liquids [9]), the most interesting domain for basic and applied scientists using XPS. As a convenient operational definition of XPS, I will consider excitation energies above a few hundred eV and going into the hard X-ray regime up to 15 keV. Thus, both core levels and valence levels are readily observable in spectra. The topics considered will reflect to a certain degree my own personal biases, but, together with the other articles in this issue, I believe the reader will have access to a very thorough overview of the current status of XPS, as well as of some of the most exciting directions for its future.

2. Some basic considerations:

Fig. 1 illustrates in a schematic way some of the most important aspects of the XPS experiment, including some new directions of development. These will be discussed in subsequent paragraphs.

As an additional important starting point for quantification, the fundamental energy conservation equation in photoemission is the following [5–8]:

$$h\nu = E_{binding}^{Vacuum} + E'_{kinetic} + V_{charge} + V_{bias}$$
$$= E_{binding}^{Fermi} + \varphi_{spectrometer} + E_{kinetic} + V_{charge} + V_{bias} \quad (1)$$

in which h is Planck's constant; ν is the photon frequency; $E_{binding}^{Vacuum}$ is the binding energy of a given electron relative to the vacuum level of the sample; $E'_{kinetic}$ is the kinetic energy of the emitted electron just as it leaves the sample; $E_{kinetic}$ is the kinetic energy as measured finally in the spectrometer, which may be different from $E'_{kinetic}$ by a small contact potential difference if the sample is a solid; $E_{binding}^{Fermi}$ is the binding energy relative to the Fermi level or electron chemical

* Correspondence address: Department of Physics, University of California, Davis, CA 95616, USA. Tel.: +1 530 752 8788; fax: +1 530 752 4717.
E-mail address: fadley@physics.ucdavis.edu.

0368-2048/$ – see front matter © 2010 Elsevier B.V. All rights reserved.
doi:10.1016/j.elspec.2010.01.006

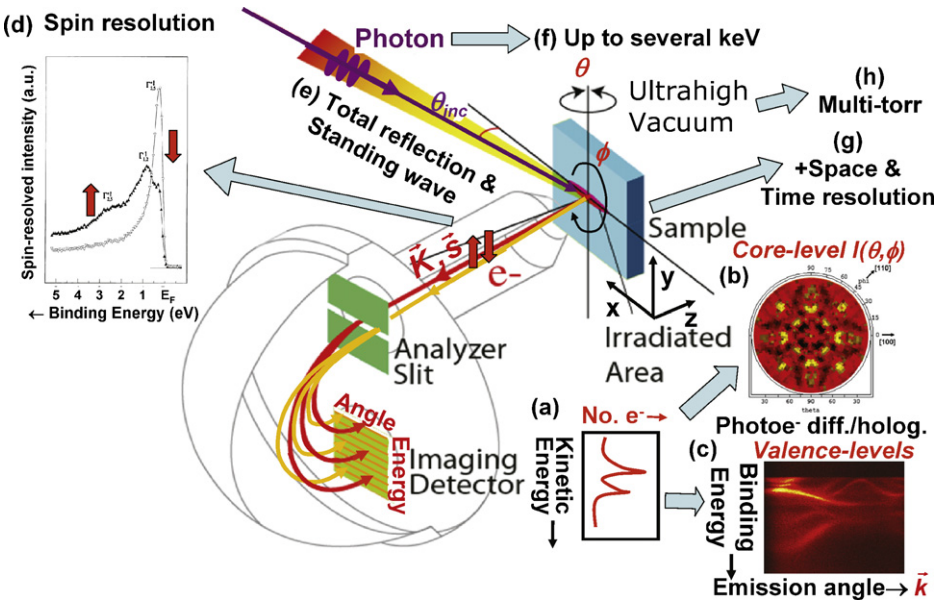

Fig. 1. Illustration of a typical experimental configuration for X-ray photoelectron spectroscopy experiments, together with the various types of measurements possible, including (a) simple spectra or energy distribution curves, (b) core-level photoelectron diffraction, (c) valence-band mapping or binding energy vs $\vec{k}$ plots, (d) spin-resolved spectra, (e) exciting with incident X-rays such that there is total reflection and/or a standing wave in the sample, (f) using much higher photon energies than have been typical in the past, (g) taking advantage of space and/or time resolution, and (h) surrounding the sample with high ambient sample pressures of several torr (with acknowledgement to Y. Takata for part of this figure).

potential; $\varphi_{spectrometer}$ is the work function of the spectrometer used to measure kinetic energy, V_{charge} is a possible charging potential on the sample that may build up if the emitted photoelectron and secondary electron current is not fully compensated by flow from the sample ground, and V_{bias} is a time-dependent bias potential that may be placed between the sample and the spectrometer, here with sign such that a positive bias acts to slow the photoelectrons. The effects of charging are discussed elsewhere in this issue by Cazaux. In very precise measurements, and/or as the excitation energy is increased into the multi-keV regime, both kinetic energies will be reduced by a recoil energy E_{recoil} imparted to the sample due to momentum conservation [4], with this often being negligible in typical XPS applications, but affecting both core and valence-band emission significantly as excitation energies are increased into the multi-keV regime [10]. E_{recoil} can be estimated from:

$$E_{recoil} \approx \frac{\hbar^2 k_f^2}{2M} \approx 5.5 \times 10^{-4} \left[\frac{E_{kin}(\text{eV})}{M(\text{amu})}\right],$$

where $\hbar$ has the usual meaning, k_f is the final photoelectron wave vector, and M is the effective mass of the atom(s) involved.

If one measures the electron kinetic energy, and perhaps also knows the spectrometer work function, it is thus possible to measure the binding energies of various inner (or core) electrons, as well as those of the outer (or valence) electrons that are involved in chemical bonding. Such measurements have been found to reveal a broad array of phenomena that can be used to characterize a given material, in particular the near-surface regions of solids from which most photoelectrons are emitted. Adding a bias potential, including one with time dependence V_{bias} (t), has also been found useful for determining the conductivity and dielectric properties of the sample, as discussed elsewhere in this issue by Süzer et al.

Many papers to date have explored the effects of charging in XPS and in fact a dedicated issue of this journal has recently been devoted to this [11]. Beyond this, a few papers have considered more quantitatively the space charge and image potential effects near surfaces on binding energies and peak widths [12–14], which emerge as a serious consideration as to the realm of applicability of future ultrahigh-brightness sources such as free-electron lasers in photoemission. These papers have demonstrated the general systematics of these effects [12,13], including detailed theoretical modelling [14]. As one example of the limitations uncovered in this work [14], it is concluded that, if the optimum case of metal core levels are to be studied with less than 50 meV resolution, the number of low-energy "cloud" electrons emitted per ultrashort excitation pulse (with the pulse assumed to be shorter than the time for the cloud electrons to significantly disperse and/or be neutralized) must be less than 10,000 e^-/mm spot diameter. Assuming that the low-energy cloud electrons are the dominant source of current, the number per pulse can be estimated simply by dividing the total sample current by the number of pulses per second. The criterion stated above thus implies that an increased number of photons per pulse and/or a highly focussed beam will exaggerate the energy broadening problem. Possible ways to get around this limitation so as to carry out XPS with these high-brightness sources are to increase the repetition rate of the pulses, from the ca. 5 Hz of the FLASH FEL source in Hamburg today [15] into the MHz regime, with the photons per pulse then decreasing by possibly ca. 10^{-5} for the same time-integrated number of photons. Defocussing the beam so as to spread the photons over a wider area would also help. By working with higher harmonics that have significantly lower photons per pulse, such effects can be reduced, while also having the advantage of moving up into the soft X-ray regime for a vuv-regime FEL. And of course, making use of a spectrometer that records a maximum energy and solid angle range for each pulse, as e.g. via time-of-flight would assist as the final stage of the measurement. Taking advantage of all of these possibilities will certainly leave some region of experimental space for high-resolution XPS with FEL excitation, and with exciting future possibilities. Sample damage due to the radiation is a consideration beyond space charge effects, however, with one solution to this being to raster the sample in front of the beam. But such damage will be very sample specific, and should be studied for each individual case, e.g. by somehow varying the effective number of photons per pulse over a large dynamic range.

It is also useful to specify the binding energy more precisely from the point of view of theoretical calculations, and we can write this as:

$$E_{binding}^{Vacuum}(Qn\ell j, K) = E_{final}(N-1,\ \ Qn\ell\, j\, hole, K) - E_{initial}(N), \qquad (2)$$

where we for simplicity consider a binding energy for the $n\ell j$ core level from atom Q, with n the principal quantum number, ℓ the orbital angular momentum quantum number, and $j = \ell \pm 1$ the additional quantum number if spin–orbit splitting is present, $E_{kinetic}\ (N)$ is the total initial state energy for the assumed N-electron system, and $E_{final}(N-1,\ \ Qn\ell j\, hole, K)$ is the Kth final-state energy for the $(N-1)$-electron system with a hole in the $Qn\ell j$ orbital. As an example, the six electrons in the Mn 2p subshell are split into Mn $2p_{1/2}$ (two electrons with $m_j = -1/2, +1/2$) and Mn $2p_{3/2}$ (four electrons with $m_j = -3/2, -1/2, +1/2, +3/2$). In general, there may be more than one final state associated with a given $Qn\ell j$ hole, with labels $K = 1, 2, \ldots$, as we discuss further below, e.g. in connection with multiplet splitting. Note also that, in the final state with the hole, all of the remaining electrons may relax slightly so as to try to screen the hole, thus lowering the total final energy by some amount that is often called the relaxation energy [5,6]. In many cases, this screening can also take the form of a change in orbital occupation numbers, with resulting configuration interaction in the final state. I return to discuss these effects briefly below. This relaxation/screening phenomenon has many consequences for the detailed interpretation of spectra. In many-electron theory, these effects are included in what is termed the "self-energy" correction, and accurate methods for calculating binding energy are discussed in the article by Olovsson et al. in this issue.

Beyond measuring photoelectron energies, the intensity of each peak or feature is of critical importance in most uses of XPS. A much-used approach for calculating and using photoelectron intensities from both core and valence levels is the so-called three-step model [5,6] which divides the process into three steps of: (1) penetration of the exciting photon beam into the surface, with some resulting intensity profile $I_{h\nu}(x, y, z)$ and the coordinates defined in Fig. 1, and excitation of photoelectrons from each atom in the sample that are located at various depths z, which will be proportional to the differential photoelectric cross-section of the particular level $Qn\ell j$ of atom Q involved (e.g. Mn $2p_{1/2}$ and Mn $2p_{3/2}$), written as $d\sigma_{Qn\ell j}(h\nu, \hat{\varepsilon})/d\Omega$ and dependent on photon energy, radiation polarization $\hat{\varepsilon}$, and the experimental geometry; (2) transport of the photoelectron from depth z to the surface, which involves inelastic attenuation via an inelastic mean free path Λ_e, as well as elastic scattering and diffraction; and (3) escape from the surface, which involves refraction and reflection at the surface barrier, with these effects being controlled by the inner potential V_0 having typical values of 5–15 eV, and possible surface inelastic scattering, as well as elastic scattering and diffraction (surface umklapp processes). In general, $d\sigma_{Qn\ell j}(h\nu, \hat{\varepsilon})/d\Omega$ is a maximum near threshold, when the photon energy is equal to $E_{binding}^{Vacuum}(Qn\ell j)$, and steadily decreases as the energy increases, although it may not reach a maximum until some distance above threshold, and it may also exhibit local minima called Cooper minima for energies not too far above threshold [5,16]. Neglecting elastic scattering and surface refraction in crossing the inner potential surface barrier V_0 for simplicity, one can finally calculate a core-level intensity from:

$$I(Qnlj) = C\int_0^\infty I_{h\nu}(x,y,z)\rho_Q(x,y,z)\frac{d\sigma_{Qn\ell j}(h\nu,\hat{\varepsilon})}{d\Omega}$$
$$\exp\left[-\frac{z}{\Lambda_e \sin\theta}\right]\Omega(h\nu,x,y)dxdydz, \qquad (3)$$

where C is a constant characteristic of the experimental geometry, $\rho_Q(x, y, z)$ is the density of atomic type Q at positions x, y, z, and $\Omega(h\nu, x, y)$ is the solid angle of acceptance of the spectrometer for a given photon energy (or equivalently electron kinetic energy) and positions x, y on the sample surface. In principle, $I_{h\nu}(x, y, z)$ can be calculated from a knowledge of the source beam spot profile, the incidence angle, and the X-ray indices of refraction of the substances in the sample [17]; $d\sigma_{Qn\ell j}(h\nu, \hat{\varepsilon})/d\Omega$ can be calculated from atomic theory, and its evaluation requires knowing the polarization of the exciting radiation [16,18–20], Λ_e can either be taken from tabulations of experimental and calculated data [21] or estimated from semi-empirical formulas, as e.g. the much-used TPP-2M formula [22,23]; and $\Omega(h\nu, x, y)$, which is equivalent once integrated over x and y to the spectrometer intensity response function or transmission, can be determined from reference-sample calibration measurements [24]. For excitation energies in the keV regime, if not even below this, non-dipole or retardation corrections are needed for a fully accurate description of $d\sigma_{Qn\ell j}(h\nu, \hat{\varepsilon})/d\Omega$, as first demonstrated by Krause [25], and discussed in much more detail elsewhere [26]. Ultimately, it is in principle possible to measure $I(Qnlj)$ and determine the only remaining unknown $\rho_Q(x, y, z)$, which amounts to a quantitative chemical analysis of the sample. These form the basic core of quantitative surface analysis by XPS, but with many prior papers and recent reviews pointing out significant additional considerations in achieving the most accurate results, as e.g. including the effects of elastic scattering and electron refraction [22,23,27–29]. These more accurate approaches are discussed elsewhere in this issue by Powell and Jablonski, and Werner. These methods also include attempts to create expert systems for analyzing XPS data that minimize the need for operator intervention and resulting subjectivity, as discussed by Castle in this issue.

It is also worth noting here that, if the X-ray incidence angle is such that a significant degree of reflection results, either by being near the critical angle for one of the interfaces in the sample or being near the Bragg angle for reflection from a set of crystal planes or a multilayer mirror, the form of $I_{h\nu}(x, y, z)$ can be significantly altered, as indicated in Fig. 1(e), and discussed further below. The interference of incident and reflected waves will create a standing wave above the surface and/or inside the sample. And if one goes well below the critical angle, the penetration depth of the radiation is also drastically reduced, resulting in what has been termed total reflection XPS (TRXPS) or grazing-incidence XPS (GIXPS), a technique for enhancing the signal from the surface region and reducing the inelastic background underneath spectra [30]: this is reviewed elsewhere in this issue by Kawai. The presence of X-ray reflectivity, even at the 1% level, will create a significant standing wave modulation of the exciting radiation, thus providing additional depth sensitivity that has been used to determine surface atomic positions [31]; resolve valence densities of states into their element-specific components [32], as discussed by Zegenhagen in this issue; or determine depth profiles in nanometer-scale layered structures [33], as discussed in more detail later in this article.

Turning again to Fig. 1, we can describe the XPS measurement as starting when a photon with variable polarization is incident on the sample surface at some angle θ_{inc}. Photons in the XPS regime can be generated from either laboratory sources (X-ray tubes or higher harmonic generating laser sources), or synchrotron radiation. The photon is absorbed, exciting a photoelectron into the vacuum with some momentum $\vec{p} = \hbar\vec{k}$, where $\vec{k}$ is the electron wave vector, and $\vec{s}$ is the electron spin, and finally into some kind of spectrometer for measuring kinetic energy. The energy of the photoelectron inside the surface is greater by the inner potential V_0, such that the wave vector $\vec{k}$ outside is somewhat smaller in magnitude, and perhaps of slightly different direction due to refraction, if compared to the wave vector $\vec{k}$ inside the surface.

In Fig. 1, I show the most commonly used spectrometer configuration, which consists of a set of concentric hemispherical deflection electrodes and adjustable slits to regulate both source

size and angular acceptance [34], although several other geometries are possible, including time-of-flight measurements if the exciting source is pulsed. In this hemispherical geometry, electrons of a given energy are focussed to a given radius (i.e. along a given y coordinate in the detection plane of Fig. 1), such that integrating intensity over a given radius yields the first type of measurement: a photoelectron spectrum of number of electrons vs kinetic energy or energy distribution curve (EDC), as shown schematically in Fig. 1(a). Alternate modes of operating the retarding lens in such a spectrometer permit resolving one of the electron emission angles along a two-dimensional detector, as shown in Fig. 1(b) [34]; this is the most common current method of recording angle-resolved photoemission (ARPES) from valence electronic states, a type of measurement that is now being extended into the soft and hard X-ray regime, as discussed below. The commercial instrument from Scienta based on this principal [34] has been used for most ARPES measurements to date, but other options are now on the market. Alternatively, by suitably choosing the voltages on the retarding lens, this second axis in the detector can be used to determine the y-axis position of origin of the electrons, providing a one-dimensional type of photoelectron microscopy that is also well established in commercial systems.

Other spectrometer configurations, including those with electron optical elements permitting direct two-dimensional angular resolution or two-dimensional photoelectron microscopy also exist [34–37]. These are available both as commercial products with resolutions down to a micron (1000 nm), and synchrotron radiation based instruments that can achieve about 20 nm resolution, but with the promise of 5–10 nm, if not less, in the near future. The additional information that such microscopes provide, particularly with synchrotron radiation as the excitation source, will certainly lead to enhanced applications of them in the future, and I will later show some results obtained with one such instrument. In other articles in this issue, Escher, Artyushkova, and Margaritondo review the current status of photoelectron microscopy with both laboratory sources and synchrotron radiation excitation. It has also been demonstrated that photoelectron microscopy can be carried out with hard X-ray excitation [38,39] and this will certainly be a future area of exploitation. I will also discuss later the possibility of adding the third vertical dimension to such microscope images by using standing wave excitation.

As a final basic consideration related to measuring peak intensities, the degree of non-linearity in the final detector system needs to be taken into account. Straightforward methods for measuring and correcting for non-linearity have been discussed [40,41], but it seems like these are not widely practiced or appreciated. In measurements made over a large dynamic range, as e.g. in tuning photon energy on and off a resonance absorption process, such non-linearities can alter the observed intensities appreciably [42], but even in more routine analytical XPS applications where peaks can still range in intensity over 1–2 orders of magnitude, these effects need to be corrected for. Probably the most linear detectors operating to rates of several MHz are individual channeltrons, but the more efficient multiplexing systems provided by microchannel plates backed by phosphor/CCD combinations, resistive anodes or cross-wires to achieve spatial information begin to saturate at ~1 MHz. Looking to the future, detectors going well beyond this and into the GHz regime are clearly needed to be able to handle even the electron fluxes of certain current sources (either laboratory XPS or high-brightness synchrotron radiation sources), not to mention the much brighter free-electron laser sources now beginning to be used. Although some development steps have been made in this direction, with a one-dimensional prototype detector actually having demonstrated performance into the GHz range [43], much more is needed. This is currently a significant bottleneck to the future development of XPS.

3. Electron inelastic scattering and surface vs bulk sensitivity

Of key importance in any photoemission experiment is the depth of sensitivity in a solid sample, which is controlled primarily by the photoelectron inelastic mean free path (IMFP) Λ_e, but also with significant modifications due to elastic electron scattering and surface escape to yield an effective attenuation length [22], as discussed by Powell and Jablonski in this issue. If inelastic scattering is assumed to be isotropic in the material, and these other effects are neglected, the intensity from a certain emission depth z will decay as $I(z) = I_0 \exp[-z/\Lambda_e \sin\theta]$, where θ is the takeoff angle with respect to the surface and the mean escape depth below a surface will be given simply by $\Lambda_e \sin\theta$. Although this is an oversimplification of the physics, as discussed by Powell and Jablonski, and Werner elsewhere in this issue, there is in general a monotonic decrease in emission depth with decreasing takeoff angle that can be used both qualitatively and quantitatively to study the depth distributions of species near surfaces. This variation of mean depth has resulted in angle-resolved XPS (ARXPS) by now being a widely used method in surface and interface science method for selectively varying depth sensitivity and deriving concentration profiles of different species [28]. Various methods of analyzing ARXPS data now exist, ranging from the qualitative to the quantitative, with each having what are often conflicting advantages of simplicity vs accuracy [28]. These are reviewed in detail elsewhere in this issue by Powell and Jablonski, Werner, and Brundle.

As a useful summary of the variation of IMFP with kinetic energy, Fig. 2 shows a recent compilation of values calculated using the TPP-2M formula for 41 elemental solids [23]. The well-known form of these curves, with a minimum between roughly 20 and 100 eV, a general increase on going above this to higher energies, and a less pronounced increase on going to energies below the minimum, is a critical ingredient in the analysis of XPS data. The IMFP increases above 1 keV roughly as $E_{kin}^{0.75-1.10}$ over a variety of elements and compounds, but with the majority of elements in Fig. 2 suggesting

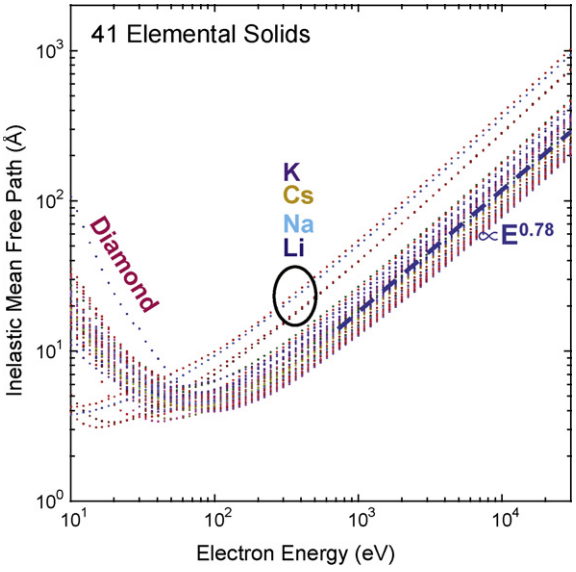

Fig. 2. Inelastic mean free paths (IMFPs) for 41 elements, calculated using the TPP-2M formula: Li, Be, three forms of carbon (graphite, diamond, glassy C), Na, Mg, Al, Si, K, Sc, Ti, V, Cr, Fe, Co, Ni, Cu, Ge, Y, Nb, Mo, Ru, Rh, Pd, Ag, In, Sn, Cs, Gd, Tb, Dy, Hf, Ta, W, Re, Os, Ir, Pt, Au, and Bi. Five "outlier" elements are indicated to provide some idea of what electronic structure characteristics can give rise to deviations from the majority behavior: diamond and the alkali metals. The dashed straight line for higher energies represents a variation as $\Lambda_e \propto E_{kin}^{0.78}$, and is a reasonable first approximation to the variation for all of the elements shown (from Ref. [23]).

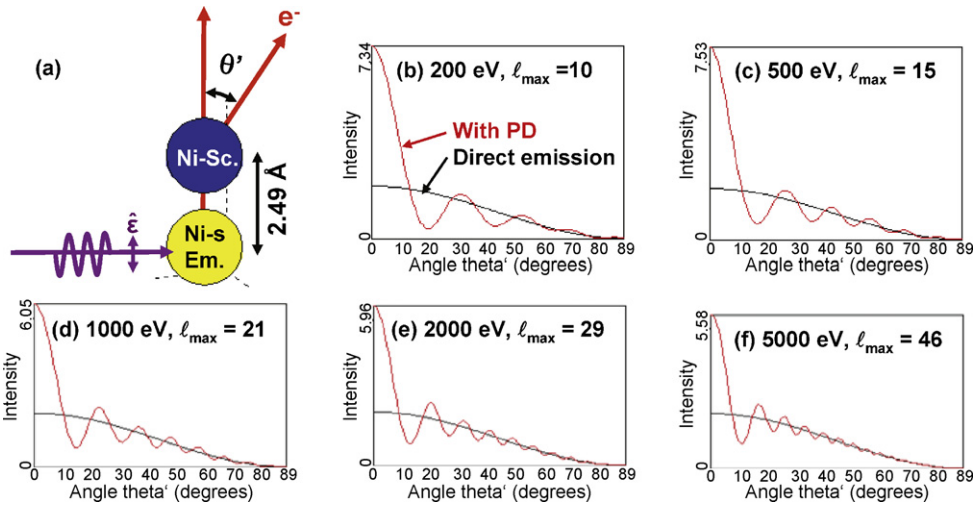

Fig. 3. Single scattering calculations of Ni dimer photoelectron diffractions patterns for s-level emission into a p outgoing wave at various photon energies. (a) The model geometry, with polarization along the Ni–Ni bond direction, and only one Ni atom considered as emitter. (b)–(f) Diffraction patterns for energies from 200 to 5000 eV are shown in red, with the direct emission in the absence of scattering also shown in black. In each panel, the number of partial wave phase shifts needed to assure full convergence is indicated, with this leading to one limitation of using the cluster approach at energies beyond about 5000 eV (calculations using the EDAC program of Ref. [44]). (For interpretation of the references to color in this figure caption, the reader is referred to the web version of the article.)

$E_{kin}^{0.78}$ as a convenient estimation formula. It is also noteworthy that the only element here which shows an unusually large increase in its IMFP at energies down to 10 eV is diamond, with a very large bandgap of 5.5 eV. Four other outliers over the full energy range are the alkali metals. These results thus strongly suggest that the only way to significantly enhance the bulk sensitivity of photoemission beyond what is achieved routinely in XPS at ca. 1 keV is to go into the multi-keV regime, with the only type of material expected to show a strong increase in IMFP at very low energies being an insulator with fairly large bandgap. This provides a major impetus for the new developments in hard X-ray photoemission, as discussed by Köver later in this article.

Inelastic scattering at the surface is also an important consideration in XPS, as discussed elsewhere in this issue by Nagatomi and Goto. This is expected to decrease in importance as the kinetic energy increases, as discussed also in the later article by Köver.

Note also that the form of the inelastic tail and background in an XPS spectrum can provide an immediate qualitative, and with further analysis even quantitative, idea of the depth distribution of the emitting species. Qualitatively, a peak with a very high intensity in its inelastic tail must have its origin in an atom well below the surface, whereas a peak with a very low inelastic tail must have its origin in an atom near to or on the surface. Analyzing such effects quantitatively was pioneered by Tougaard [29(b)], who discusses it elsewhere in this issue.

Finally, it is also worthwhile in this section to discuss some significant advantages that accrue to using hard X-rays in the multi-keV regime for excitation in ARXPS, a topic that is also explored in depth here by Köver. To first illustrate the effects of elastic scattering on ARXPS, Fig. 3 shows a set of calculations at different photoelectron energies from 200 to 5000 eV obtained with the photoelectron diffraction program EDAC [44]. The atomic cluster (Fig. 3(a)) is a simple diatomic of two Ni atoms separated by the Ni nearest-neighbor distance. The polarization is oriented along the Ni–Ni bond, and electrons emitted from an s-level ($\ell = 0$) in one of the atoms are detected by moving the spectrometer relative to the bond direction. The black curves represent the unscattered intensity in the absence of the Ni scatterer; they clearly show the influence of the s-level differential cross-section, which goes as $\cos\theta'$, with θ' being the scattering angle. With scattering and interference of direct and scattered waves, the red photoelectron diffraction patterns result. They show the well-known forward scattering peaks along the bond direction, and higher-order interference fringes that we will later see can be related to a holographic interpretation of such data [45]. In the simplest single-scattering picture, the maxima of these holographic fringes should appear when the following equation is satisfied:

$$2\pi m = \left[\frac{2\pi}{\lambda_e}\right] d_{sc}(1 - \cos\theta') + \varphi_{sc}, \quad m = 1, 2, \ldots \tag{4}$$

where λ_e is the electron de Broglie wavelength, d_{sc} is the distance between emitter and a given scatterer, and φ_{sc} is the phase shift associated with the scattering process, often small compared to the first term in Eq. (4). It is important for the present discussion that these forward scattering peaks become much narrower, and the higher-order fringes decrease in magnitude, as energy increases. This is a result of the narrowing of the forward peak in the differential elastic scattering cross-section, and the decrease in importance of larger scattering angles. Thus, large-angle scattering effectively becomes negligible for angles greater than approximately by 15–20° at 5000 eV, and this trend is expected to continue for higher energies.

Another aspect of high-energy photoelectron escape from a solid that has recently been emphasized is that extrinsic loss processes such as plasmons do not lead to a significant change in the direction of electron motion [39]. Thus, the effects of both elastic and inelastic scattering on ARXPS are expected to diminish as energy increases, leaving the straight-line trajectory as a better approximation.

The implications of the above discussions for ARXPS are illustrated in Fig. 4. At typical XPS energies of 500–1500 eV (Fig. 4(a)), one must allow for elastic scattering in estimating the effective emission depth, as mentioned above. For very low angles, refraction of the electrons as they surmount the inner potential can act to further reduce the degree of surface sensitivity in measured spectra. Finally, surface inelastic scattering processes can further complicate analyses. As Fig. 4(b) indicates, all three of these effects tend to be markedly reduced as energies mount into the hard X-ray regime. Forward elastic scattering which does not change propagation direction significantly becomes dominant (cf. Fig. 3). The inner potential is much smaller than the photoelectron energy, such that refraction is negligible until very low angles of exit. Thus, obtaining more directly interpretable data down to takeoff angles of 5–10° should be possible in hard X-ray ARXPS; by contrast, at typical

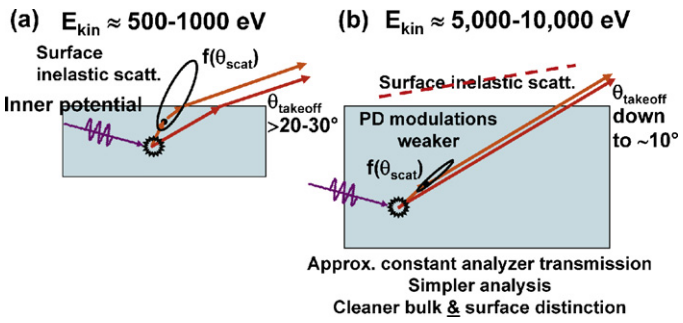

Fig. 4. Illustration of basic effects encountered in quantitatively interpreting angle-resolved XPS (ARXPS) data at (a) typical laboratory XPS energies and (b) hard X-ray energies into the 5–10 keV range. Several simplifications are possible with hard X-rays: less influence of high angle-to-low angle elastic scattering, reduced or negligible surface inelastic scattering, less effect of refraction in crossing the surface barrier, and a more constant spectrometer transmission function if the range of energies considered is not too large compared to the mean energy.

XPS energies, the usual recommendation is to limit this angle to no less than 20–30° [27,28]. Surface inelastic scattering is also much reduced. Thus, ARXPS or more precisely ARHXPS with hard X-rays, promises to be easier to analyze quantitatively, while having the advantage of allowing a broader angular range of data acquisition that will still allow significant surface enhancement at the lowest angles. We later show some recent experimental results of this kind.

4. Core-level spectra

From XPS energy distribution curves or spectra, a number of useful effects have been extracted, and, although these are well known to most XPS users, I discuss them here briefly for completeness and to establish vocabulary for subsequent sections:

- *Core-level chemical shifts* certainly represent one of the most often-used aspects of XPS. From the first clear confirmation of core-level chemical shifts, for the case of sodium thiosulfate-$Na_2S_2O_3$ [46], a very convenient compound that has S in two distinct chemical states that are resolved in the spectrum (actually serendipitously chosen for this experiment [47]), such chemical shifts have by now been measured for thousands of systems, providing unique information on the distributions of chemical and structural sites near surfaces. Such shifts can now be measured with resolutions in the 50 meV range using synchrotron radiation, yielding extremely sensitive decompositions of spectra into the chemical and structural components of a sample. The detailed theoretical prediction and interpretation of such shifts must always allow for the variety of final-state effects implicit in the discussion of Eq. (2) above. In other articles in this issue, the measurement and theoretical interpretation of such shifts for a variety of systems are discussed: the calculation of such shifts from local-density theory by Takahata and Dos Santos Marques, and by Olovsson et al.; the use of such shifts and the peak broadenings they produce to investigate metal alloys by Cole and Weightman; the combination of core-level photoelectron and Auger electron shifts into the Auger parameter by Moretti; and the use of chemical shifts in the study of nanostructures by Baer, self-assembled monolayers by Zharnikov, polymers and composites, adhesion by Watts, and semiconductor multilayer structures by Brundle.
- *Core-level multiplet splittings*: Another core-level effect is multiplet splittings in core-level emission from systems with unfilled valence shells [48,49]. The core subshell from which emission occurs can couple its spin and orbital angular momenta in different ways to the net spin and orbital angular momenta of the unfilled valence shells, resulting in more than one final state K in the language of Eq. (2) and thus more than one binding energy. The first measurements of this type were by Siegbahn et al. for the O_2, NO, and N_2 molecules [48], with the O 1s and N 1s binding energies for the paramagnetic molecules O_2 and N_2 being split into two components due to the spin-dependent exchange interaction of the 1s electron remaining after photoemission with the net valence electron spin. Soon afterwards, such splittings were measured for the transition metal atom Mn in several compounds [49], with the Mn 3s spectra in particular exhibiting doublets whose splittings are roughly proportional to the net 3d spin on Mn. These splittings and other final-state effects are now routinely used to probe the nature of the valence states and chemical bonding in magnetic and other complex materials, and they can be quantitatively analyzed using Anderson impurity model theory, with convenient computer programs for analyzing such data now available [50]. Some of these effects are illustrated in a case study below.
- *Core-level satellites and final-state configuration interaction*: Beyond the well-known shake-up and shake-off intensity first explored in noble gases and observed frequently in molecular systems, the first dramatic truly many-electron effect seen in XPS was final-state configuration mixing involving ligand-to-metal charge transfer [51]. By now, such measurements constitute a key tool in the study of transition metal, rare earth, and actinide compounds, with special importance for magnetic and strongly correlated systems. The interpretation of such data, which naturally include multiplet effects, is reviewed elsewhere, along with many experimental examples [50]. There is no doubt that the measurement and interpretation of such effects will be a major aspect of XPS in the future, including what one hopes will be even more accurate theoretical modelling involving also metallic systems. Closely related to these satellites are the so-called intrinsic loss processes that can create both electron–hole pair and plasmon excitations, and which can exhibit quantum mechanical interference with the normal extrinsic loss processes during electron transport. Theory and experiment concerning these effects are discussed elsewhere in this issue by Fujikawa and Köver.
- *Core-level vibrational fine structure*: It has long been realized that vibrational broadening can play a role in XPS spectra [52], but by now such effects have been resolved in adsorbates [53] and in many gas-phase molecular systems [54]. It is thus clear that such effects, and their temperature dependence, will play a role in the future quantitative analysis of XPS spectra.
- *Photoelectron diffraction and holography*: If the photoelectron emission direction is varied relative to the crystal axes of a single-crystal, epitaxial, or textured sample, for example by rotating the sample about the θ and ϕ axes in Fig. 1, additional effects are seen, due to the anisotropic elastic scattering and interference of the outgoing electron wave components from various atoms in the sample. If the emission is from a core level that is necessarily highly localized on one atomic site, a photoelectron diffraction pattern is observed [45]. The first X-ray photoelectron diffraction (XPD) patterns were measured for a NaCl crystal [55] and for a Au single crystal [56]. A more recent example of this for O 1s emission from NiO(0 0 1) is shown in Fig. 1(b). Such scanned-angle patterns can be used to determine near-surface atomic structures, and XPD has become one of the standard methods for determining surface structures [45], as we will consider in more detail below. Woodruff in this issue discusses the complementary synchrotron radiation based method of using scanned-energy photoelectron diffraction to determine adsorbate structures on surfaces. Photoelectron holography, in which a set of scanned-angle or scanned-energy photoelectron diffraction patterns are treated as a volume hologram in three-dimensional $\vec{K}$ space, has also been demonstrated in a number of experimental studies and

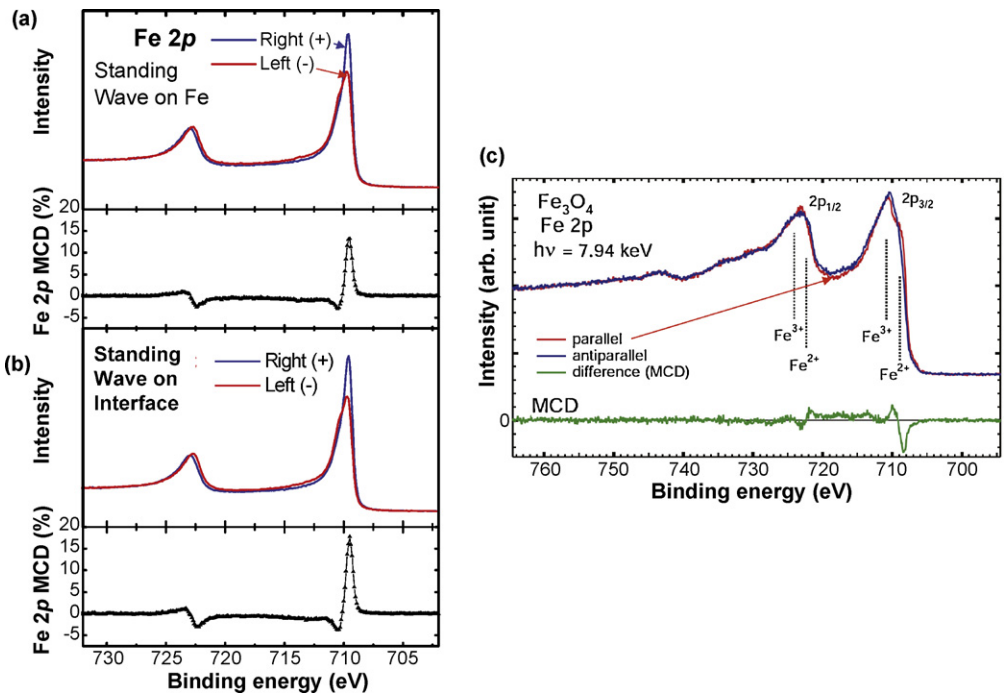

Fig. 5. Magnetic circular dichroism in Fe 2p emission. (a) and (b) MCD data for Fe emission from a 16 Å overlayer of Fe on a Cr wedge, excited by a soft X-ray standing wave at 825 eV that has been positioned either (a) maximally on Fe or (b) maximally on Cr near the Fe/Cr interface (from Ref. [33]). (c) MCD for Fe emission from hematite at 7.94 keV, demonstrating for the first time that these effects can be measured with hard X-rays (from Ref. [61]).

is reviewed elsewhere [57]. Matsushita et al. in this issue also discuss a newly developed method for holographic reconstruction. I will return later to consider both photoelectron diffraction and photoelectron holography (PD and PH) for a couple of illustrative examples, including the implications of taking the photoelectron kinetic energy into the multi-keV regime, with a preliminary theoretical look at what is expected in this already in Fig. 3.

- *Circular and linear dichroism*: Dichroism, in which a photoelectron intensity changes if the polarization of the incident radiation is changed, is ubiquitous in XPS due to the differential cross-sections that control the emission intensity. But beyond this are two significant effects that deserve attention here. First is something that is often referred to as circular dichroism in angular distributions (CDAD) [58]. This represents a combination of the preferential excitation of certain states of angular momentum (certain combinations of total angular momentum ℓ and z-component m_ℓ) by circularly polarized (CP) radiation, combined with forward-peaked elastic photoelectron scattering from nearby atoms. It results in what are often referred to as "peak rotations" in the PD patterns in the plane of the rotating electric field vector [58b]. It has also been pointed out that the two XPD patterns resulting from right and left CP (RCP and LCP) radiation can be considered in first approximation as a stereoscopic view of the atoms surrounding a given emitter [59], and Matsui et al. discuss this method later in this issue.

  If a given core level furthermore exhibits resolvable spin–orbit splitting, and the system also has long-range magnetic order relative to the radiation source and spectrometer coordinate system, magnetic circular dichroism (MCD) results. Here, the intensity of a photoelectron peak is found to change when the polarization of the incoming radiation is changed from right circular (RCP) to left circular (LCP). MCD is thus defined as the difference of two intensities or I(RCP) − I(LCP), usually divided by the sum or the average of these two intensities to yield a fractional number. These effects were first observed and qualitatively interpreted in core-level photoemission from Fe by Baumgarten et al. [60]. As more recent examples, Fig. 5(a) and (b) shows results obtained for Fe 2p emission from an Fe overlayer on a substrate of Cr, excited by a soft X-ray standing wave (SW) at 825 eV whose maximum has been located at two positions relative to the Fe/Cr interface [33]. Fig. 5(c) shows very recent results for Fe 2p emission from Fe_3O_4 at the much higher photon energy of 7.94 keV, a first demonstration that such effects persist in hard X-ray photoemission [61]. A simple one-electron explanation of these results [62] proceeds by noting that the spin–orbit interaction splits the six 2p states into two $2p_{1/2}$ and four $2p_{3/2}$ states. Beyond this, one assumes a Zeeman-like splitting of the sublevels within each spin–orbit peak induced by an effective internal magnetic field of the ferromagnet and resulting from the exchange interaction. These energy splittings are then combined with the different intensities expected for these $2p_{1/2}$ and $2p_{3/2}$ levels through the appropriate atomic transition probabilities. The expectation from this simple model is an up-down character for the MCD profile across a given peak, as well as an opposite sign of the MCD for the $2p_{3/2}$ and $2p_{1/2}$ peaks, as seen in Fig. 5. This general form of 2p MCD spectra has by now been observed in many 3d transition metal systems, and it clearly also exists up to much higher excitation energies [61]. Combining SW excitation with MCD will be discussed in more detail below. Because ferromagnetic order is necessary for MCD to be observed, measurements of this type provide an element-specific measurement of magnetic order, and this technique has been used to study a variety of magnetic systems.
- *Resonant photoemission*: A final important effect related to photoelectron intensities is resonant photoemission (RPE), in which the photon energy is tuned so as to lie on a strong core-level absorption resonance (e.g. Mn $2p_{3/2}$ or L_3), with this providing a second interfering channel for photoelectron excitation in another level in the same atom (e.g. Mn 3d) [63]. The intensity of the second level can thus be dramatically increased or decreased, depending on the relative amplitudes and phases of the interfering channels. This effect can be very useful in enhancing the contributions of a given type of valence character to bonding (e.g. by enhancing

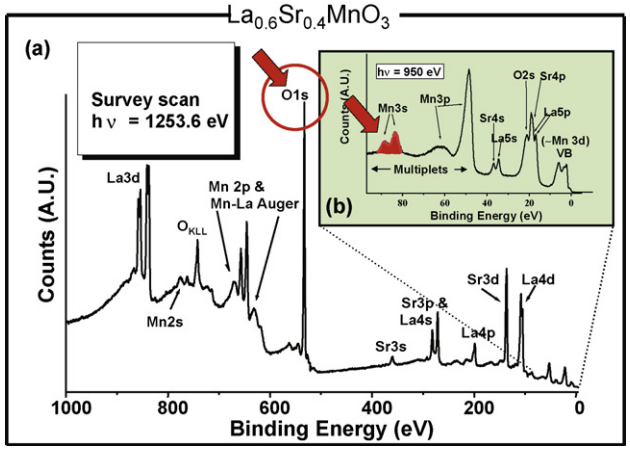

Fig. 6. (a) A broad survey spectrum from the colossal magnetoresistive oxide $La_{0.6}Sr_{0.4}MnO_3$ obtained with excitation at 1253.6 eV, together with (b) an inset obtained at 950 eV over the region of the highest lying core levels and the valence levels. The highlighted O 1s and Mn 3s spectra have been studied as a function of temperature, as shown in the next figure (from Ref. [84]).

the Mn 3d contributions to the valence spectra of a compound such as the colossal magnetoresistive oxide shown in Fig. 6 [63]). Extending this kind of resonant photoemission study into the hard X-ray regime has also been discussed recently [64]. It has also been pointed out that resonant photoemission can occur between levels on different atoms, as e.g. between O 1s and Mn 3d in the compound MnO [42], with this type of multi-atom resonant photoemission (MARPE) effect providing the potential of uniquely identifying near-neighbors to a given atomic species. In the later article of Fujikawa, the theory of MARPE is discussed in detail. As a final interesting new aspect of RPE, it has been pointed out that XPD carried out at a resonant energy can be used to enhance the emission from certain types of atoms in a system [65]; thus resonant X-ray photoelectron diffraction (rXPD) has recently emerged as a potentially useful new technique for the future, and we discuss one example of its application below.

5. Valence-level spectra-angle-resolved photoemission (ARPES) and the XPS limit

If the emission is from a valence level that is delocalized over many sites due to chemical bonding and molecular orbital or electronic band formation, additional anisotropy in emission is found, and this can be measured, for example, by taking advantage of another property of the hemispherical electrostatic analyzer with a two-dimensional (2D) imaging detector, as shown in Fig. 1(c) for emission from *W*(1 1 0) [66]. In this case, a 2D image in the detector plane can be directly related to the binding energy vs electron momentum or electron wave vector inside the crystal $\vec{k}$, which is then in many cases directly relatable to the band structure, or more precisely the quasi-particle excitation spectrum of the material. Such angle-resolved photoemission (ARPES) measurements are numerous in the literature, they have typically been carried out at energies below ~150 eV, and thus they are not strictly speaking XPS. We consider below some recent promising developments involving energies in approximately the 1–6 keV range.

For most materials at room temperature, the combined effects of phonons and angular averaging in the spectrometer yield X-ray excited ARPES spectra that are directly related to the total density of valence electronic states; this situation has often been referred to as the XPS limit. The existence of this limiting behavior was realized in very early experiments on a family of transition metals [67,68], and there are by now many examples of its application. The effects of phonons in reaching this limit have also been discussed previously [69]. The use of XPS to study densities of states is thus another very productive aspect of the technique, and the article by Knippenberg and Deleuze in this issue discusses this for conjugated aromatic systems.

6. Additional variations on the XPS experiment

6.1. Spin-resolved XPS

If an additional sensitivity to electron spin is somehow built into the detector, e.g. by taking advantage of spin–orbit scattering of high-energy electrons from a heavy-atom target in Mott scattering [70], or low-energy electrons from a heavy atom [71], or a magnetic atom [72], it is possible to measure also the electron spin, providing additional information of particular relevance to magnetic materials. Such measurements were pioneered by Siegmann and co-workers [73]. As an example of such data, Fig. 1(d) shows a more recent measurement of this kind for the valence bands of iron, clearly indicating the difference in the electronic state distributions of spin-up and spin-down electrons for this ferromagnet [74]. The extent of development of this aspect has been limited by the ~10^3 to 10^4 times greater data acquisition times required, but such measurements can provide unique information concerning magnetic systems, and with brighter radiation sources and faster detectors involving low-energy scattering mentioned above, spin-resolved XPS should see expanded usage in the future.

6.2. XPS with hard X-ray excitation

Fig. 1(f) further indicates the option of varying photon energy significantly above and significantly below the energy regime from ~20 to 1500 eV that has been used in most prior photoemission measurements, with the aims of increasing the degree of bulk sensitivity and/or improving energy resolution. As noted in connection with the discussion of Fig. 2, hard X-ray photoemission (HXPS or HAXPES) represents a very promising and rapidly growing new direction which is overviewed in several recent sources [75–77], and discussed in detail by Köver in this issue. I also return to consider a few additional aspect of HXPS later in this article.

6.3. Time-resolved photoemission

There are also newer types of measurements (again Fig. 1(g)) in which some perturbation of the sample is made, e.g. by gas reaction with a clean surface, by short-pulse light excitation, or by short-pulse field exposure and the spectra are measured as a function of time. Depending on the particular process involved, these measurements can be fruitfully carried out on timescales varying from minutes (for surface chemical reactions at higher ambient pressures) down to femtoseconds (for laser or synchrotron radiation pump-and-probe experiments) [78–80]. Some time-resolved studies in conjunction with photoelectron microscopy are considered by Oelsner in a later article in this issue. Looking ahead in the time domain, it seems clear that one exciting application of time-resolved XPS will be to use PD and PH to do time-resolved atomic imaging of small-to-medium sized molecules or of the local environment of atoms around an emitter near a surface. It has been obvious from the beginning of solid-state PD that it represents a way to look at local atomic structure in an element-specific way "from the inside out", and this has more recently also been recognized by the molecular physics community [81]. In this case, the exciting source would be a very short X-ray pulse from a free-electron laser or next generation X-ray source, and this could be moved in time delay relative to some other pulse which initiates an electronic or atomic structural change. Such "molecular movies"

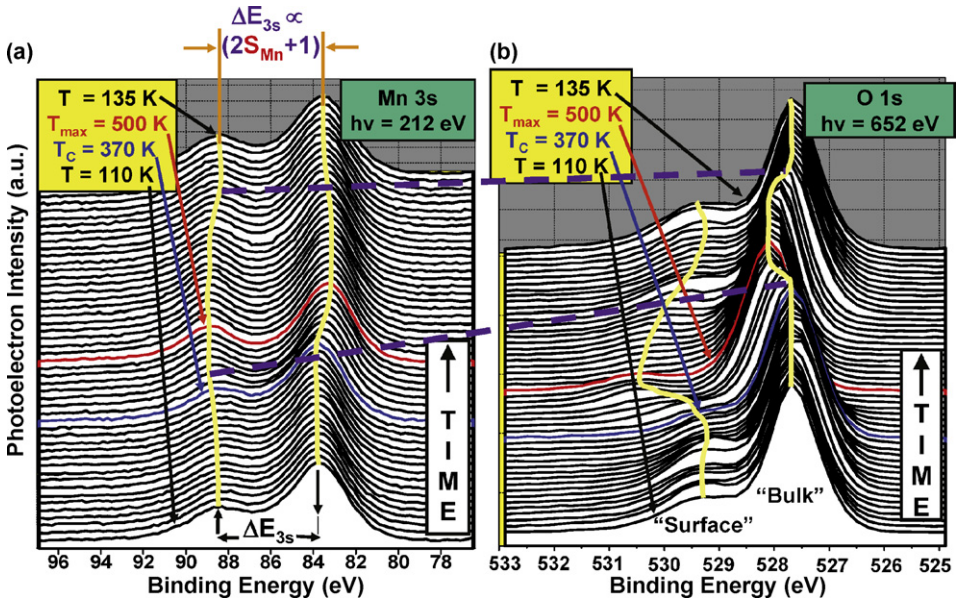

Fig. 7. Temperature dependence of the Mn 3s and O 1s spectra from a freshly fractured surface of $La_{0.7}Sr_{0.3}MnO_3$ (cf. Fig. 6). The two photon energies indicated have been chosen so that the photoelectrons in both cases have very nearly the same kinetic energy and thus the same inelastic attenuation lengths and surface sensitivity (from Ref. [84]).

would enable for the first time directly viewing atomic and electronic dynamics on their inherent timescales. It is not yet clear how easy it will be to use such ultrabright sources on solid samples and surfaces, but with future developments in large-scale multiplexing analyzer/detector combinations, e.g. by using time-of-flight methods, it is definitely in the realm of possibility. Gas-phase experiments from which small-molecule atomic movies will result seem certain to succeed to some degree in the not-too-distant future, as discussed further below.

6.4. XPS at multi-torr pressures

Finally, Fig. 1(h) indicates that it is possible with special differential pumping outside the sample region to carry out studies at up to several torr of pressure [82,83], and this is another rapidly growing area of activity, as discussed in more detail later in this article.

There is thus an extremely rich and steadily growing array of effects and methods in X-ray photoelectron spectroscopy and I will now turn to a few recent examples, drawn both from the work of my group and its collaborators and from other groups as appropriate, to illustrate some promising applications and future directions.

7. Applying multiple electron spectroscopies to a complex strongly correlated oxide—$La_{1-x}Sr_xMnO_3$

As a recent example of the use of a variety of effects in XPS spectra, including spectra obtained with hard X-ray excitation, I consider some recent studies of the colossal magnetoresistive oxide $La_{1-x}Sr_xMnO_3$ with $x = 0.3$ and 0.4 [84–86]. This is a strongly

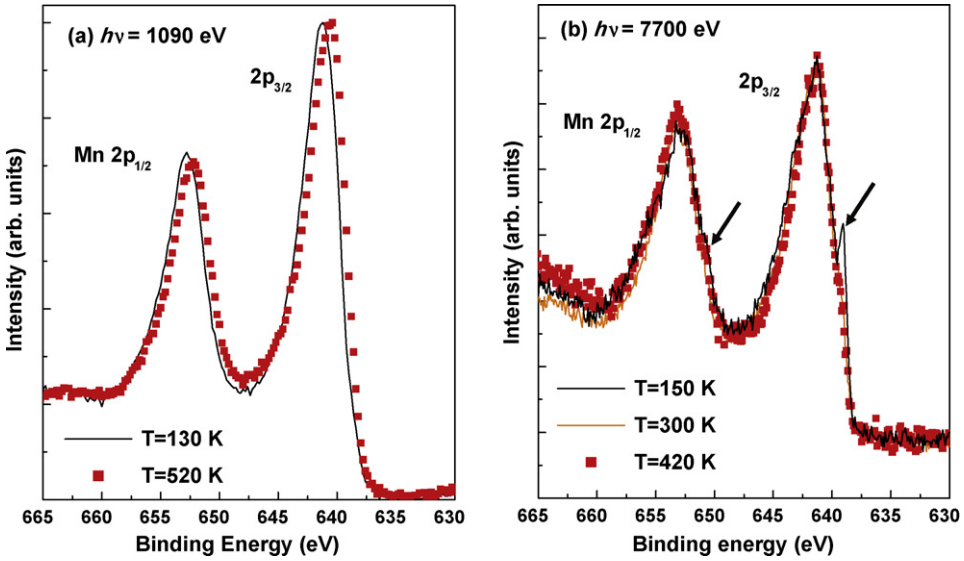

Fig. 8. Mn 2p photoelectron spectra from fractured $La_{0.7}Sr_{0.3}MnO_3$ surfaces at two different photon energies of (a) 1090 eV and (b) 7700 eV, and for temperatures below and above the Curie temperature of 370 K. The arrows in (b) highlight two low-binding-energy satellite features, a very sharp one on $2p_{3/2}$ and a small shoulder on the $2p_{1/2}$ peak, that are thought to arise from bulk-like long-range screening processes (from Ref. [86]).

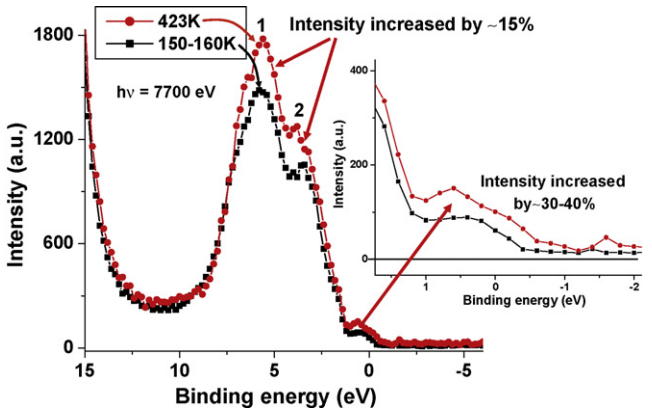

Fig. 9. Valence photoelectron spectra excited at a photon energy of 7700 eV from a fractured $La_{0.7}Sr_{0.3}MnO_3$ surface at two different temperatures above and below T_C. The only normalization done between the two spectra is to force the close-lying Sr 4p and La 5p intensities to be equal. The inset shows an expansion for the region near the Fermi level (from Ref. [86]).

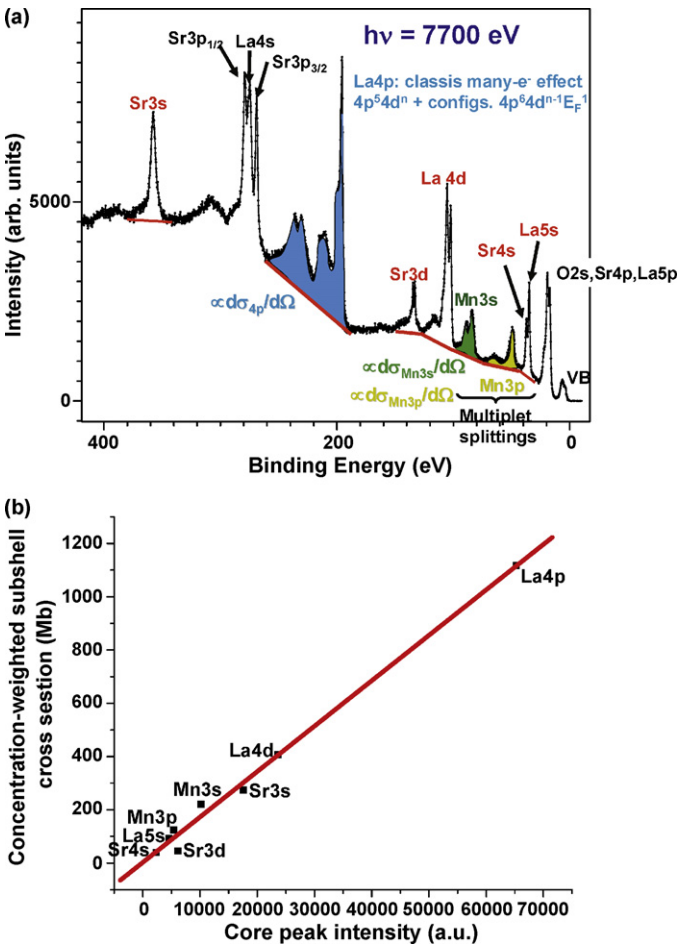

Fig. 10. (a) High-lying core and valence-level survey spectrum from a fractured $La_{0.7}Sr_{0.3}MnO_3$ sample, with the origins of all features labelled, including multiplet splittings of Mn 3s and 3p, as well as many-body final-state mixing for La 4p. Peak areas were measured for eight of the labelled peaks. (b) Peak areas from (a) are compared to a product of stoichiometric concentration and differential photoelectric cross-section, thus assuming a constant analyzer transmission function and that the IMFPs for all peaks are identical (from Ref. [90]).

correlated material that is also thought to be a half-metallic ferromagnet and is of interest for spintronic applications. The chemical and magnetic state of the Mn atoms is thus a key factor influencing the behavior of this material. In Fig. 6 are (a) broad and (b) zoomed survey spectra indicating all the relevant photoelectron and Auger peaks observed with excitation of $La_{0.7}Sr_{0.3}MnO_3$ in the typical XPS regime of ~1 keV [84]. The valence-band (VB) region in Fig. 6(b) is expected to be dominated by Mn 3d character, as the 3d cross-section at 950 eV is about 5× larger than that of O 2p that is admixed with it. The oxide surface was here prepared by cleaving, or more precisely, fracturing, a single crystal in UHV, in order to minimize surface contamination. In Fig. 7(b), we show the temperature dependence of the O 1s spectra from the same sample. Firstly, these O1s spectra exhibit a main peak and a weaker peak at about 1.5 eV higher binding energy. From various measurements, including varying the electron takeoff angle to change the degree of surface sensitivity (see earlier discussion), it is concluded that the peak at higher binding energy is due to O atoms near/at the surface, with the other peak representing O atoms deeper within the material and denoted "Bulk" in the figure. Now considering the changes in these spectra as temperature is varied from well below to well above the temperature at which long-range ferromagnetic order disappears (the Curie temperature, T_C, which is 370 K for this material) and then cooled to near the starting temperature again, a distinct shift in the bulk O 1s binding energy to higher values is observed as T goes up to about 150 K above T_C, together with a concomitant shift, broadening and loss of intensity in the O 1s surface peak. Upon cooling again to below T_C, both features return to their previous states. The bulk peak shift has been interpreted as a transfer of electron charge to Mn from the six O atoms arranged in an octahedron around each Mn atom, via classic qualitative reasoning for chemical shifts and charge transfer [84].

Fig. 7(a) further shows the temperature dependence of the Mn 3s splitting in $La_{0.7}Sr_{0.3}MnO_3$, and it exhibits a marked increase of about 1 eV or 20% over the same temperature range as the O 1s chemical shifts discussed previously. This increase has been interpreted as being caused by an increase in the Mn spin that is equivalent to a net transfer of one electronic charge from the O atoms to Mn, an effect not observed previously [84].

As an example of what can been seen in addition for this system with hard X-ray photoemission, we compare in Fig. 8 temperature-dependent Mn 2p spectra from the same type of colossal magnetoresistive oxide sample involved in Figs. 6 and 7, excited by (a) soft X-rays and (b) hard X-rays [86]. The data in Fig. 8(a) obtained at an excitation energy of 1090 eV, corresponding to kinetic energies of ~450 eV and an inelastic mean free path of ~10 Å [23], are compared with data in Fig. 8(b) obtained at 7700 eV, corresponding to kinetic energies of ~7050 eV and an inelastic mean free path of ~85 Å [23]. Thus, the latter represents a much truer sampling of bulk properties. Although the general shape of the doublet is the same at the two energies, there are two significant differences. First and most obvious in the hard X-ray spectrum is a small, but very sharp, satellite that appears below T_C on the low-binding-energy side of the $2p_{3/2}$ peak, but which is only hinted at in the lower-energy more-surface-sensitive spectrum. There is also an indication of the same satellite, although less well resolved, on the $2p_{1/2}$ peak, as indicated by the arrow. This type of satellite has been observed in HXPS from other manganite and strongly correlated oxide samples, and it has been interpreted as a screening satellite associated with highly delocalized electrons [87–89], with the implication that it requires the extended volume of a more bulk-sensitive measurement to see it. This satellite is also observed to slowly disappear as temperature is raised, which implies a connection with either magnetic order or a lattice that is free of the kind of lattice distortion above T_C that is thought to produce the effects seen in Fig. 7 [84]. A second difference between the hard X-ray and soft X-ray spectra is that a chemical shift with soft X-ray excitation of both Mn 2p components to higher binding energy by about 0.7 eV on lowering the temperature to about 150 K, and

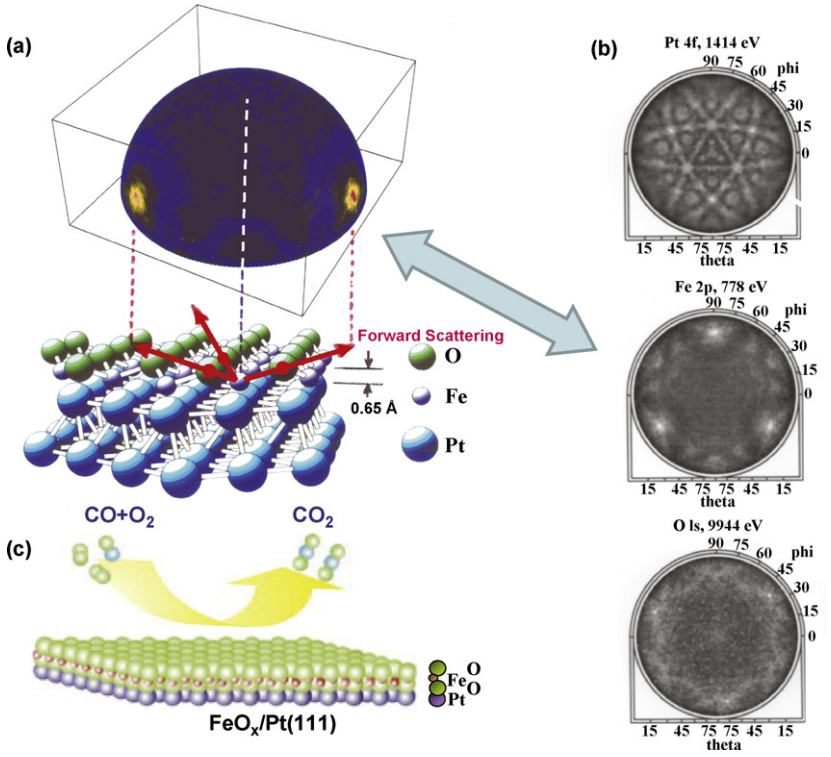

Fig. 11. X-ray photoelectron diffraction at 1486.7 eV excitation from a monolayer of FeO grown on Pt(1 1 1). (a) A full-hemisphere pattern for Fe 2p emission is shown, above the atomic geometry finally determined for this overlayer. (b) Two-dimensional projections of diffraction patterns simultaneously accumulated for emission from Pt 4f (kinetic energy 1414 eV), Fe 2p (778 eV), and O 1s (944 eV) (from Ref. [91]). (c) The O–Fe–O bilayer geometry to which this FeO overlayer is hypothesized to convert when it catalyzes the oxidation of CO (from Ref. [92]).

which has been linked to the O-to-Mn charge transfer discussed in connection with Fig. 7 [84,85], is difficult to discern with hard X-ray excitation. Beyond this, the changes in the Mn 3s multiplet splitting with temperature are found to be less with hard X-ray excitation [86]. Taken together, these results suggest that the effects seen in Fig. 7 are more localized near the surface, within approximately the first 30–40 Å. Combining soft and hard X-ray photoemission has thus been very useful in determining the effective depths of these effects.

Fig. 9 now shows the temperature dependence of the valence spectra from $La_{0.7}Sr_{0.3}MnO_3$ with hard X-ray excitation [86], and

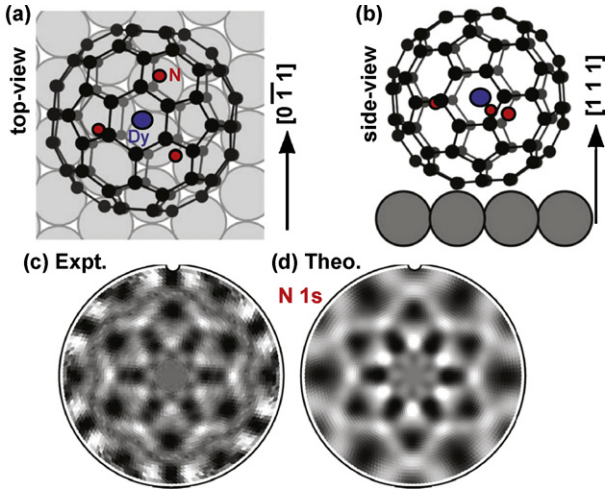

Fig. 12. (a) and (b) Two views of the adsorption geometry of the endofullerene DyN_3 in C_{80}, as determined from a combination of STM, XPD, and resonant XPD. (c) and (d) Experimental and theoretical diffraction patterns for emission from the three N emitters in the system, respectively (from Ref. [93]).

illustrates another useful aspect of such HXPS measurements: deriving information on valence population changes with temperature or composition. These spectra have been normalized to the combined Sr 4p, and La 5p core-level intensities nearby (see Fig. 6(b)), which are not expected to change with temperature. With this normalization, it is clear that the valence spectra change in relative intensity, exhibiting increased intensity at the higher temperature. Considerations of the relative magnitudes of the relevant valence atomic cross-sections at this energy for Mn 3d, Mn 4s, and O 2p, as well as the expected relative populations of these orbitals in the valence bands as estimated from local-density theory, leads to the conclusion that the increases in the valence-band intensity in this figure further confirm an increase in the Mn 3d population at high temperature, as first concluded based on the data in Fig. 7.

As a final aspect of the hard X-ray data for this manganite, Fig. 10(a) shows a survey spectrum including the valence levels and a number of core levels, with all peaks labelled [90]. The core peaks illustrate two different types of final-state effects: the Mn 3s and Mn 3p spectra exhibit multiplet splittings, and the La 4p region is distributed in a complex way over about 30 eV due to the mixing of final states with configurations $4p^5 4d^{10}$ and $4p^5 4d^9 E_F{}^1$, both well-known from previous studies [5,6]. The areas of various peaks connected with all of the atoms in the sample have been measured by subtracting the backgrounds shown, and being careful to include all final states associated with a given core hole. Thus all of the multiplet structure for Mn 3s and 3p, and all of the final-state mixing for La 4p have been included in estimating their respective intensities. In Fig. 10(b) is now shown a plot of these experimental intensities vs the concentration-weighted differential cross-section for each core level, assuming that, for this high-quality single crystal with a freshly fractured surface, the stoichiometry probed by photoemission is that of $La_{0.7}Sr_{0.3}MnO_3$. The resulting plot is linear, with most peaks falling within +/− 10% of a straight line, with no correction for the spectrometer transmission function. This illustrates other

advantages of HXPS: (1) to a good approximation, the spectrometer transmission will be constant over the valence and high-lying core region, as the retard ratio changes very little; in this case the electron kinetic energies in Fig. 10(a) vary only over electron kinetic energies of 7300–7700 eV, so for retardation to the energy of analysis of 200 eV used here, the retard ratio changed only from 0.0273 to 0.0259. (2) The inelastic mean free path, and thus mean emission depth, which is expected to vary roughly as $E_{kin}^{0.75-1.10}$, can also be assumed constant over this spectral range also, changing by only about 5% over the spectrum. Thus, quantitative analysis of spectra to determine stoichiometries in complex materials will be more reliable with hard X-ray excitation, while keeping in mind that all final states reached must be included in peak area determinations.

The further application of this type of combined soft and hard X-ray photoemission to other strongly correlated materials or complex multicomponent materials is thus a very promising area for the future.

8. Photoelectron diffraction and photoelectron holography

8.1. Application to oxide overlayer growth and fullerene adsorption

As one example of how XPD can be used, in what was a study with complementary information from STM and LEED, we show in Fig. 11(a) the full-hemisphere intensity distribution for Fe 2p emission at 778 eV kinetic energy from a monolayer of FeO grown on a Pt(1 1 1) surface [91]. At this energy, the forward-peaked nature of the electron scattering is observed to create strong peaks in intensity along the Fe–O bond directions, as well as first-order interference around these peaks (cf. Fig. 3(d) for 1 keV). The angle at which the forward scattering peaks are seen can furthermore be used to estimate the distance between the Fe and O atoms in the overlayer, and it is found to be only about half that for similar bilayer planes in bulk FeO, as illustrated in the bottom of Fig. 11(a). Fig. 11(b) also illustrates the element-specific structural information available from XPD. The Pt 4f XPD pattern from the same sample is rich in structure due to the fact that emission arises from multiple depths into the crystal, with forward scattering producing peaks and other diffraction features along low-index directions. The bands of intensity in the Pt pattern can be ascribed to Kikuchi bands, as discussed further below. The Fe 2p pattern is here just a projection onto 2D of the 3D image in Fig. 11(a). The O 1s pattern shows only very weak structure, as the O atoms are on top of the overlayer, with no forward scatterers above them, and only weaker side and back scattering contributing to the diffraction pattern. Comparing the Fe and O patterns thus immediately permits concluding that Fe is below O in the overlayer, rather than vice versa. It is also interesting to note that this FeO monolayer has very recently been found to be catalytically very active, in particular for the low-temperature oxidation of CO [92], suggesting future applications of such monolayer oxide catalysts. For the bilayer FeO case, it is further hypothesized that a double-layer O–Fe–O sandwich forms at the surface as it actually becomes involved in catalysis, as illustrated in Fig. 11(c) [92]. Doing O 1s XPD on this double-layer would immediately show by forward scattering peaks for emission from the bottom O layer due to both Fe and O in the layers above that this hypothesis is correct, an obvious interesting future experiment.

As another recent example of XPD as applied to a much more complex structure, a fullerene-based system, Fig. 12(a) and (b) shows two views of the atomic geometry expected when a C_{80} fullerene enclosing a DyN_3 molecule is adsorbed in an ordered array on Cu(1 1 1) [93]. Fig. 12(c) and (d) shows the experimental N 1s XPD pattern (a) and compares it to a theoretical pattern (b) that permits, together with separate resonant XPD patterns of the Dy MNN Auger intensities, concluding that the N atoms occupy very nearly the center of the C_{80} cage, while the endohedral DyN_3 unit takes at least two symmetry-inequivalent, but closely related, orientations in the C_{80} cages on the substrate surface. Even though there are in addition three slightly symmetry-inequivalent N-atom emitters for each DyN_3 unit in this system, the complex XPD pattern could be analyzed to derive useful structural results. It is also worth noting that, in this and other cases involving XPD from adsorbates, the simplification of using only a single-scattering cluster (SSC) type of theoretical modelling is found to be adequate. For emission from atoms in a bulk crystal or significantly below a surface, multiple scattering along rows of atoms must be considered for quantitative XPD modelling [45].

Many other examples of photoelectron diffraction in the study of clean surfaces, adsorbates, and nanostructure growth appear elsewhere [45,94,95], including discussions of an alternative method of PD measurement in which the geometry is held fixed and the photon energy is scanned [45,96], the principle focus of the article by Woodruff in this issue.

8.2. Hard X-ray photoelectron diffraction

As another future direction in XPD, we consider what might be possible by exciting with energies of several keV, as treated in a recent theoretical study [97] and demonstrated in some first experimental data [98,99]. Fig. 3 and Eq. (4) have already provided an introduction to the general systematics expected, with highly forward-peaked elastic scattering dominating the patterns, and any higher-order diffraction features being weaker and more closely spaced in angle. Beyond this, however, the higher inelastic mean free paths lead to the sampling of many more atomic layers in emission from a multilayer substrate, with effects of Bragg scattering from different sets of planes becoming visible. In this limit, the diffraction of the photoelectrons is better treated as a multiple Bragg scattering (also referred to as dynamical scattering) process leading to Kikuchi bands of intensity, as was in fact qualitatively recognized in the first XPD study [55]. From a theoretical point of view, this implies going from an atomic cluster formulation of the problem to one involving multiple scattering from Bragg planes, in what can be considered a time-reversed low-energy electron diffraction (LEED) picture with the surface explicitly included [97]. In fact, above around 5 keV, it begins to be difficult to use the cluster picture that is common in XPD algorithms [44], due among other things to the large number of scattering phase shifts (cf. Fig. 3) and the large atomic clusters required. For example, calculation times in the cluster approach scale roughly as ${N_{cluster}}^2\ (l_{\max}+1)^3$, where $N_{cluster}$ is the number of atoms in the cluster. A family of Bragg-based dynamical theoretical calculations over the energy range of 0.5–20 keV for emission from diamond is shown in Fig. 13(b) [97], where that for 1 keV can be directly compared to experiment in Fig. 13(a) [100]. The agreement between experiment and theory at 1 keV is excellent, including many fine-structure features. The expectation on going to higher energies is for sharper and sharper Kikuchi-band like features, as seen in the other panels of this figure. Further consideration of such calculations indicates that hard X-ray photoelectron diffraction (HXPD) should provide a very sensitive method for the element-specific bulk-sensitive determination of the positions of atoms in a complex lattice (for example, substitutional vs interstitial sites), as well as of lattice relaxations [97].

As an example of experimental HXPD, as well as hard X-ray ARXPS data obtained to date, Fig. 14 shows results of exciting Si 1s photoelectrons from clean Si(0 0 1) and Si(0 0 1) with 4 nm of native oxide on top with synchrotron radiation at 7.94 keV (panel (b)) and with monochromated Cr $K\alpha_{1,2}$ X-rays at 5.4 keV (panels (c) and (d)) [99]. These data have been obtained with a specially adapted commercial hemispherical analyzer–lens com-

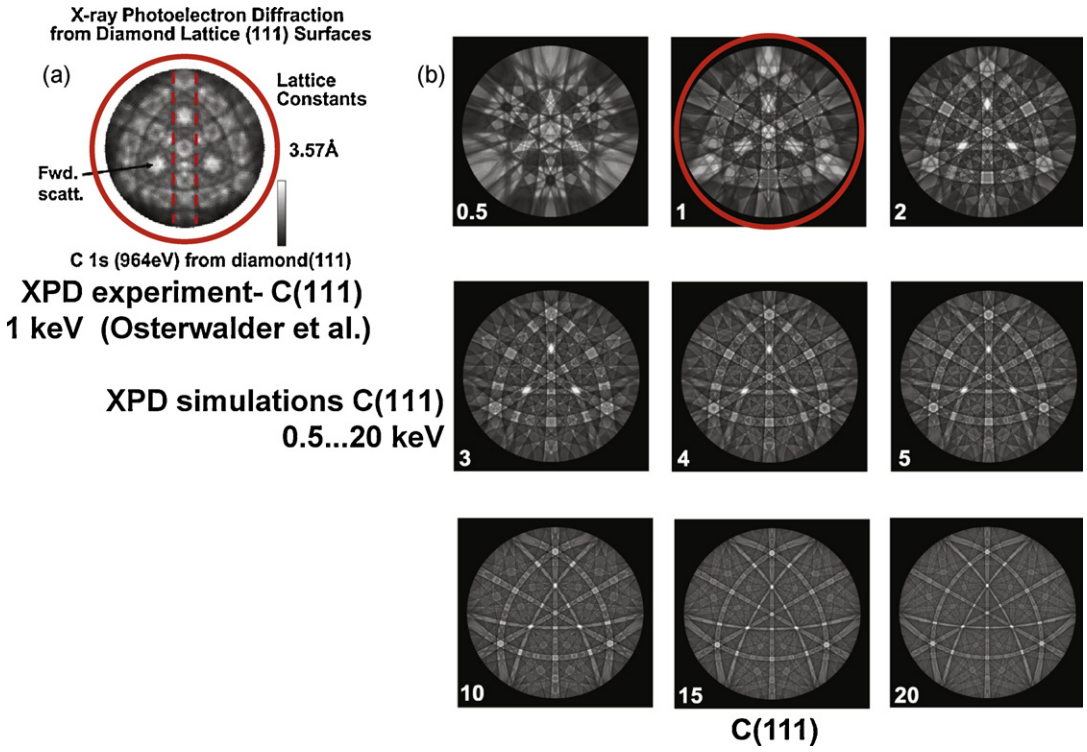

Fig. 13. (a) An experimental full photoelectron diffraction pattern from diamond (1 1 1) at 964 eV kinetic energy (from Ref. [100]). (b) Calculations using a Bragg reflection/Kikuchi band approach for photoelectron diffraction and going up to 20 keV in energy (from Ref. [97]).

bination that has been fitted with a wide-angle prelens and a bent-crystal X-ray monochromator in the Rowland circle geometry. Energy resolutions of ca. 0.26 eV at 7.94 keV and 0.50 eV at 5.4 keV and angular resolutions of 1° are achieved over approximately a large ±35° in detector θ (cf. Fig. 1). The Si^0 and combined $Si^{3+,4+}$ peaks in the presence of oxide are clearly resolvable in Fig. 14(a). In Fig. 14(b) a single detector image over the full angle range is shown for the oxidized sample. The relative enhancement of the oxide single relative to the normalized Si^0 signal is obvious, indicating that ARXPS can be performed quickly over a large-angle range with such an instrument, as also practiced with some commercial XPS spectrometers, but over a smaller angle range. Also, by rotating the sample in azimuth ϕ (cf. Fig. 1) and combining results, a large section of a hemispherical XPD pattern can be obtained. The Si^0 peak shows strong XPD effects in emission from the clean Si(0 0 1) surface in Fig. 14(c), with the clear presence of both forward scattering along low-index directions and Kikuchi bands (cf. Fig. 11(b) for Pt 4f and Fig. 13(a)). Fig. 14(d) illustrates the damping effect of the amorphous 4 nm layer of SiO_2, although there are residual Si XPD effects even with this relatively thick overlayer present. In other data, not shown here, the combined $Si^{3+,4+}$ peaks are found to show no XPD features, consistent with the expected amorphous character of the oxide.

HXPD and hard X-ray ARXPS experiments are thus just beginning, and this aspect of the technique awaits future development, but instruments such as that described above should make such data much more accessible, and the result should be a new tool for looking at local atomic structure in buried layers or in complex bulk materials. As one interesting type of experiment that awaits future trial, one can imagine tuning the hard X-ray incidence angle to an atomic-plane Bragg reflection, and then observing the HXPD patterns and the valence-band spectra as either the angle is varied over a rocking curve or the photon energy is scanned over the Bragg energy. This sort of "double-Bragg" experiment, in which both photons and electrons are Bragg scattering, but in general from different sets of planes, should permit even more precisely determining both local atomic structure and decomposing valence-band densities of state in an element-specific way.

8.3. Photoelectron holography

As noted earlier, a photoelectron diffraction pattern can also to a first approximation be considered a photoelectron hologram [101]. This has led to several studies in which diffraction patterns at various angles and/or various energies have been mathematically transformed so as to directly yield atomic positions in space. More precisely, if the photoelectron diffraction intensities $I(\vec{k})$ are measured over several angles and/or energies, equivalent to some volume in $\vec{k}$-space, and then normalized by subtracting out the smoother unscattered intensity profile I_0 corresponding to an unscattered reference wave to yield a function $\chi(\vec{k}) = [I(\vec{k}) - I_0(\vec{k})]/I_0(\vec{k})$, then the holographic image of the atoms neighboring the emitter $U(\vec{r})$ can be obtained from:

$$U(\vec{r}) = \left| \iiint \chi(\vec{k}) \exp[i\vec{k}\bullet\vec{r} - ikr] d^3k \right|, \quad (5)$$

where the exponential phase factor is that appropriate to the phase difference between the reference wave and an object wave scattered from point $\vec{r}$, and the integral is over the volume in $\vec{k}$-space covered by the data points.

As one example of this approach, I show in Fig. 15 a holographic image obtained using Cu 3p photoelectron intensities above a Cu(0 0 1) surface, with the emitter (e) as the central reference point [102]. These images were actually obtained using a differential approach in which two holograms at slightly different energies are subtracted from one another so as to suppress forward scattering effects, which are deleterious as far as holography is concerned. Using this approach, it is clear that one can image about 15 near-neighbor atoms below and to the sides of the emitter. Other future possibilities with photoelectron hologra-

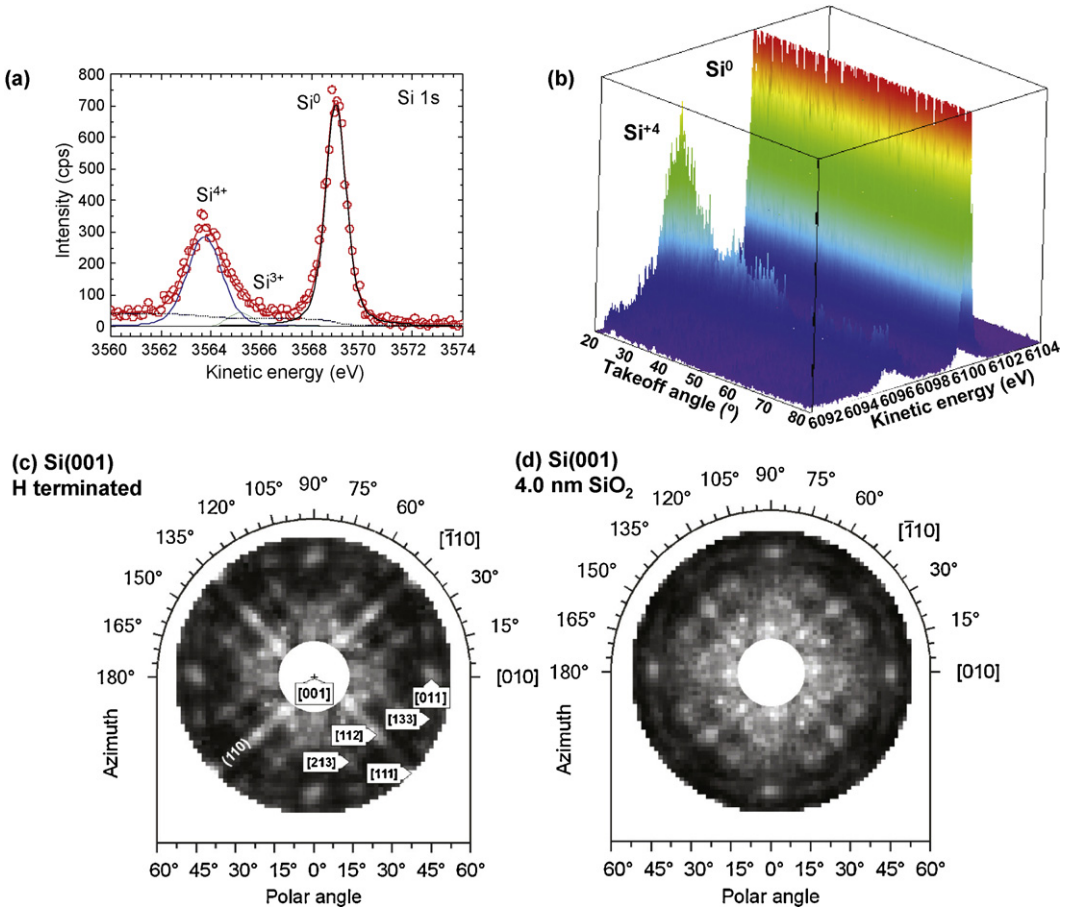

Fig. 14. Hard X-ray angle-resolved XPS (ARXPS-(b)) and X-ray photoelectron diffraction (HXPD-(c) and (d)). (a) A Si 1s spectrum from a Si sample with 4 nm of oxide on top, excited with monochromatized Cr Kα radiation at 5.4 keV, with different oxidation states labelled. (b) Multichannel Si 1s ARXPS data excited at 7.94 keV from a sample such as that in (a) and simultaneously obtained over a wide-angle range with a special prelens. (c) Large solid-angle hard X-ray XPD from Si^0 1s of Si(0 0 1) excited by Cr Kα and thus a kinetic energy of 3569 eV, with the data obtained from single detector images at various azimuthal orientations of the sample. (d) As (c), but with 4 nm of SiO_2 on top (from Ref. [99]).

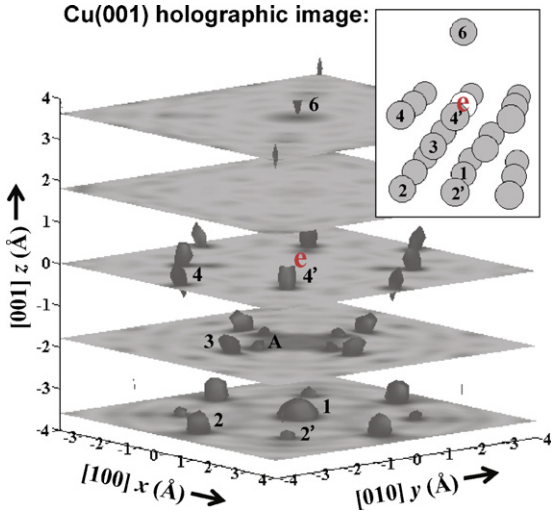

Fig. 15. Holographic image of the atoms neighboring a given reference Cu atom below a Cu(0 0 1) surface, based on a differential method in which holograms at two close-lying energies are subtracted from one another to reduce forward scattering effects. The typical reference emitter atom is noted by "e", and the neighboring atoms are indicated in the inset. The data yielding this image consisted of Cu 3p spectra at 25 kinetic energies from 77 to 330 eV and over 65 directions, thus representing about 1600 data points in k-space (from Ref. [102]).

phy, including making use of spin resolution and circular dichroism, are discussed elsewhere [57]. It should be noted, however that PH becomes more challenging at higher photoelectron energies due to the increasing importance of forward scattering and the weaker nature of the holographic fringes (cf. Fig. 3), although the differential approach mentioned above, and an alternative "near-node" approach in which the polarization vector is oriented such that the direct wave is near zero in the forward scattering direction [103], both can be used to compensate somewhat the deleterious effects on images of forward scattering [57].

It is also possible that PH could be used to directly image small molecules or local atomic clusters in a time-resolved mode, as discussed previously.

9. Photoemission with standing wave excitation and other X-ray optical effects

9.1. Basic methodology and the standing wave/wedge ("swedge") method

Carrying out measurements in an experimental geometry for which the reflectivity is high enough that the exciting radiation generates a significant standing wave represents a relatively newly developed method for selectively exciting at certain positions within the sample. As indicated in Fig. 16, the period of the square magnitude of the standing wave *E*-field will be given by $\lambda_{SW}(|E^2|) = \lambda_x/2\sin\theta_{inc}$, where λ_x is the X-ray wavelength. Going

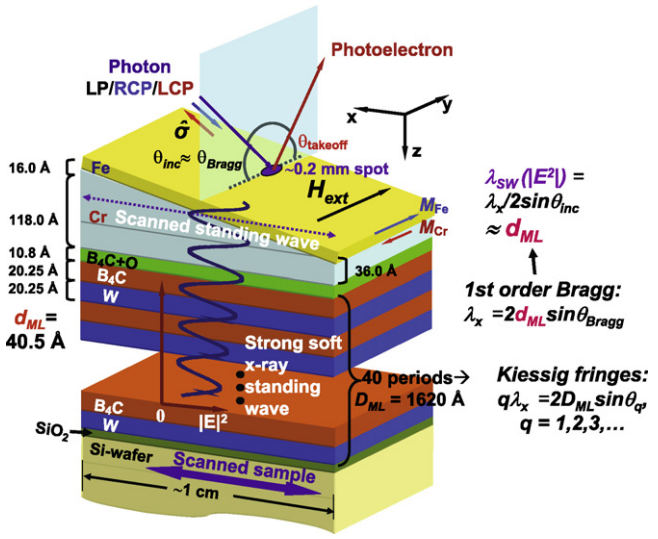

Fig. 16. Schematic illustration of the simultaneous use of an X-ray standing wave created by reflection from a multilayer mirror plus a wedge-profile overlayer sample to selectively study buried interfaces and layers—the "swedge" method. In the example here, a strong standing wave (SW) is created by first-order Bragg reflection from a multilayer made of repeated B_4C/W bilayers, and a Cr wedge underneath an Fe overlayer permits scanning the SW through the Fe/Cr interface by scanning the sample, and thus the X-ray spot, along the x direction. The two relevant equations for predicting the period of the standing wave along the z direction in conjunction with Bragg reflection from the multilayer are also shown. In addition, the equation for predicting Kiessig fringes in angular scans (rocking curves) is given. Other precise geometric parameters for the specific study in Ref [33] are also indicated (from Ref. [33]).

into a grazing-incidence total reflection geometry is one way to achieve high reflectivity [104]. Or, if the excitation is at a high enough energy (a short enough electron de Broglie wavelength λ_e) to permit Bragg reflection from crystal planes, then a standing wave parallel to a given set of Bragg planes $\{h\,k\,\ell\}$ can be generated; in this case, the SW period for first-order reflection is just the planar spacing $d_{h\,k\,\ell}$ [104–106]. In such a Bragg geometry, scanning the incidence angle over the Bragg angle, or scanning the photon energy over the Bragg energy, sweeps the SW vertically by about 1/2 to 3/4 of λ_{SW}, thus also moving it through the unit cell, and providing via core-level intensities information on atomic positions near a surface [31], or, by using both core and valence-level intensities, element-specific densities of states [32]. The latter is discussed by Zegenhagen in this issue. Another possibility is using reflection from a synthetic multilayer mirror to generate the SW, with this yielding in first-order reflection a SW period equal to the multilayer period d_{ML} (cf. Fig. 16) and permitting depth-resolved studies of nanometer-scale multilayer structures [33,104–106]. Finally, Fig. 16 indicates an additional type of fine structure that can be seen in scanned-angle or rocking curve measurements: Kiessig fringes. These result from the interference of waves reflecting from the top and bottom of the full multilayer, with thickness D_{ML}, leading to SW field maxima when $q\lambda_x = 2D_{ML}\sin\theta_q$, $q = 1, 2, 3\ldots$. Additional fine structure in a rocking curve can result from reflections at the top and bottom of the wedge, or some other thicker layer(s) in the sample, for which one simply replaces D_{ML} with $D_{effective}$ above.

The basic principle of the multilayer SW method, as amplified by including one wedge-profile layer in the sample, is illustrated in Fig. 16; this figure also includes some specific parameters for the first case studied: the Fe/Cr interface, a prototype system exhibiting giant magnetoresistance (GMR) [33]. A well-focussed soft X-ray synchrotron radiation (SR) beam at between 500 and 6000 eV energy is incident on a synthetic multilayer mirror at its first-order Bragg angle. This leads to a high reflectivity and a strong standing wave (SW) above the mirror. As noted above, if the bilayers making up the mirror (in this example composed of B_4C and W) have a thickness d_{ML}, then the period of the SW, as judged by the square of its electric field, also has a period of d_{ML}, as indicated in the figure. Beyond this, the fact that the SW modulation is the result of interference between the incident and reflected beams implies that its intensity will range over maximum limits set by $1 \pm 2\sqrt{R(\theta_{inc})} + R(\theta_{inc})$, where R is the reflectivity at a given incidence angle. Thus, even a modest reflectivity at the Bragg condition of 1% will yield an overall SW modulation of $\pm 2\sqrt{R} \approx \pm 20\%$ via the middle term in this expression. The sample to be studied is then grown on top of the mirror, with its base layer (here Cr) in a wedge profile, and another constant-thickness layer (here Fe), plus perhaps other layers, grown on top of the wedge. The slope of the wedge is such that, over the full sample length along the x direction in the figure, it changes in height z by a few times the standing wave period d_{ML}. Since the X-ray beam size is ~0.1 mm and much smaller than the typical sample length of ~1 cm, scanning the sample relative to the beam along the wedge slope (the x direction) effectively scans the standing wave through the sample. It is important in this context to note that the SW phase is fixed relative to the multilayer during such a scan. Thus, photoelectron or X-ray emission signals from different atoms will exhibit oscillatory behavior that can, in a direct-space manner, be interpreted in terms of depth distributions, with the aid of X-ray optical calculations to accurately simulate the standing wave [107,108].

In practice, this standing wave/wedge (swedge) method is also combined with the more standard SW methods for determining depth-resolved information perpendicular to a set of reflecting planes: scanning the incidence angle over the Bragg reflection condition for a given fixed photon energy, so as to generate a rocking curve, and scanning the photon energy over the Bragg condition for a given fixed incidence angle. In both of these types of scans the SW modulation is negligibly small at the outset well off the Bragg condition, then grows in to a maximum at the Bragg angle, and then decreases to a small value again. Simultaneously, the phase of the SW moves vertically by about 1/2–3/4 of the SW period, thus causing significant changes in photoelectron or X-ray emission intensities. Both of these measurements, combined with appropriate X-ray optical simulations, can be used to determine the Bragg angle at the outset of a swedge experiment, and they also provide complementary depth-resolving information that has been used together with x-coordinate scans along the wedge to finally determine the thickness of the wedge for a given x-coordinate setting, as well as final depth profiles. A distinct advantage of the swedge approach however, is that several full periods of the SW can be scanned through the sample, and the resulting very nearly sinusoidal oscillations more quantitatively analyzed to determine depth profiles. One feature of such oscillations that is particularly useful is the phase shift between them for different species, which can directly be read as an approximate indicator of position with respect to the surface of the sample. We illustrate this now for a few examples below, including both soft X-ray and hard X-ray excitation.

9.2. Application to a giant magnetoresistive interface

The first results obtained with the swedge method were for the Fe/Cr interface, and they are summarized in Fig. 17. In Fig. 17(a), the two basic types of measurement performed are indicated: (i) a scan of sample position along x with the incidence angle fixed at or near the Bragg angle, as discussed previously; and (ii) a rocking-curve scan of incidence angle through the Bragg angle at fixed x, or equivalently fixed Cr thickness. The results of both types of scans on the Cr3p/Fe3p intensity ratio are presented in Fig. 17(b) and (c). The roughly sinusoidal oscillations of this ratio in Fig. 17(b) clearly

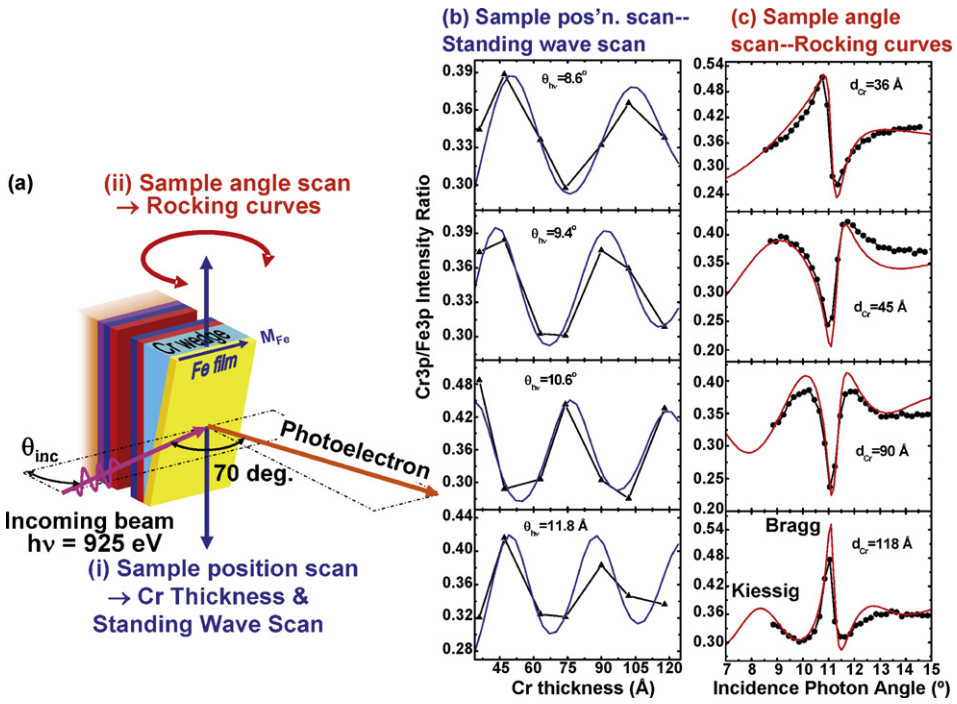

Fig. 17. (a) Two types of scans possible in the standing wave/wedge (swedge) method: (i) Scanning along x or wedge thickness with θ_{inc} fixed at the Bragg angle to yield a direct scan of the standing wave through the layers above the wedge, and (ii) scanning the incidence angle over the Bragg angle with x (or Cr thickness) fixed to yield a rocking curve. (b) and (c) Experimental (points) and calculated (curves) of the Cr3p/Fe3p ratios for these two types of scans, for the sample shown in Fig. 16 (from Ref. [33]).

reflect the passage of the standing wave through the interface. Fig. 17(c) shows the more complex forms that are characteristic of rocking curves, with dramatic changes in the ratio in this data also. There are easily measured modulations of approximately ±15 to ±25% in these ratios. Note also in Fig. 17(c) that the wings of the rocking curve contain Kiessig fringes that are observable in theory, and to a lesser degree in experiment, due to its limited angular range. Self-consistently analyzing the data in Fig. 17(b) and (c) with X-ray optical calculations of standing wave photoemission [107] and only two variable parameters (the depth of onset of the change in the Fe composition and the width of a linear gradient as the interface changes from pure Fe to pure Cr) yielded the excellent fit to both types of data shown in the figure, and permitted determining the position and thickness of the Fe/Cr interface [33]. Adding to this data Fe 2p, Fe 3p, Cr 2p, and Cr 3p MCD measurements (cf. Fig. 5(a)) as a function of position also permitted determining the depth profile of the magnetization of both atoms through the interface. Thus, in this first published example, the swedge method permitted non-destructively determining the concentration profile through an interface, as well as the variation of the element-specific magnetization contributions through it.

9.3. *Application to tunnel magnetoresistive interfaces*

As another example related to spintronics, we consider a prototypical magnetic tunnel junction (MTJ), in which two ferromagnetic layers (e.g. CoFe) are separated by an insulating layer (e.g. Al_2O_3 or MgO), and spin-dependent tunneling interactions can produce a large tunnel magnetoresistance (TMR). Fig. 18 summarizes photoemission data from a sample consisting of an Al_2O_3 wedge varying in thickness from 100 to 55 Å, a layer of CoFe of 25 Å thickness, a layer of CoFeB of 15 Å thickness, and a final protective cap of Al_2O_3 of 10 Å thickness [109]. In Fig. 18(a) is shown the B 1s spectrum, which is split into two components by a large chemical shift. These two components A and B can be verified as two chemically and spatially distinct species by either doing a rocking-curve scan and monitoring the two intensities A and B (Fig. 18(b)) or a scan along the wedge slope (Fig. 18(c)) in which the x position is fixed and the angle of incidence is varied, thereby sweeping the SW position through the sample. The two components A and B have markedly different behavior as a function of SW position. Analysis of the scans shown in Fig. 18(b) and (c), but in particular, the phase shift between the oscillations in Fig. 18(c), reveals that their mean depths are different by about 7 Å and that peak B originates from atoms closer to the surface. A quantitative X-ray optical analysis of both sets of data yields the concentration profiles responsible for these two peaks indicated in Fig. 18(d), and the conclusion that the boron of type B in the CoFeB layer has segregated out into the interface between CoFeB and the Al_2O_3 capping layer [109].

For the same MTJ sample type as in Fig. 18, it has also been possible to use several valence-band spectra obtained as the standing wave is scanned through the sample to yield layer-resolved densities of states, and in particular, to provide an understanding in terms of electronic structure of the marked increase in tunnel magnetoresistance (TMR) when the CoFe layer is decreased in thickness d_{CoFe} from 25 to 15 Å [110].

As another type of MTJ structure studied using the swedge method, we consider a system consisting of an Al_2O_3 wedge varying from 140 to 280 Å in thickness covered by a constant-thickness 15 Å Co layer and a 12 Å Ru cap [109]. One type of sample in this study was produced using a synthetic procedure involving a 30-s final plasma oxidation of the Al_2O_3 just before deposition of the Co, a procedure that has been thought to increase the desired TMR. For such a sample, the Co is found via Co 2p chemical shift analysis to be highly oxidized. Fig. 19(a) shows a reference Co 2p spectrum from the literature, with one sharp feature from metallic Co (Co^0) and two peaks from Co oxide (Co^{2+}) [111]. We find the same spectral features, as shown in the standing wave/wedge (swedge) scan in Fig. 19(b). In the same sense that the two boron species A and B in Fig. 18(a) have a phase shift in Fig. 18(c), so does the single Co metal component have a phase shift of about 16 Å relative to the two components from Co oxide in the Co^{2+} state, as shown clearly in Fig. 19(b). This shift is in turn in a direction indicating that the oxide is situated on average above the metallic Co, rather than below it

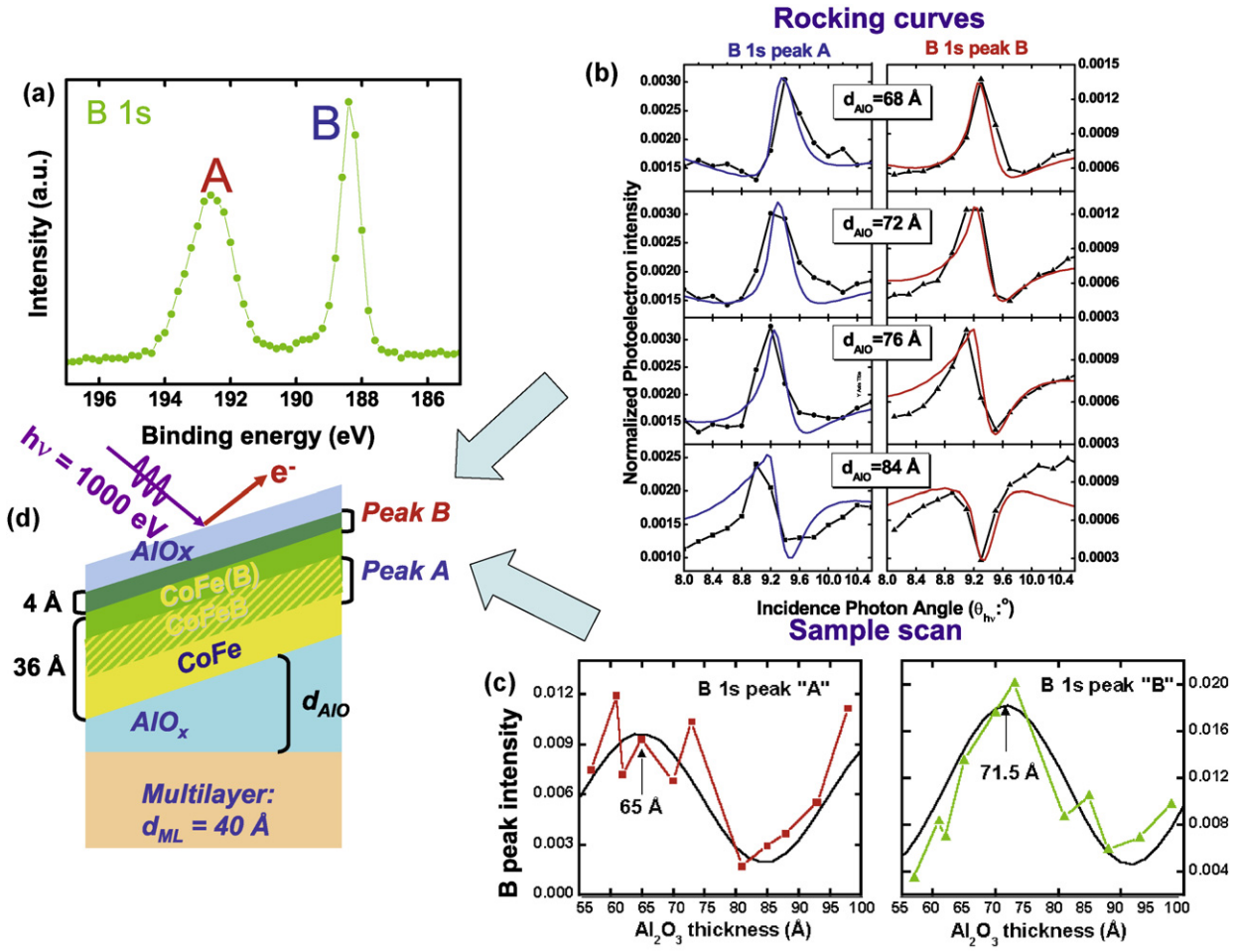

Fig. 18. (a) The boron 1s spectrum from a CoFeB layer on top of a sample with the configuration shown in (d). The photon energy was 1000 eV. (b) The intensity of the two components A and B in (a), obtained by rocking the sample, i.e., by scanning the X-ray incidence angle through the first-order Bragg reflection of the multilayer. (c) The variation of the intensities of peaks A and B as the standing wave is scanned through the sample by moving the sample in the *x* direction (a swedge scan). (d) The distribution of the two types of boron in the sample, as derived from a fit of X-ray optical calculations to the data, with the smooth curves in (b) and (c) representing best fits. Type A has segregated out at the top of the FeCoB layer, leaving a depleted FeCo(B) region. Type B represents boron in the FeCoB layer with original doping level (from Ref. [109]).

and adjacent to the Al_2O_3. Beyond this, the oscillatory patterns seen for the various core-level intensities of different atoms from this sample, as plotted in Fig. 20, yield a family of phase shifts which can be analyzed to determine depth distributions. For example, O 1s is split into what appears to be two metal-oxide components, one that is in phase with Co oxide and nearer to the surface, and one that is in phase with Ru that is below the surface. The metallic Co signal also seems to come from not very far below the Ru on average. These results thus point to a very strong intermixing and/or island formation in the Co and Ru layers, with the relative weakness of the Ru oscillations also suggesting that it has distributed itself over depths that must be approaching the wavelength of the standing wave, which was in this case 40 Å. An approximate picture of the sample profile is shown in the inset of Fig. 19(c), and it is very different from what might have been supposed from the synthetic recipe.

A final example, again of an MTJ structure, is of Fe/MgO and its interfaces, some further soft X-ray excited results from which are illustrated in Fig. 21 [112]. The sample configuration is shown in Fig. 21(a). An Fe wedge varying from 0 to 200 Å in thickness was grown on a Si/Mo multilayer mirror with 39.8 Å period, a 20 Å MgO layer was grown on top of this, and a 20 Å capping layer of Al_2O_3 was finally added to protect the MgO from radiation-induced chemical changes. In Fig. 21(b), the results of wedge scans of several core intensities, as well as the valence-band region are shown. Approximately two full cycles of passage of the SW through the sample layers are observed, with strong modulations of various features in the 20–30% range. Clear phase shifts of the peaks from Al, Mg, and Fe are seen, with these directly giving information on the relative depths of these species from the surface. Beyond this, the valence-band region shows clear changes as well, with the Fe-related DOS features near the Fermi level following the Fe 3p core level in modulation, such that the overlying oxide DOSs are more emphasized at points for which the Fe DOS is a minimum. Fig. 21(c) shows selected valence spectra from the data in (b), which make these changes more evident. Analyzing this data, together with MCD data for Fe 2p emission, has permitted deriving concentration and magnetization profiles through the Fe/MgO interface, as well as extracting the interface density of states for Fe, with the latter suggesting some Fe oxidation at the interface [112].

9.4. Standing wave photoemission with hard X-ray excitation

Beyond the studies mentioned before using Bragg scattering of harder X-rays from crystal planes to create a standing wave [31,32,104], another interesting area for future development is to use much harder X-rays for excitation of photoelectrons above a multilayer mirror, thus going from soft X-rays in the 500–1000 eV regime up to 5 or 10 keV. This would permit penetrating multilayer structures more deeply. It has been pointed out that standing

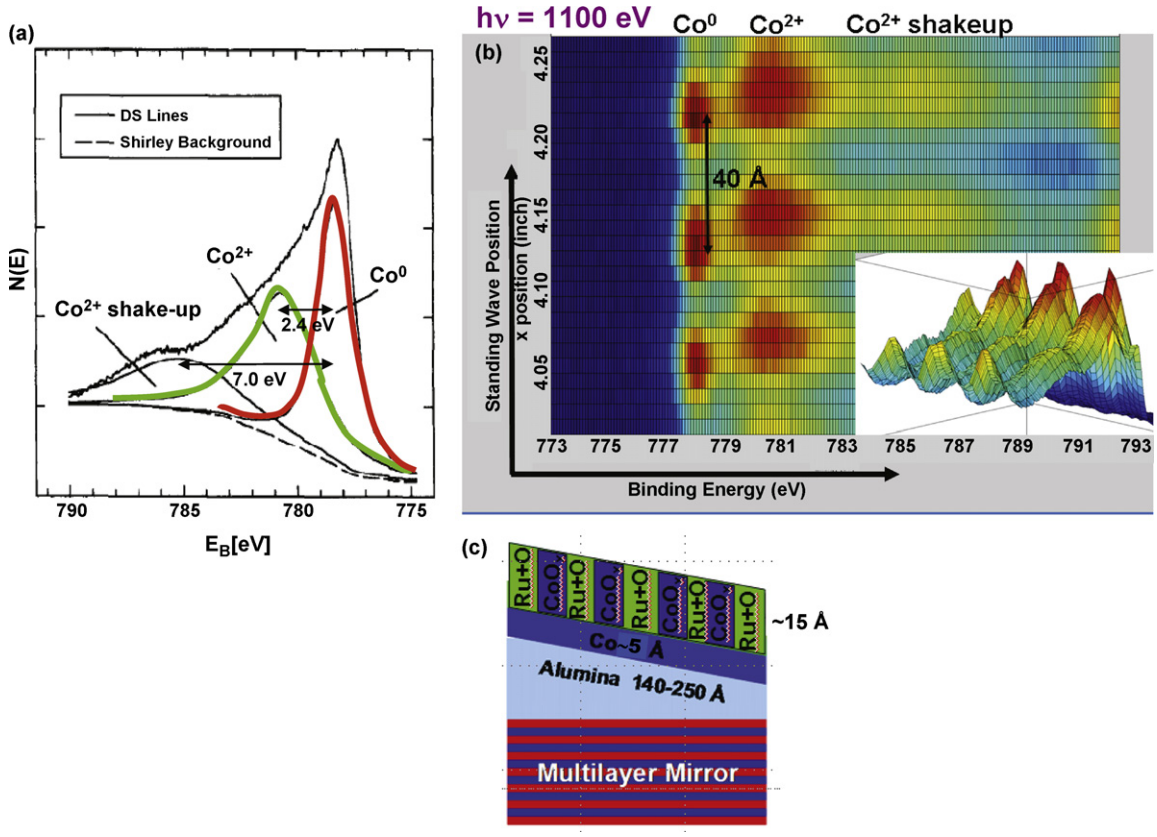

Fig. 19. (a) A Co 2p spectrum from oxidized Co, as obtained from the literature [111], indicating the three features expected: one from Co^0 and two from Co^{2+} (a main peak and a broad shake-up or screening satellite). (b) The effect of scanning the standing wave through a sample consisting of an Al_2O_3 wedge, a Co layer, and a Ru cap, on the Co 2p spectrum [109]. The photon energy was 1100 eV. Note the obvious phase shift between the Co^0- and Co^{2+}-associated peaks. (c) The approximate sample profile as deduced from the data in this figure and in Fig. 20 (from Ref. [109]).

waves above nm-scale multilayer mirrors should be even stronger in this higher-energy regime [113], and thus more accurate characterizations of even deeper structures should be possible. Some encouraging data of this type have in fact recently been obtained [114,115]. Fig. 22 summarizes some of the first data of this type for a sample with the configuration shown in panel (a), very close to that in Fig. 21. Photoelectrons were excited from this nanostructure with 4.0 keV photons [114]. As the X-ray beam is scanned along the wedge, Fig. 22(b) and (c) shows that there are strong oscillations of about 50% in magnitude in core photoelectron intensities arising from the oxide overlayers (Al 1s, O 1s (chemically shifted between the two oxides), and Mg 1s), with about four standing wave cycles

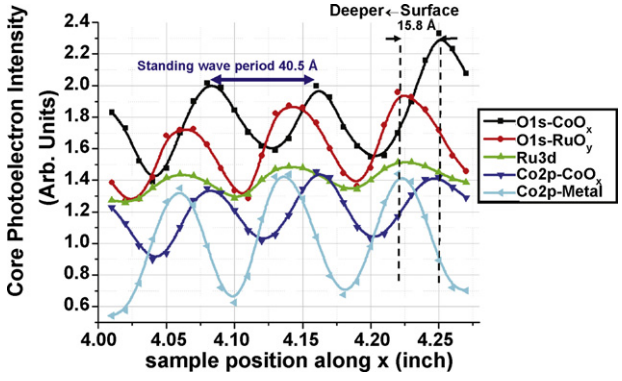

Fig. 20. (a) The oscillatory intensity variations of different core-level photoelectron intensities as the standing wave is scanned through a sample with the configuration shown in Fig. 19(c). The different peaks involved are indicated (from Ref. [109]).

being seen. The Fe oscillations are weaker, at only about 10% overall due to the greater thickness of the Fe wedge, the larger photoelectron IMFPs, and resultant averaging over a couple of SW cycles, but they are still visible, together with a phase shift due to the different effective sensing depths of Al, Mg and O, vs the Fe underneath. These data suggest another fruitful direction of development for HXPS in studying multilayer nanostructures, with applications already to Fe/MgO [114,115] and TiN/Si, a system of relevance to current semiconductor technology [116].

9.5. *Photoelectron microscopy in 3D with standing wave excitation*

As another possibility for the future, carrying out soft X-ray-excited photoelectron microscopy (PEEM) studies with standing wave excitation should provide a type of direct depth sensitivity to these laterally resolving synchrotron radiation based techniques, provided that one or more standing wave cycles can somehow be viewed in a single microscope image or series of images. Some first encouraging measurements of this type have in fact recently been carried out [117], as summarized in Fig. 23. As shown in Fig. 23(a), a multilayer-mirror substrate had grown on it a very narrow Ag wedge and then a bilayer of Co, then Au. This sample was then imaged in a photoelectron microscope, and the standing wave-induced variation of the intensity of a Ag wedge layer in the sample and a C contaminant overlayer could be seen in a single snapshot (Fig. 23(b) and (c)). The phase shift between the Ag and C images due to their different vertical positions relative to the SW is also seen in these figures. By further scanning the photon energy over the Bragg condition, the SW can be seen to move along the wedge

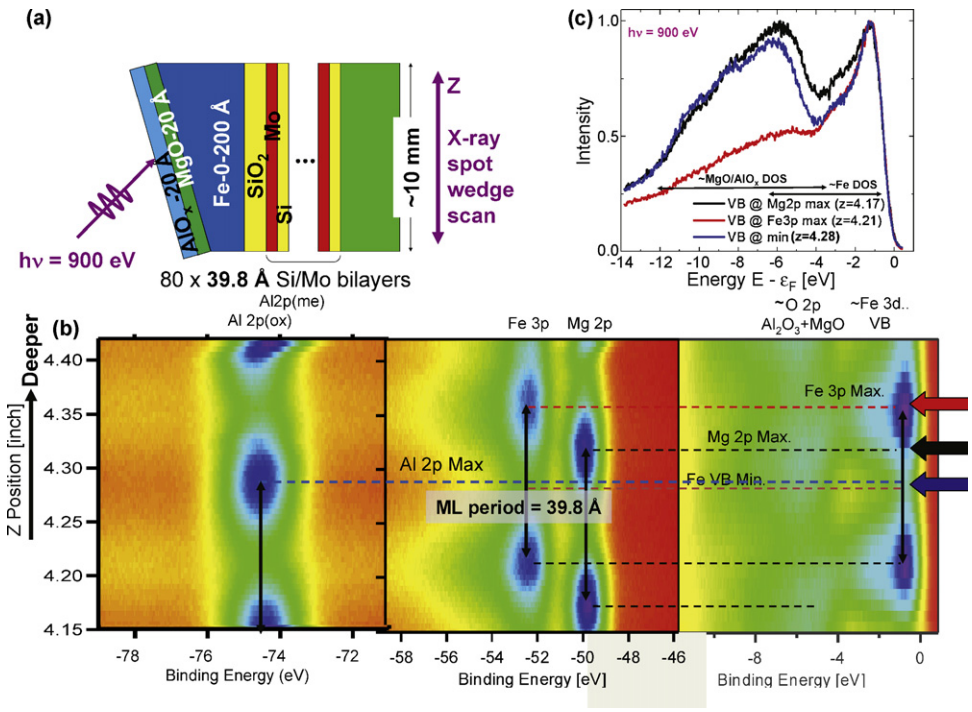

Fig. 21. Soft X-ray standing wave/wedge data for the MgO/Fe magnetic tunnel junction system, with excitation at 900 eV. (a) The sample configuration. (b) Variation of various core and the valence-band intensities as the X-ray spot is scanned along the wedge. The swedge geometry assures that adjacent maxima for a given level are spaced apart in height by precisely the SW period, here 39.8 Å. (c) Three selected valence-band spectra, at the points indicated by the arrows in (b), illustrating the different degrees of emphasizing the Fe DOS near the Fermi level vs the Al_2O_3 and MgO DOSs below their respective insulating band gaps (from Ref. [112]).

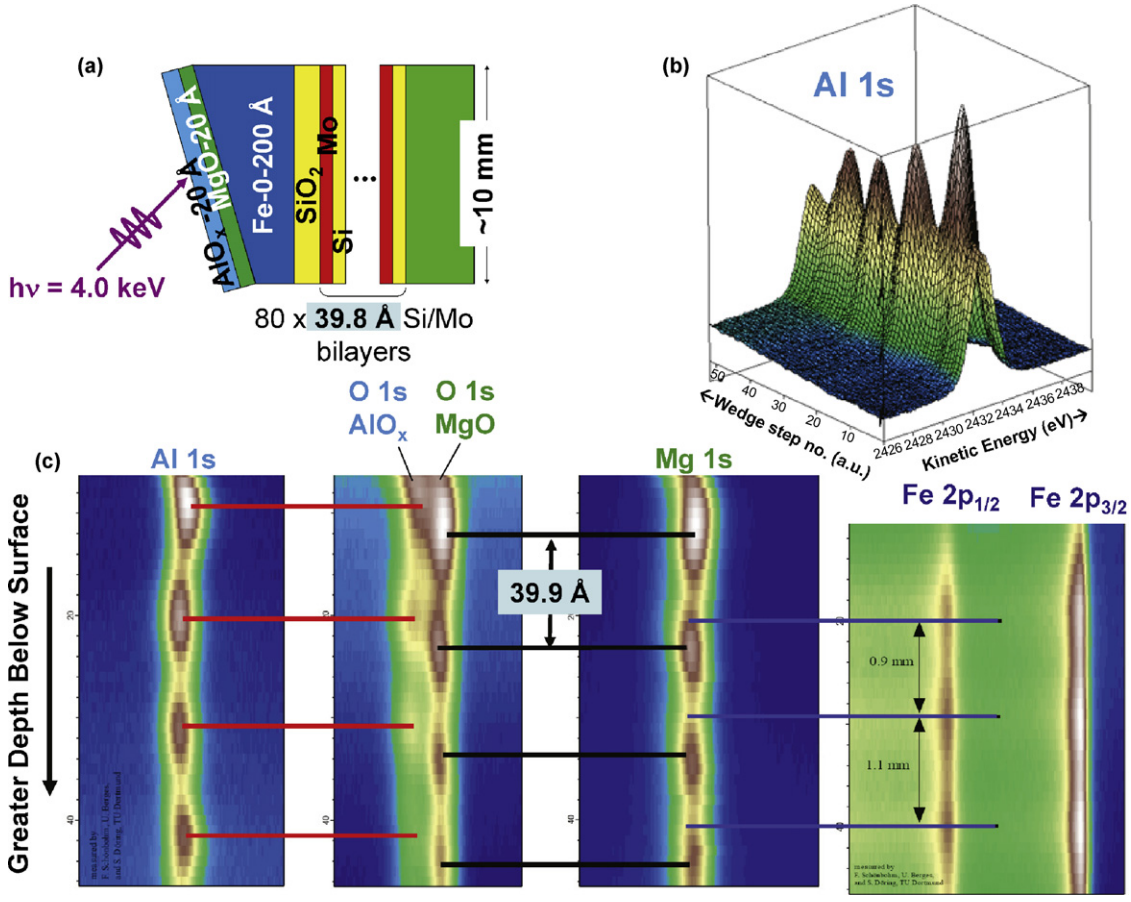

Fig. 22. Hard X-ray standing wave wedge data for the MgO/Fe magnetic tunnel junction system, with excitation at 4000 eV. (a) The sample configuration. (b) Variation of the Al 1s intensity as the X-ray spot is scanned along the wedge. (c) Variation of various core-level intensities as the X-ray spot is scanned along the wedge. The swedge geometry again assures that adjacent maxima for a given level are spaced apart in height by precisely the SW period, here 39.8 Å (from Ref. [114]).

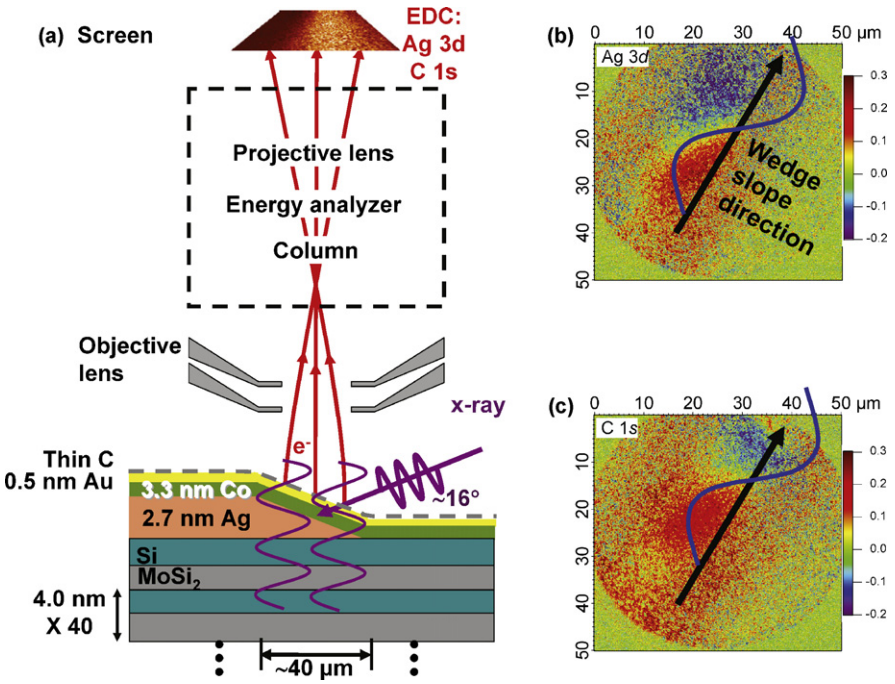

Fig. 23. (a) A schematic view of the first implementation of the standing wave/wedge (swedge) method in a photoelectron microscope, for the specific case of a Ag wedge below Co and Au layers, and with a C contaminant layer on top. (b) and (c) The difference of two PEEM images taken well above (602 eV) and on the Bragg reflection condition (590 eV), using the Ag 3d and C 1s intensities to produce the images in (b) and (c), respectively. The 590 eV photon energy is closest to the Bragg condition for the multilayer mirror. The difference images show ~20% modulation of photoemission intensity introduced by the SW. Note the phase shift between the two images due to the different vertical positions of Ag and C with respect to the multilayer mirror which generates the standing wave (from Ref. [117]).

[118]. In more recent experiments, simply scanning photon energy over the Bragg condition for a multilayer-based sample with no wedge present has also been found to yield a similar type of depth information [119].

Thus, the use of standing wave excitation in photoelectron microscopy should provide information on the third vertical dimension in images that have hitherto only been indirectly inferable from subtleties in core photoelectron or X-ray absorption spectra.

9.6. *Additional X-ray optical effects in XPS*

As an illustration of the rich variety of X-ray optical effects that can occur with hard X-ray excitation on a multilayer structure when the incidence angle is varied, Fig. 24 shows purely theoretical X-ray optical calculations for 6 keV X-rays incident on a model multilayer structure of relevance to exchange-bias, as shown in Fig. 24(a): a GaAs/AlAs multilayer with period 44.9 Å, on which is placed 200 Å of MgF_2 (modelling a seed layer for epitaxial growth), followed by 100 Å of FeF_2 (an antiferromagnet), 40 Å of Co (a ferromagnet), a 10 Å protective cap of Al, and finally a thin layer of oxygen contaminant to simulate the surface oxidation of Al [120]. In Fig. 24(b) and the blowup from it in Fig. 24(c), photoelectron intensities arising from all layers within the sample are plotted as a function of incidence angle, with various effects being seen: (1) rocking curves at the Bragg angle of 1.39°, (2) small closely spaced oscillations on either side of the Bragg rocking curve that are due to Kiessig fringes resulting from interference between waves reflecting from the top layer of the multilayer and from the bottom interface of it, and associated with the distance $D_{ML} = 60 \times 44.9\,Å + 40\,Å = 2694\,Å$, and (3) longer wavelength Kiessig fringes associated with the $MgF_2 + FeF_2 + Co$ layers, with an effective $D = 340$ Å. These fringes are evident in recent experimental rocking curve data using both soft X-ray (cf. Fig. 17(b)) and hard X-ray excitation, and can be used to check the thickness of the multilayer and the wedge + overlying layers, for example. As the onset of total reflection is approached at low incidence angles of ca. 0.5°, the photoelectron intensities rise due to a concentration of electric field near the surface, an effect first observed and explained by Henke [30a]. Finally, when total reflection is reached, they all fall to zero, but at different rates due to different onset angles of total internal reflection at buried interfaces that turn off the emission below them. Of course, this is also the regime in which total reflection XPS (TRXPS, GIXPS) is already being exploited [30], as overviewed by Kawai in this issue. It is now interesting to look at the precise form of the electric field squared as a function of depth at a few special points in angle. For angle "1" of 0.3° in the total reflection regime, as shown in (d), there is little penetration below the Co layer, and intensities would be sensitive to the Co/FeF_2 interface. For angle "2" of 0.375°, as shown in (e) the electric field exhibits a "waveguide" effect due to multiple scattering of the radiation at the top and bottom surfaces of the relatively low optical density MgF_2, and the field strength is much greater in this layer, with a resulting dramatic spike in the intensity from it in panel (b). The angle 0.375° is furthermore very close to the angle 0.298° which one gets for first-order multiple internal reflection inside the 200 Å-thick MgF_2 layer. Combined with the observed onset of total reflection at the top GaAs layer seen in Fig. 24(b) at very nearly the same angle, this explains semi-quantitatively the strong waveguide effect observed. Such waveguide effects have in fact been observed in hard X-ray fluorescence experiments previously [121]. For the last special case of the Bragg angle, as shown in Fig. 24(f), a strong standing wave with the period of the multilayer is created, with this being the topic of most of the prior discussion in this section. Although these results are based on theory only, they are expected to be an accurate representation of experiment in the absence of any threshold absorption resonance excitations. Thus, interesting variations in the field form with incidence angle such as those seen in Fig. 24 should also be very useful in future and soft and hard X-ray experiments on multilayer structures, permitting one to tailor the radiation profile so as to emphasize different por-

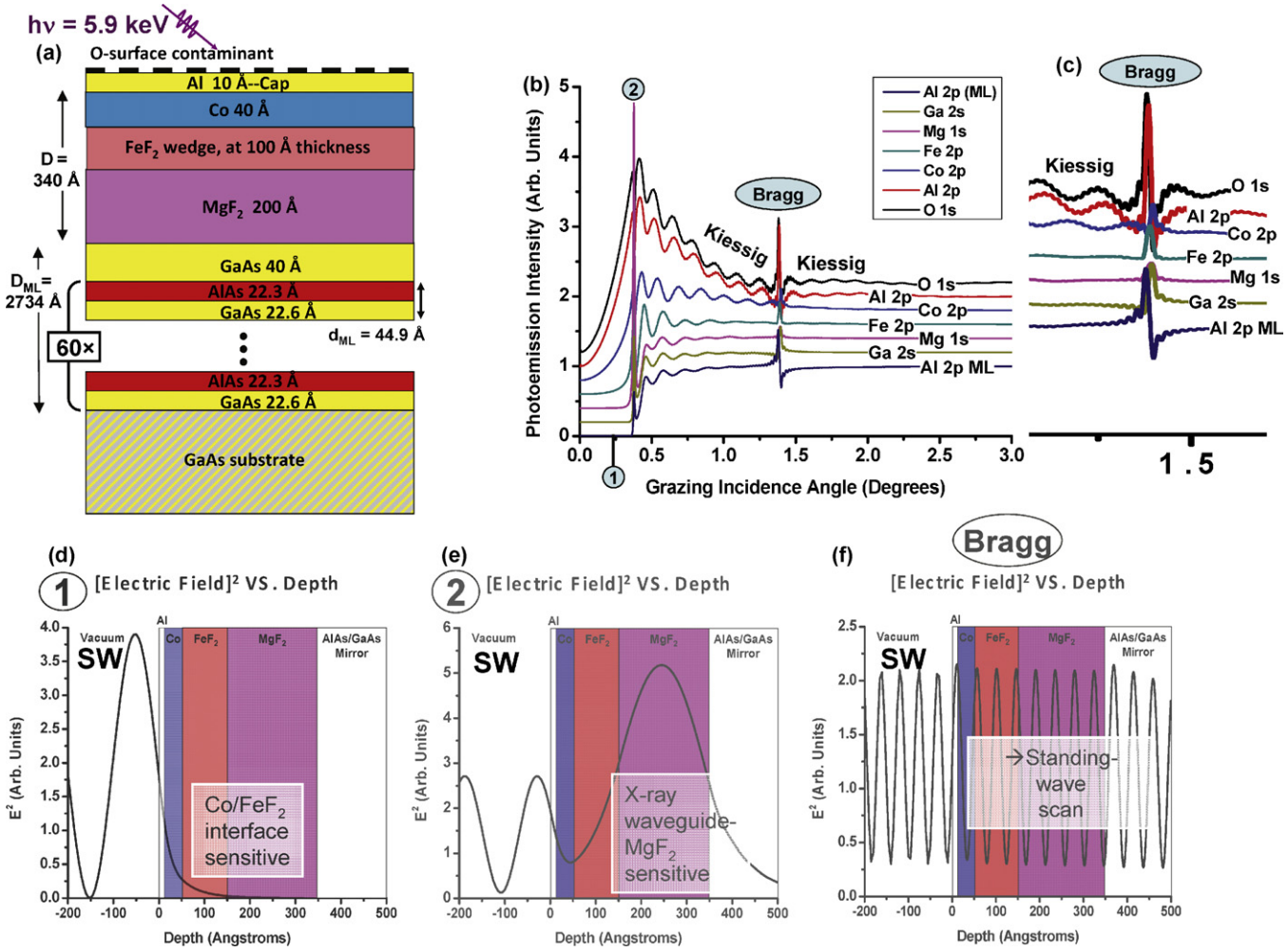

Fig. 24. Theoretical X-ray optical calculations using a program due to Yang [107] for the angular dependence of photoelectron intensities and electric field for 5.9 keV photons incident on a hypothetical sample involving exchange-bias between Co and FeF_2, and grown on a GaAs/AlAs multilayer of 44.9 Å period. (a) The sample configuration. (b) Photoelectron intensities from core levels in every layer of the sample, normalized to unity at 3.0° incidence angle, and shifted by 0.2 with respect to one another to avoid confusing overlap. (c) A blowup of the region around first-order Bragg reflection from the multilayer, indicating more clearly the two types of Kiessig fringes expected from such a structure, and associated with the distances D_{ML} and D in (a). (d) The depth dependence of the electric field squared for an incidence angle for which total reflection from the Co/FeF_2 interface has just turned on. (e) As (d), but for an incidence angle in which an X-ray waveguide effect has greatly enhanced the field inside the MgF_2 layer. (f) As (d), but for incidence at the first-order Bragg angle of the multilayer. Standing waves (SW) are created in all cases in the vacuum above the sample as well (from Ref. [120]).

tions of the sample. Carrying out such measurements does require a very narrow angular divergence of the incident beam, however, and thus such experiments are best done with synchrotron radiation.

10. Angle-resolved photoemission in the soft and hard X-ray regime

10.1. The basic ARPES measurement in the UPS limit

At lower energies of excitation, especially below roughly 100 eV, photoemission spectra are routinely used to map the band structure of solids and surfaces, and this is one of the most powerful applications of photoelectron spectroscopy. This ability is due to the fact that the excitation can be considered to be dominated by so-called "direct transitions" (DTs) in which an occupied initial one-electron Bloch-wave state $\varphi(E_i, \vec{k}_i)$ at energy E_i and wave vector $\vec{k}_i$ can in the dipole limit only make a transition to a final state with wave vector $\vec{k}_f = \vec{k}_i + \vec{g}_n$, where $\vec{g}_n$ is some reciprocal lattice vector associated with the crystal structure under investigation, and n represents a general set of $h\,k\,\ell$ indices. The relevant vector conservation equation is illustrated for the examples of soft X-ray and hard X-ray excitation from tungsten in Fig. 25. This figure also indicates that, as the photon energy is increased, one can no longer neglect the momentum of the photon $\vec{k}_{h\nu}$ in conserving wave vector, one manifestation of non-dipole effects in the excitation [25,26,122]. Determining $\vec{k}_f$ inside the surface from a measurement of $\vec{K}_f$ outside the surface (which will be slightly different from $\vec{k}_f$ inside due to crossing the inner potential V_0 at the surface) and then the set of $\vec{g}_n$ vectors which project $\vec{k}_f$ back into the reduced Brillouin zone (BZ) in which the band structure is usually described thus permits directly measuring $E_{binding}(\vec{k}_i) = E_i(\vec{k}_i)$, the band structure, or if final-state screening and many-electron excitations are taken into account, more properly the spectral function as calculated from some sort of many-electron theory [6]. A convenient expression of wave-vector conservation is thus:

$$\vec{k}_i = \vec{k}_f - \vec{k}_{h\nu} - \vec{g}_n. \tag{6}$$

If the final photoelectron state is high enough in energy, it can be approximated as a free-electron, with $E_f(\vec{k}_f) \approx p_f^2/2m_e = \hbar^2 k_f^2/2m_e$, where m_e is the electron mass.

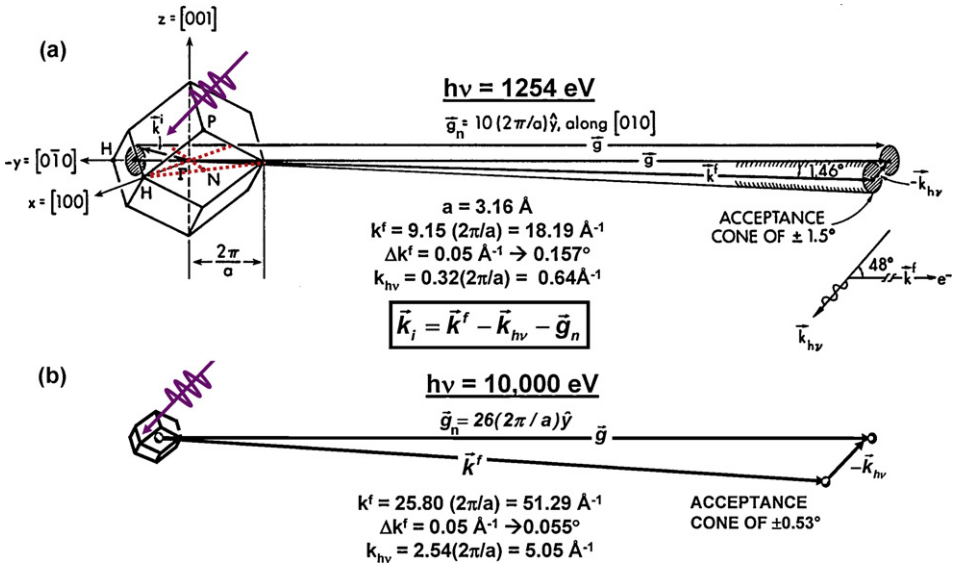

Fig. 25. Illustration of $\vec{k}$ conservation in valence photoemission from W at two different photon energies: (a) 1253.6 eV, a typical soft X-ray energy also available with laboratory sources, and (b) 10,000 eV, a hard X-ray energy that is of interest for the future. Note the basic wave-vector conservation law, which must include the photon wave vector for energies above ~100 eV (from Refs. [113,122]).

10.2. Hard X-ray angle-resolved photoemission (HARPES): densities of states and band mapping

We have already noted that the combined effects of phonon excitations during photoemission and angular averaging in the spectrometer often lead in measurements at 1 keV or higher excitation energies spectra that represent a matrix-element weighted density of states (DOS), the XPS limit (cf. Fig. 9). A measure of how completely phonon effects have contributed to this DOS limit is a temperature-dependent Debye–Waller factor ($W(T)$) calculated for the relevant $\vec{g}_n$, which roughly represents the fraction of direct transitions remaining [122]. This factor can be calculated from $W(T) \approx \exp[-g^2 < u^2(T) >]$, with $< u^2(T) >$ the one-dimensional mean-squared vibrational displacement at temperature T. To illustrate the XPS limit for very small $W(T)$, Fig. 26 shows two comparisons of experiment and theoretical densities of states for Au with excitation energies of 1487 eV (Al Kα) [123] and 5.5 keV in the hard X-ray regime [124]. The relevant $W(T)$ values are ~0.04 for 1487 eV excitation and $\sim 5 \times 10^{-6}$ for 5.5 keV, so one expects to be in the XPS limit in both cases. In both panels, the density of states as calculated from local-density theory is compared to experiment [125]. Although there are subtle differences between experiment and theory, probably due to matrix-element effects, it is clear that high-energy photoemission provides a rather direct measure of the DOS.

It is also important to note that, since the XPS limit in its simplest interpretation measures a matrix-element weighted DOS, the two panels in Fig. 26, or indeed in any comparison of spectra with soft X-ray and hard X-ray excitation, will represent different weightings of the atomic orbital character of the valence bands. More quantitatively for the case of Au, the relevant subshell photoelectric cross-section ratios between the two photon energies are: Au6s/Au5d = 0.012 at 1.5 keV and 0.028 at 6 keV [19], with the relative influence of Au 6s thus expected to be about 2.3 times higher at 6 keV. This is in fact seen in Fig. 26, via the enhanced relative intensity of the 6s-dominated region over about 0–1.5 eV binding energy, as compared to the 5d-dominated features over 2–8 eV binding energy. More generally, subshells with lower angular momentum quantum number ℓ are favored at higher energy, due to the increased number of oscillations in their radial wave functions, and thus better non-zero overlap with the strongly oscillatory photoelectron radial wave function in the calculation of a matrix element.

Beyond densities of states however, it is also interesting to assess whether more bulk-sensitive band mapping is possible by using energies beyond the usual ARPES range up to ~150 eV, and going up into the keV, or even multi-keV regime. Several papers exploiting this in the 500–1000 eV range have in fact already appeared [66,126–130]. As an example of the competing physics involved in doing this, we consider an intermediate case for which both band mapping and phonon smearing are involved: photoemission from tungsten with ~1 keV excitation. Fig. 27(a)–(d) shows a set of angle-resolved data from $W(1\,1\,0)$ obtained in near-normal emission with an intermediate energy of 870 eV, and at four different temperatures, which permits assessing the influence of phonons in a more quantitative way [66]. The four experimental panels all clearly show band-mapping features, and in fact can be shown by simple free-electron final-state calculations to sample along the Γ-to-N direction in the BZ, one of the directions highlighted in Fig. 25(a). It is also clear that raising the temperature stepwise from 300 to 780 K, or from 0.75 times the tungsten Debye temperature to 1.95 times that temperature involves a smearing of those features and a significant gain of intensity in other parts of the angle-resolved data. Also shown for comparison to experiment in Fig. 27(e)–(h) are the results of one-step photoemission calculations that go beyond the three-step model in many respects and include matrix-elements effects [131], a level of theory also discussed by Fujikawa in this issue. These calculations agree very well with the positions and intensities of all features seen in experiment, with some special points labelled 1, 2, ... 6 in experiment, and 1′, 2′ ... 6′ in theory. However, these calculations do not at their present level correctly predict the smearing of features at higher temperatures due to phonons [66]. Further work is clearly needed in the theory of X-ray excited ARPES so as to adequately describe these phonon effects; this would permit more quantitatively using such data to study bulk electronic structures in a variety of materials.

As a further example of such higher-energy ARPES, Fig. 28(a)–(b) compares experiment and one-step theory, again for $W(1\,1\,0)$, but this time with excitation at a higher energy using non-monochromatized Mg Kα radiation at 1253.6 eV and cooling to liquid nitrogen temperature to reduce the phonon effects [132].

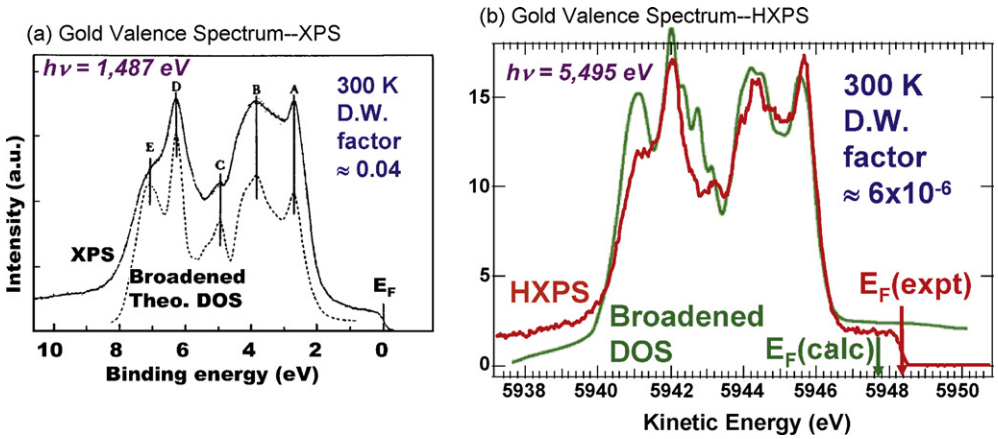

Fig. 26. Valence photoelectron spectra from the noble metal Au in the XPS or density of states (DOS) limit. In (a) and (b), Au spectra with 1.5 keV (from Ref. [123]) and 5.5 keV (from Ref. [124]) excitation, respectively, are shown. In both cases, the experimental results are compared with theoretical densities of states based on local-density theory; in (b) these are from Ref. [125].

In the measurements, the sample angle θ was varied in steps that were a little smaller than the ~20° window spanned by the detector in $\vec{k}$ (cf. Fig. 1), such that the detector images could be tiled together in an overlapping way over a range of about 50°. The agreement with one-step theory here is again excellent, both as to the positions and the relative intensities of the excitation from different bands. There is some disagreement in angular positions for the largest positive angles relative to the [110] surface normal, but this is probably due a slight misalignment of the crystal relative to that assumed in the calculations. Finally, in Fig. 28(c), the actual $\vec{k}_f$ excursion in this experiment is shown, as calculated based on simple free-electron final states. Over the angle range of the experiment, the reduced Brillouin zone is spanned about 5 times via five different reciprocal lattice vectors $\vec{g}_n$, $n = 1, 2, \ldots 5$, starting out for small angles along the face of the Brillouin zone along H-to-N-to-H and finally moving to scan more along H-to-Γ-to-H, as indicated by two additional dashed lines in the Brillouin zone in Fig. 25(a). These results make it clear that one can do three-dimensional band mapping in this way, and with greater bulk sensitivity. Varying photon energy for a fixed emission-angle

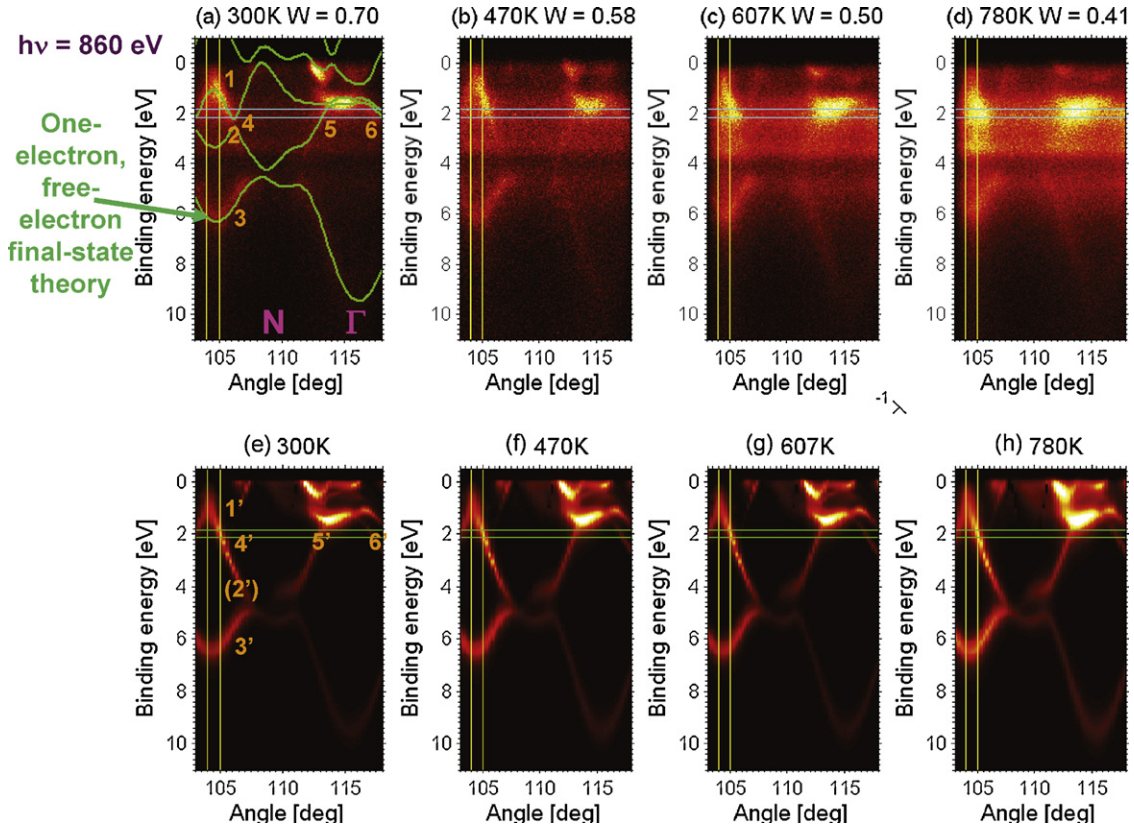

Fig. 27. Temperature-dependent angle-resolved photoemission data from $W(1\,1\,0)$ at an excitation energy of 860 eV. (a)–(d) Experimental energy-vs-angle (energy-vs-$\vec{k}$) plots at four temperatures, with phonon-induced smearing of features evident as T is raised. From left to right in each, the N-to-Γ line in the Brillouin zone (cf. Fig. 25(a)) is approximately sampled. In (a) the results of a simple free-electron final-state estimate of the spectra with no matrix elements included are shown as the green curves. (e)–(h) Theoretical calculations of these results based on a one-step model including matrix elements, and allowing for phonon effects via the approximation of complex phase shifts (from Ref. [66]).

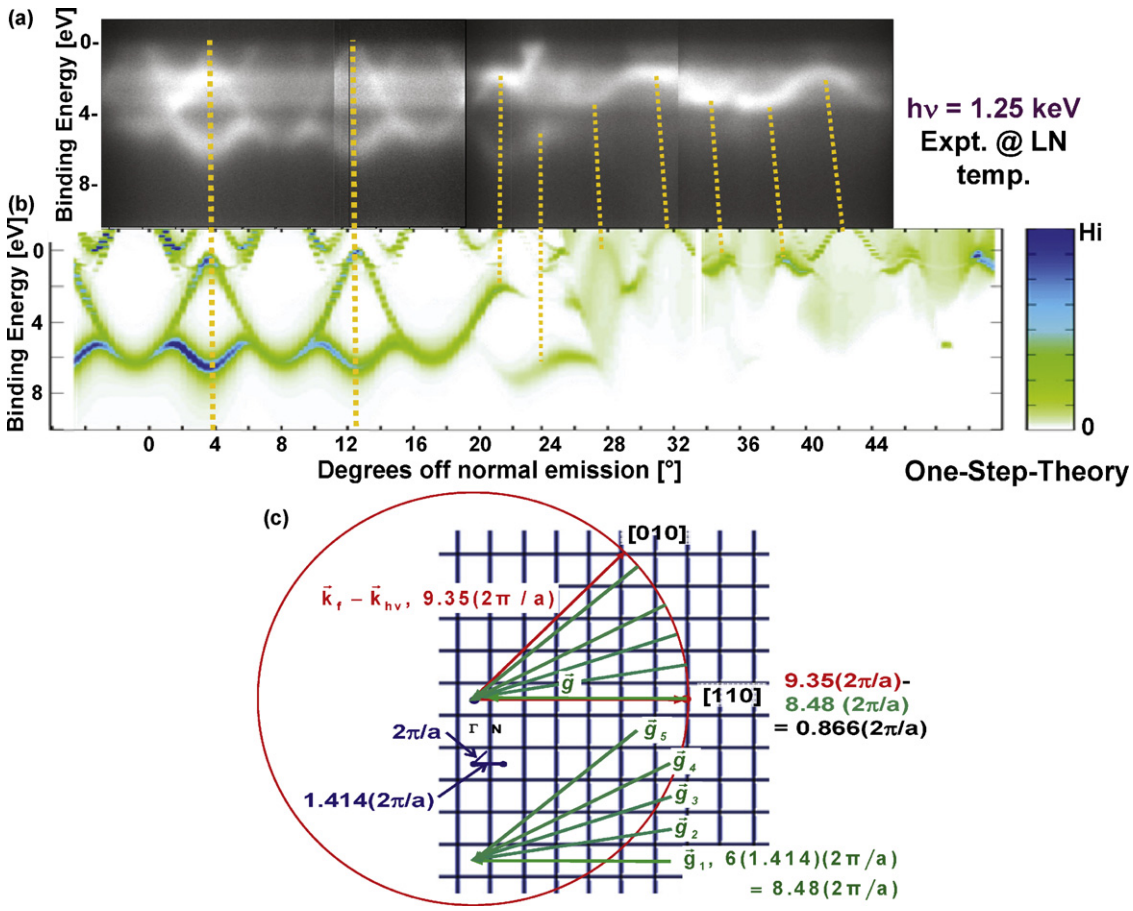

Fig. 28. Angle-resolved photoemission data obtained from $W(1\,1\,0)$ with non-monochromatized Mg Kα radiation and at 77 K. The experimental data in (a) were obtained by rotating the sample in θ and tiling several $E - \vec{k}$ images in the detector (cf. Fig. 1(c)). The one-step theory with matrix elements included in (b) is based on the same method used in Fig. 27 [66,131]. There is in general excellent agreement as to both positions and relative intensities, with the dashed lines being guides to the eye in comparing experiment and theory. Some angular shifts between them for larger angles are probably due to a slight misalignment of the crystal. (c) The region in $\vec{k}$-space spanned by these measurements. By thus scanning the emission direction over a range of about −5° to +45° relative to the [110] surface normal, the $\vec{k}$-point sampling in the Brillouin zone involves five different reciprocal lattice vectors $\vec{g}_n$ and thus five different sampling arcs, as indicated by 1, . . . 5 in the reciprocal space drawing (From Ref. [132]).

range is another method for doing three-dimensional band mapping.

As a final example here, we show in Fig. 29 truly hard X-ray ARPES from $W(1\,1\,0)$ as measured at two temperatures, 300 and 30 K, and excited by 5.9 keV photons obtained from the SPring8 synchrotron radiation source [133]. In the detector images shown, 39–40 channels equal 1°, so each image spans about 12°. Fig. 29(a) shows a detector image at 300K, for which $W \approx 0.09$, a situation expected to yield the XPS limit. Indeed, no dispersive features are seen, and the EDC at any angle is found to closely resemble the W DOS, with the three most prominent peaks indicated by arrows in the figure. Fig. 29(b) shows results after cooling to 30K, for which $W \approx 0.45$, and approximately half the intensity is thus expected to be involved with direct transitions. For this case, dispersive features clearly appear, although they are superposed with DOS features. However, in both panels (a) and (b), the DOS-like intensity exhibits modulations with angle that can be as much as 30%. These are simply hard X-ray photoelectron diffraction effects, as has been seen before with soft X-ray excitation of valence bands for cases in the XPS limit [134]. Thus, both dispersing band effects and XPD effects can be seen in the same dataset, with relative amounts depending on temperature and photon energy.

The raw low-temperature image in Fig. 29(b) has then been corrected with a two-step procedure that involves dividing by the detector window average over energy (to approximately correct for XPD effects) and by the window average over angle (to approximately correct for DOS effects) [135], with the final result being shown in Fig. 29(c). The dispersive features are much clearer in this corrected image, and suggest this procedure as a general method that should be useful for any systems for which W is less than approximately 0.5. Fig. 29(d) now presents one-step photoemission calculations with matrix-element effects included, and the agreement is very good. Finally, Fig. 29(e) shows the region in $\vec{k}$-space involved in these measurements. The image is expected to span the Γ-to-N-to-Γ direction, as indicated also in Fig. 29(c). Fig. 29(e) also shows that the effect of the photon momentum for this case is by chance to shift the image in $\vec{k}$-space by very nearly the Γ-N-Γ distance (4.35° compared to 4.21°, respectively), so the forward scattering peak along [110] in Fig. 29(a) lines up almost exactly with the Γ position in the dispersing bands. In general, this would not be true.

The results of Figs. 27–29, together with more recent results for GaAs(1 0 0) at 3.2 keV [133], thus clearly indicate that it should be possible to carry out more bulk-sensitive electronic structure studies at much higher photon energies than have been typically employed in the past. Estimates for a number of elements based on Debye–Waller factors in fact indicate that, with cryogenic cooling to suppress phonon effects, it should be possible to carry out more bulk-sensitive band mapping for many materials at up to a few keV, if not higher [66,136]. For example, Fig. 30 shows isocontour plots for $W = 0.5$, corresponding to an estimated 50% of direct transitions, at a sample temperature of 20 K that can be reached by many cryo-

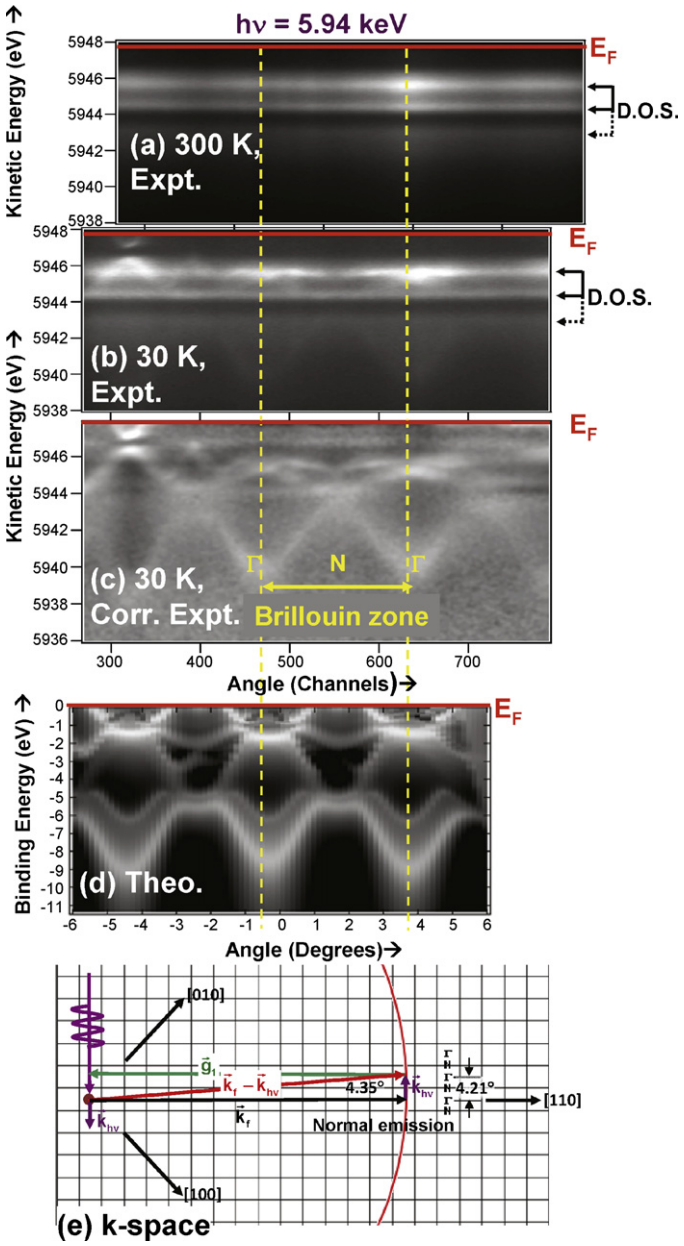

Fig. 29. The first hard X-ray angle-resolved photoemission data, for the specific case of $W(1\,1\,0)$ excited with 5.94 keV excitation. (a) Detector image as recorded at 300 K, very close to the XPS limit, and showing XPD modulation of the density of states (DOS), whose three primary peaks are indicated by arrows. (b) Detector image as recorded at 30 K, exhibiting both XPD-DOS and dispersive band features. (c) Corrected image from (b) after division by both the energy average and the angular average to enhance dispersive band features [135]. (d) One-step photoemission theory including matrix-element effects. (e) Free-electron final-state picture of the region sampled in $\vec{k}$-space (from Ref. [133]).

genic sample holders, as a function of photon energy and the two sample-related parameters Debye temperature and atomic mass. This plot can be used for any material for which the Debye temperature and the effective atomic mass are known. Also indicated by points are the actual values for about 34 elements. From this data, it is clear that band mapping should be possible in the 1–2 keV range, with the results for graphite also suggesting that layered materials may exhibit very different degrees of phonon involvement in-plane and perpendicular-to-plane. In addition, for GaAs, bands have been resolved with a lower W value of 0.35 [133], so the estimates in this figure are if anything conservative, with higher energies in the few keV range likely being usable for many systems. It is also expected that better procedures for correcting for the photon-associated DOS-like features will be developed, along with better microscopic theoretical treatments of such phonon effects [66], thus extending the energy range even further.

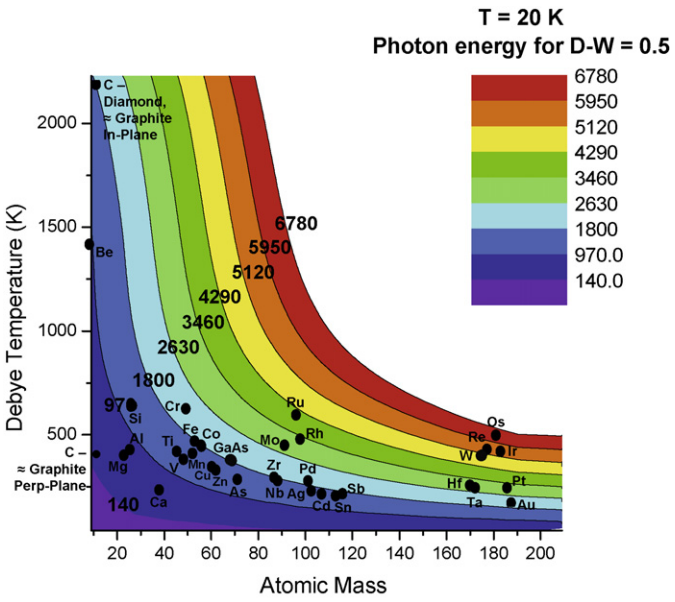

Fig. 30. Theoretical calculations of Debye–Waller factors W for angle-resolved photoemission, showing isocontours for $W = 0.5$ at a temperature of 20 K, as a function of Debye temperature, the atomic mass, and the photon energy. Results are shown for 34 elements, including three entries for carbon: diamond, graphite-in plane, and graphite-perpendicular-to-plane. The Debye temperatures used are for 300 K, with the exception of graphite (from Ref. [136]).

10.3. Nanometer-scale angle-resolved photoemission

As Fig. 1(g) indicates, other dimensions of photoemission involve adding *spatial resolution in the lateral dimensions x and y*, with one method for achieving additional resolution in the *vertical z dimension* via standing waves already being discussed in a prior section. Photoelectron microscopy or more generally "spectromicroscopy" is reviewed in detail by Margaritondo and by Oelsner in this issue, and in other recent overview articles [35–37]. Thus, we will here only specifically consider one future direction involving focussing the radiation to a small spot so as to do what has been termed "nano-ARPES" [135].

In Fig. 31(a), the basic idea of the experiment is presented [135]. A zone-plate lens is used to focus a soft X-ray synchrotron radiation beam down to a spot of the order of 100 nm. A spectrometer like that shown in Fig. 1 is then used to measure spectra from various regions of the sample by raster-scanning the sample in front of the beam in x and y. Both core and valence-level spectra can be accumulated in this way. Fig. 31(b) shows a micrograph from a cleaved sample of highly oriented pyrolytic graphite (HOPG) in which the intensity in valence-band spectra has been used as a contrast mechanism. Looking in more detail at the ARPES spectrum excited with 180 eV photons from the specific 300 nm region indicated reveals in Fig. 31(c) the band structure of the HOPG in that region. It is furthermore observed that the contrast comes about due to a slight tilting of different polycrystalline domains, with the brighter (yellow) regions corresponding to the so-called π-band of graphite being oriented towards the detector. Thus, one can look forward to taking advantage of much of what was discussed above with lateral spatial resolutions that should eventually reach 20 nm or better. In addition, spectromicroscopes making use of sophisticated electron optical elements promise to permit photoemission measurements below 10 nm, and perhaps at a few nm [137,138],

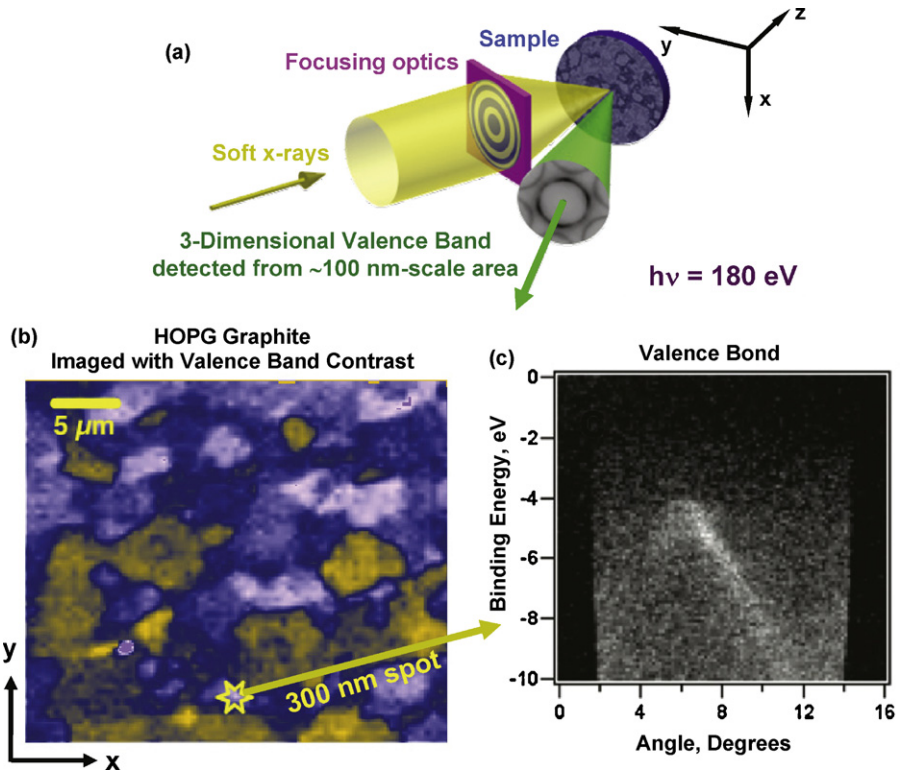

Fig. 31. Some first experimental results for spatial- and angle-resolved photoemission: nano-ARPES. (a) The basic experimental geometry, with a zone-plate used to focus the radiation into a small spot. (b) An image obtained by scanning the sample in front of the spot in *x* and *y*, with contrast provided by the intensity of the valence-band spectra, as excited by 180 eV radiation. (c) Angle-resolved photoemission results obtained from a 300 nm region indicated in (b) (from Ref. [135]).

although perhaps not with the energy and angular resolution of the zone-plate scheme in Fig. 31. Going to higher photon energies as discussed in the prior section should also yield more bulk-sensitive electronic structure, but with two-dimensional imaging.

10.4. Bonding interactions and band structures in core levels

As a final aspect of ARPES, we should note an only very recently discovered effect, the observation of weak bonding interactions in deep core levels of solids, and resultant "band structures" [139]. In particular, combined C 1s XPD and C 1s ARPES measurements on graphene show that, although C 1s is nominally a core level that is not involved in chemical bonding, there are interatomic interactions of sufficient strength to mix adjacent orbitals in bonding and anti-bonding combinations, thus forming long-range Bloch functions that exhibit dispersion with wave vector [139]. The magnitudes of these dispersions are small, at 60 meV overall, but nonetheless observable via high-resolution measurements at photon energies of 350–700 eV. Such effects are in fact not surprising, as they are the solid-state analogues of effects that have been known in simple molecules such as acetylene (H–C–C–H) [140] and N_2 for some time [141]. This phenomenon thus represents another example of the fruitful cross-fertilization that often takes place between atomic and molecular physics and condensed matter physics.

It is thus expected that such effects will be seen in high-resolution measurements of core levels in many other systems, and that they could in fact influence the overall linewidths in core spectra at the 50–100 meV level.

11. X-ray photoemission at high ambient pressure

I have previously mentioned XPS measurements at higher pressures in the multi-torr regime, but it is worthwhile here to consider a few illustrative examples of recent results.

As one aspect of XPS at higher pressures, we first consider the monitoring of surface chemical reactions in real time. Beginning with some first exploratory studies by Nilsson et al. in Uppsala [142] and by Grunze and co-workers [143], work in several laboratories has by now extended such reaction kinetics studies with synchrotron radiation excitation to faster timescales and more complex chemical reactions [144,145], as well as to higher effective ambient pressures [82,83,146], thus permitting studies of such systems as aqueous surfaces [146] and solutions [147] and catalytic reactions [148]. This represents yet another exciting and rapidly developing area for future studies with X-ray photoelectron spectroscopy.

As a technologically relevant example of these types of time-resolved reaction studies, Fig. 32(a) shows a high-resolution spectrum of an oxidized Si(0 0 1) surface, with the well-known resolution of at least five distinct chemical states from the element to that of SiO_2 [149]. Such spectra have previously been used to study the kinetics of oxidation of Si at pressures of about 10^{-6} Torr, with resolution in time of all of the oxidation states. As a more recent development, Fig. 32(b) shows a first high-pressure XPS system in which the sample could be separated from the exciting synchrotron radiation beam by a thin Al (or SiN) window and from the analysis section of the electron spectrometer by an electron lens with two stages of differential pumping [82]. This configuration permits having the sample region at up to a few torr in pressure during measurements. In this way, surface reactions can be studied at pressures that in some cases are much closer to the actual conditions of industrial processes or systems of relevance to environmental science, thus bridging what has been called the "pressure gap" between ultrahigh vacuum surface science research and real-world reaction conditions, and leading to the term "ambient pressure photoemission spectroscopy (APPS) for this technique [83]. As an example of the use of such a system, Fig. 32(c) shows several spectra from a very recent Si oxidation study at 450 C and 1 Torr which is of relevance

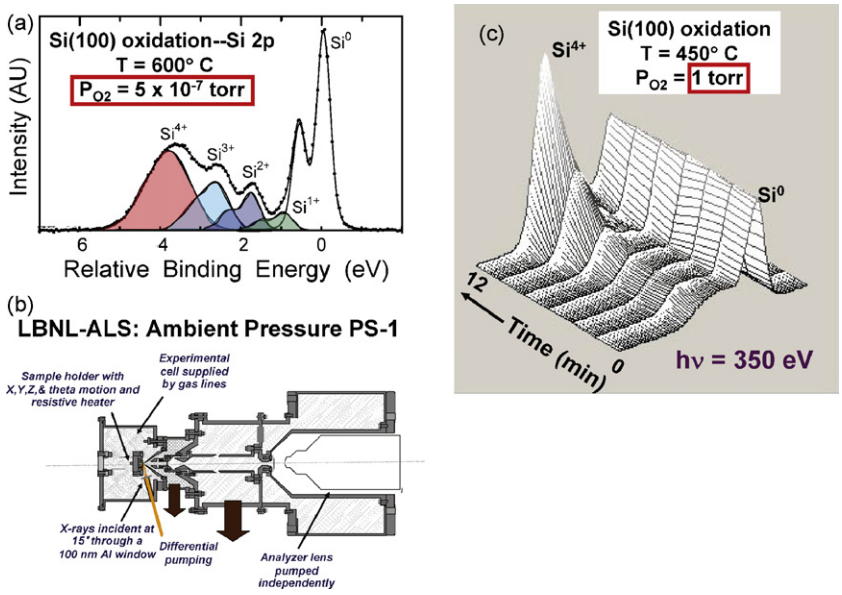

Fig. 32. (a) High-resolution Si 2p spectrum from a Si(0 0 1) surface that has been oxidized at 600 °C and an ambient pressure of 5×10^{-7} Torr (from Ref. [149]) (b) A spectrometer configuration in which the sample region is isolated from the radiation source by a thin window and from the spectrometer by differential pumping so as to permit ambient pressures up to 5–10 Torr (from Ref. [82]). (c) A series of Si 2p spectra taken at about 1 min intervals during the oxidation of Si(0 0 1) at 450 °C and an ambient pressure of 1 Torr (from Ref. [150]).

to the processing conditions used in the semiconductor industry [150]. Spectra here were recorded every 8 s, but are finally shown as binned in 1-min intervals for this plot. The SiO_2 thickness range covered is 0–25 Å. More detailed analysis of this data as shown in Fig. 33 indicates a clear division of the reaction rates into an initial rapid regime and a much slower quasi-saturated regime, with a break point between them that occurs when the SiO_2 is about 5–15 Å thick, depending on the ambient pressure. Current models for the reaction kinetics of this process do not describe this regime of thicknesses that is now crucially important in devices [150].

In another illustrative example of the power of ambient pressure XPS, it has recently been used to study the distribution of ions at the surface of an aqueous solution by measuring the intensity ratios of alkali and halide ions as a function of pressure (by going up to the point of deliquescence on a solid alkali halide surface) and photon energy (by varying the degree of surface sensitivity) [147]. Some of these results are summarized in Fig. 34. For KBr, with excitation at a more-surface-sensitive energy of 200 eV, Fig. 34(a) shows that

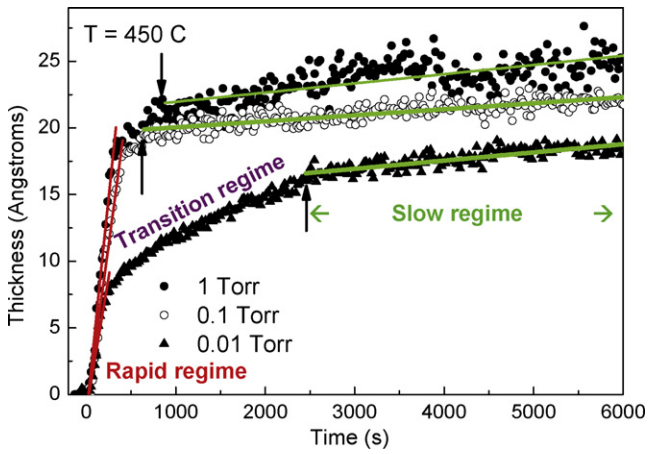

Fig. 33. Application of ambient pressure XPS to the time-dependent growth of SiO_2 on Si(0 0 1) at 450 °C and various pressures, as derived from the relative intensities of the Si^{4+} and Si^{0} peaks in spectra such as those in Fig. 32(c) (from Ref. [150])

the Br/K intensity ratio is constant until the deliquescence point is reached, at which it abruptly jumps by a factor of two due to an enhancement of the Br concentration at the surface. In Fig. 34(b), the effect of varying photon energy on this ratio at deliquescence is shown, and these results verify that, for either KBr or KI, the halide ion tends to segregate to a liquid surface, with the effect being more pronounced for the larger iodide ion. These results are also consistent with the expectations of molecular dynamics calculations. Such studies of liquid surfaces, either in the static high-pressure ambient mode described here [83], or via photoemission from a liquid jet as reviewed elsewhere [9], open the way to many studies of relevance to environmental and life sciences.

As one additional aspect of ambient pressure XPS studies, one can also look forward to being able to resolve band structures and molecular levels in the near-surface region as a function of time and gas exposure. For example, Fig. 35 shows a detector image like those in Fig. 1(c), and 27–30, but for an HOPG graphite surface in the presence of 0.2 Torr of CO at a photon energy of 120 eV [151]. The dispersing band states of the graphite are clearly seen as curved intensity profiles, together with the non-dispersing localized molecular states in the gas near the surface, and perhaps also adsorbed on the surface, which appear as flat lines. Thus, following the electronic structure of both substrate and adsorbate in detail during a surface chemical reaction should be possible. It is also clear that, if a core-level intensity is monitored in a situation such as that in Fig. 35, diffraction-produced modulations of intensity will be observable in the detector image; these would provide additional atomic structure information from XPD to the ambient pressure photoemission experiment, and represent another obvious direction for future experiments.

Looking ahead concerning ambient pressure XPS, we can expect that much higher pressures into the 15–20 Torr regime, shorter timescales in the millisecond range, and significantly better energy resolutions than those in Figs. 32(c) and 34(a) should be possible with a combination of better differential pumping, higher throughput spectrometers, brighter radiation sources, and more efficient multichannel detectors for photoelectrons that are under development [43]. Reaching 18 Torr is a particularly important goal, as this is the vapor pressure of water at room temperature. Being

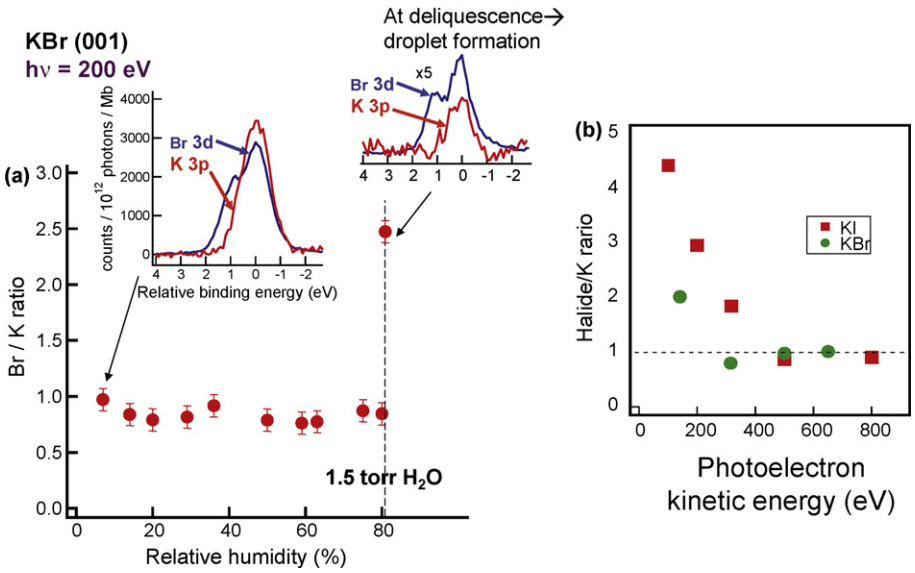

Fig. 34. Application of ambient pressure XPS to the concentration profiles at the surfaces of ionic solutions, in particular aqueous KBr and KI. (a) The variation of the normalized Br/K ratio obtained from a surface of KBr excited at 200 eV photon energy as a function of ambient water humidity, which varies from zero to the deliquescence point at which an aqueous solution forms. The insets show actual XPS spectra at the two end points. (b) The halide/K ratio for KBr and KI, as a function of the incident photon energy, or equivalently the degree of surface sensitivity (from Ref. [147]).

able to measure at such conditions would open up numerous applications in environmental and biological science. Subsequent generations of differentially pumped spectrometers beyond that in Fig. 32 are already operating and in fact beginning to be commercially available; these include, e.g. up to four stages of differential pumping. Using standing wave excitation in such ambient pressure experiments would also permit more selectively looking at the near-surface region, in particular at the depth profiles of species just below the surface and in the gas phase just above the surface. Finally, since one limit on pressure has to do with attenuation of the photoelectrons by inelastic scattering, using hard X-rays for excitation should permit operating at higher pressures, another advantage of this other new direction in XPS that has been discussed here.

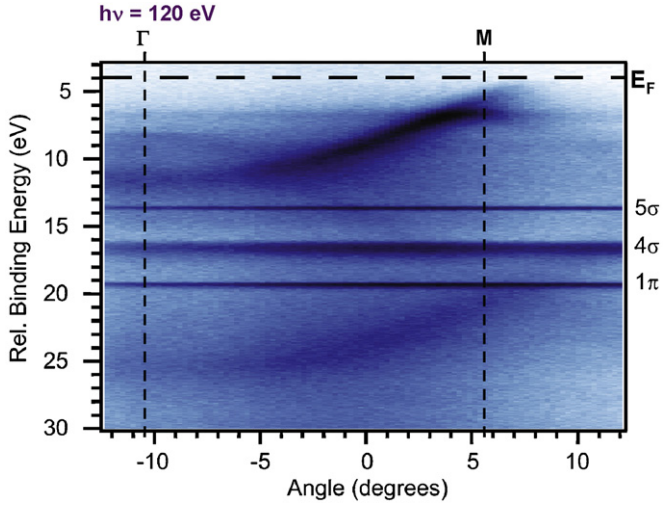

Fig. 35. Observation of bands and molecular levels in an ambient pressure XPS experiment. A sample of HOPG graphite was exposed to 120 eV photons in the presence of 0.2 Torr of CO. The resulting detector image of binding energy vs emission angle (cf. Fig. 1(c)) exhibits both the dispersing bands of graphite near the surface and the non-dispersing states of adsorbed and gas-phase CO (from Ref. [151]).

12. Concluding remarks

In this article, I have attempted to both overview the basic phenomena in XPS, in particular as discussed in more detail in other articles of this issue, and to consider several of its forefront areas for future development and exploitation, from those related to surface and interface analysis, which is in some sense the "bread and butter" application of the technique, to those related to more subtle measurements of surface and bulk electronic structure (densities of states and bands), magnetic properties, and time-resolved processes, including chemical kinetics. There are indeed many exciting new directions for XPS, with the promise that one will be able in the future to carry out experiments in which the properties of a given nanoscale sample are measured as a function of three spatial dimensions (e.g. via some combination of microscopy, variable photon energy into the multi-keV regime, and standing wave excitation), of time (via short-pulse sources and/or next generation ambient pressure systems), and of the electron spin (via next generation detectors). One can say that the "complete photoemission experiment" is within reach. It seems certain that Einstein would be pleased to see what has become of the humble photoelectric effect.

Acknowledgements

The work in the author's group described in this article was supported by the Director, Office of Science, Office of Basic Energy Sciences, Materials Sciences and Engineering Division, of the U.S. Department of Energy under Contract Number DE-AC02-05CH11231. The author also gratefully acknowledges the support of the Helmholtz Foundation, the Humboldt Foundation, and the Jülich Research Center. Various collaborators have also graciously permitted the inclusion of as yet unpublished results. Thanks also goes to A. Gray and two conscientious reviewers for helpful suggestions concerning this manuscript.

References

[1] A. Einstein, Ann. Phys. 17 (1905) 132.
[2] J.G. Jenkin, R.C.G. Leckey, J. Liesegang, J. Electron Spectrosc. Relat. Phenom. 12 (1977) 1;

J.G. Jenkin, R.C.G. Leckey, J. Liesegang, J. Electron Spectrosc. Relat. Phenom. 14 (1978) 477.
[3] K. Siegbahn, C. Nordling, A. Fahlman, K. Hamrin, J. Hedman, R. Nordberg, C. Johansson, T. Bergmark, S.-E. Karlsson, I. Lindgren, B. Lindberg, Atomic, molecular and solid-state structure studied by means of electron spectroscopy, Nova Acta Regiae Soc. Sci. Ups. 20.1-282, Almqvist and Wiksells, 1967.
[4] K. Siegbahn, C. Nordling, G. Johansson, J. Hedman, P.-F. Heden, K. Hamrin, U. Gelius, T. Bergmark, L.O. Werme, R. Manne, Y. Baer, ESCA Applied to Free Molecules, North-Holland, Amsterdam, The Netherlands, 1969, 200 pp.
[5] C.S. Fadley, in: C.R. Brundle, A.D. Baker (Eds.), Electron Spectroscopy: Theory, Techniques, and Applications, vol. II, Academic Press, London, 1978, Chap. 1; available also as a reprint at: http://www.physics.ucdavis.edu/fadleygroup/.
[6] S. Hűfner, Photoelectron Spectroscopy: Principles and Applications, 3rd ed., Springer, Berlin, 2003.
[7] C.S. Fadley, Surf. Interface Anal. 40 (2008) 1579.
[8] C.S. Fadley, Nucl. Inst. Methods A 601 (2009) 8.
[9] (a) H. Siegbahn, S. Svensson, M. Lundholm, J. Electron Spectrosc. Relat. Phenom. 24 (1981) 205;
(b) O.A. Baschenko, F. Bökman, O. Bohman, H. Siegbahn, J. Electron Spectrosc. Relat. Phenom. 62 (1993) 317–334;
(c) B. Winter, E.F. Aziz, U. Hergenhahn, M. Faubel, I.V. Hertel, J. Chem. Phys. 126 (2007) 124504;
(d) B. Winter, Nucl. Inst. Methods A: Accel. Spectrom. 601 (2009) 139.
[10] Y. Takata, Y. Kayanuma, M. Yabashi, K. Tamasaku, Y. Nishino, D. Miwa, Y. Harada, K. Horiba, S. Shin, S. Tanaka, K. Ikenaga, K. Kobayashi, Y. Senba, H. Ohashi, T. Ishikawa, Phys. Rev. B 75 (2007) 233404;
Y. Takata, Y. Kayanuma, S. Oshima, S. Tanaka, M. Yabashi, K. Tamasaku, Y. Nishino, M. Matsunami, R. Eguchi, A. Chainani, M. Oura, T. Takeuchi, Y. Senba, H. Ohashi, S. Shin, T. Ishikawa, Phys. Rev. Lett. 101 (2008) 137601.
[11] S. Suzer (Ed.), J. Electron Spectrosc. Relat. Phenom. 176 (1–3) (2010) (issue dedicated to charging effects in XPS).
[12] X.J. Zhou, B. Wannberg, W.L. Yang, V. Brouet, Z. Sun, J.F. Douglas, D. Dessau, Z. Hussain, Z.-X. Shen, J. Electron Spectrosc. Relat. Phenom. 142 (2005) 27.
[13] A. Pietzsch, A. Föhlisch, M. Beye, M. Deppe, F. Hennies, M. Nagasono, E. Suljoti, W. Wurth, C. Gahl, K. Döbrich, A. Melnikov, New J. Phys. 10 (2008) 033004.
[14] S. Hellmann, K. Rossnagel, M. Marczynski-Bühlow, L. Kipp, Phys. Rev. B 79 (2009) 035402.
[15] K. Tiedtke, et al., New J. Phys. 11 (2009) 023029.
[16] S.M. Goldberg, C.S. Fadley, S. Kono, J. Electron Spectrosc. Relat. Phenom. 21 (1981) 285.
[17] C.S. Fadley, S.-H. Yang, B.S. Mun, J. Garcia de Abajo, in: W. Schattke, M.A. Van Hove (Eds.), Solid-State Photoemission and Related Methods: Theory and Experiment, Wiley–VCH Verlag, Berlin GmbH, 2003.
[18] J.-J. Yeh, I. Lindau, Atomic subshell photoionization cross sections and asymmetry parameters: $1 < Z < 103$, Atom Data Nucl. Data Tables 32 (1) (1985), with these results also available in graphical form at: http://ulisse.elettra.trieste.it/services/elements/WebElements.html.
[19] P.H. Scofield, Theoretical photoionization cross sections from 1 to 1500 keV, Lawrence Livermore Laboratory Report UCRL-51326, 1973, out of print, but also available at: http://www.physics.ucdavis.edu/fadleygroup/Scofield.CrossSections.UCRL51326.pdf.
[20] M.B. Trzhaskovskaya, V.I. Nefedov, V.G. Yarzhemsky, Atom. Data Nucl. Data Tables 77 (2001) 97;
M.B. Trzhaskovskaya, V.I. Nefedov, V.G. Yarzhemsky, Atom. Data Nucl. Data Tables 82 (2002) 257;
M.B. Trzhaskovskaya, V.K. Nikulin, V.I. Nefedov, V.G. Yarzhemsky, Atom. Data Nucl. Data Tables 92 (2006) 245.
[21] The NIST Electron Inelastic-Mean-Free-Path Database (http://www.nist.gov/srd/nist71.htm) and the NIST Electron Effective-Attenuation-Length Database (http://www.nist.gov/srd/nist82.htm), which is available at no charge.
[22] C.J. Powell, A. Jablonski, I.S. Tilinin, S. Tanuma, D.R. Penn, J. Electron Spectrosc. Relat. Phenom. 98 (1999) 1.
[23] S. Tanuma, C.J. Powell, D.R. Penn, Surf. Interface Anal. 37 (2005) 1;
S. Tanuma, C.J. Powell, D.R. Penn, Calculations of electron inelastic mean free paths. IX. Data for 41 elemental solids over the 50 eV to 30 keV range, to be published.
[24] M.P. Seah, S.J. Spencer, J. Electron Spectrosc. Relat. Phenom. 151 (2006) 178.
[25] M.O. Krause, Phys. Rev. 177 (1969) 151.
[26] R. Guillemin, O. Hemmers, D.W. Lindle, S.T. Manson, Radiat. Phys. Chem. 75 (2006) 2258.
[27] A. Jablonski, C.J. Powell, Surf. Int. Anal. 20 (1993) 771.
[28] C.S. Fadley, Prog. Surf. Sci. 16 (1984) 275;
A. Herrera-Gomez, J.T. Grant, P.J. Cumpson, M. Jenko, F.S. Aguirre-Tostado, C.R. Brundle, T. Conard, G. Conti, C.S. Fadley, J. Fulghum, K. Kobayashi, L. Köver, H. Nohira, R.L. Opila, S. Oswald, R.W. Paynter, R.M. Wallace, W.S.M. Werner, J. Wolstenholmer, Surf. Interf. Anal. 41 (2009) 840–857 (summary of the 47th IUVSTA Workshop on Angle-Resolved XPS, Riviera Maya, Mexico, March 2007).
[29] (a) The SESSA program by W. Smekal, W. S. M. Werner, C.J. Powell, and described in Surf. Interf. Anal. 37, 1059 (2005), includes all of the effects mentioned here except surface refraction due to V_0 and can be used over a very broad range of photon energies. Further information on this is available at: http://www.nist.gov/srd/nist100.htm and http://www.iap.tuwien.ac.at/~werner/sessa.html.;
(b) An alternative program emphasizing the exact shape of spectra as produced by inelastic scattering is QUASES™ by S. Tougaard, with information on this available at: http://www.quases.com/.
[30] (a) B.L. Henke, Phys. Rev A 6 (1972) 74;
(b) J. Chester, T. Jach, S. Thurgate, J. Vac. Sci. Technol. B 11 (1993) 1609;
(c) J. Kawai, S. Hayakawa, Y. Kitajima, K. Maeda, Y. Gohshi, J. Electron Spectrosc. Relat. Phenom. 76 (1995) 313;
(d) E. Landree, T. Jach, D. Brady, A. Karemcheti, J. Canterbury, W. Chism, A.C. Diebold, in: D.G. Seiler, A.C. Diebold, T.J. Shaffner, R. McDonald, W.M. Bullis, P.J. Smith, E.M. Secula (Eds.), Proceedings of the 2000 International Conference on Characterization and Metrology for ULSI Technology, American Institute of Physics, CP550, 2001, pp. 159–163.
[31] D.P. Woodruff, Rep. Prog. Phys. 68 (2005) 743.
[32] J.C. Woicik, E.J. Nelson, D. Heskett, J. Warner, L.E. Berman, B.A. Karlin, I.A. Vartanyants, Phys. Rev. 64 (2001) 125115.
[33] S.-H. Yang, B.S. Mun, N. Mannella, S.-K. Kim, J.B. Kortright, J. Underwood, F. Salmassi, E. Arenholz, A. Young, Z. Hussain, M.A. Van Hove, C.S. Fadley, J. Phys. Condens. Matter 14 (2002) L406.
[34] N. Mårtensson, P. Baltzer, P.A. Brühwiler, J.-O. Forsell, A. Nilsson, A. Stenborg, B. Wannberg, J. Electron Spectrosc. Relat. Phenom. 70 (1994) 117.
[35] E. Bauer, C. Koziol, G. Lilienkamp, T. Schmidt, J. Electron Spectrosc. Relat. Phenom. 84 (1997) 201.
[36] G. Schönhense, H.J. Elmers, S.A. Nepijko, C.M. Schneider, Adv. Imaging Electron Phys. 142 (2006) 160.
[37] A. Barinova, P. Dudina, L. Gregorattia, A. Locatellia, T.O. Menteşa, M.Á. Niñoa, M. Kiskinova, Nucl. Instrum. Methods A 601 (2009) 195.
[38] T. Wakita., T. Taniuchi, K. Ono, M. Suzuki, N. Kawamura, M. Takagaki, H. Miyagawa, F. Guo, T. Nakamura, T. Muro, H. Akinaga, T. Yokoyay, M. Oshima, K. Kobayashi, Jpn. J. Appl. Phys. 45 (2006) 1886.
[39] T. Kinoshita, E. Ikenaga, J.J. Kim, S. Ueda, M. Kobata, J.R. Harries, K. Shimada, A. Ino, K. Tamasaku, Y. Nishino, T. Ishikawa, K. Kobayashi, W. Drube, C. Kunz, Surf. Sci. 601 (2007) 4754.
[40] M.P. Seah, I.S. Gilmore, S.J. Spencer, J. Electron Spectrosc. Relat. Phenom. 104 (1999) 73.
[41] N. Mannella, S. Marchesini, A.W. Kaya, A. Nambu, T. Gresch, S.-H. Yang, B.S. Mun, J.M. Bussat, A. Rosenhahn, C.S. Fadley, J. Electron Spectrosc. Relat. Phenom. 141 (2004) 45.
[42] A.W. Kay, F.J. Garcia de Abajo, S.-H. Yang, E. Arenholz, B.S. Mun, N. Mannella, Z. Hussain, M.A. Van Hove, C.S. Fadley, Phys. Rev. B 63 (2001) 115119 (and earlier references therein).
[43] J.-M. Bussat, C.S. Fadley, B.A. Ludewigt, G.J. Meddeler, A. Nambu, M. Press, H. Spieler, B. Turko, M. West, G.J. Zizka, IEEE Trans. Nucl. Sci. 51 (2004) 2341.
[44] The multiple scattering program EDAC due to J. Garcia de Abajo for calculating photoelectron diffraction is available at: http://csic.sw.ehu.es/jga/software/edac/index.html, with the methodology behind it described in F.J. Garcia de Abajo, M.A. Van Hove, C.S. Fadley, Phys. Rev. B 63 (2001) 075404.
[45] C.S. Fadley, in: R.Z. Bachrach (Ed.), Synchrotron Radiation Research: Advances in Surface and Interface Science, Plenum Press, New York, 1992.
[46] S. Hagstrom, C. Nordling, K. Siegbahn, Phys. Lett. 9 (1964) 235.
[47] S.B. Hagstrom, Obituary of Kai Siegbahn, Phys. Today (November) (2008) 74.
[48] J. Hedman, P.F. Hedén, C. Nordling, K. Siegbahn, Phys. Lett. 29A (1969) 178.
[49] C.S. Fadley, D.A. Shirley, A.J. Freeman, P.S. Bagus, J.V. Mallow, Phys. Rev. Lett. 29 (1969) 1397;
C.S. Fadley, D.A. Shirley, Phys. Rev. A 2 (1970) 1109.
[50] F. De Groot, A. Kotani, Core Level Spectroscopy of Solids, CRC Press, Boca Raton, FL, 2008, Together with a user friendly program for calculating spectrum for some cases. http://www.anorg.chem.uu.nl/people/staff/FrankdeGroot/multiplet1.htm.
[51] K.S. Kim, Phys. Rev. B 11 (1975) 2177.
[52] P.H. Citrin, P. Eisenberger, G. Wertheim, Phys. Rev. Lett. 33 (1974) 965.
[53] A. Föhlisch, J. Hasselström, O. Karis, D. Menzel, N. Mårtensson, A. Nilsson, J. Electron Spectrosc. Relat. Phenom. 101–103 (1999) 303.
[54] U. Hergenhahn, J. Phys. B: Atom. Mol. Opt. Phys. 37 (2004) R89.
[55] K. Siegbahn, U. Gelius, H. Siegbahn, E. Olson, Phys. Lett. 32A (1970) 221.
[56] S.Å.L. Bergstrom, C.S. Fadley, Phys. Lett. 35A (1970) 375.
[57] C.S. Fadley, M.A. Van Hove, A. Kaduwela, S. Omori, L. Zhao, S. Marchesini, J. Phys. Condens. Matter 13 (2001) 10517 (and earlier references therein).
[58] (a) C. Westphal, J. Bansmann, M. Getzlaff, G. Schönhense, Phys. Rev. Lett. 63 (1989) 151;
(b) H. Daimon, T. Nakatani, S. Imada, S. Suga, Y. Kagoshima, T. Miyahara, Jpn. J. Appl. Phys. 32 (1993) L1480;
(c) A.P. Kaduwela, H. Xiao, S. Thevuthasan, C.S. Fadley, M.A. Van Hove, Phys. Rev. B 52 (1995) 14927.
[59] T. Nakatani, T. Matsushita, Y. Miyatake, T. Nohno, A. Kobayashi, K. Fukumoto, S. Okamoto, A. Nakamoto, F. Matsui, K. Hattori, M. Kotsugi, Y. Saitoh, S. Suga, H. Daimon, Prog. Surf. Sci. 71 (2003) 217.
[60] L. Baumgarten, C.M. Schneider, H. Petersen, F. Schäfers, J. Kirschner, Phys. Rev. Lett. 65 (1990) 492.
[61] S. Ueda, H. Tanaka, J. Takaobushi, E. Ikenaga, J.-J. Kim3, M. Kobata, T. Kawai, H. Osawa, N. Kawamura, M. Suzuki, K. Kobayashi, Appl. Phys. Express 1 (2008) 077003.
[62] J.G. Menchero, Phys. Rev. B 57 (1998) 993.
[63] R. Hashimoto, A. Chikamatsu, H. Kumigashira, M. Oshima, N. Nakagawa, T. Ohnishi, M. Lippmaa, H. Wadati, A. Fujimori, K. Ono, M. Kawasaki, H. Koinuma, J. Electron Spectrosc. Relat. Phenom. 144–147 (2005) 479.

[64] P. Le Fèvre, H. Magnan, D. Chandesris, J. Jupille, S. Bourgeois, A. Barbier, W. Drube, T. Uozumi, A. Kotani, Nucl. Inst. Methods Phys. Res. A 547 (2005) 176.
[65] P. Krüger, S. Bourgeois, B. Domenichini, H. Magnan, D. Chandesris, P. Le Fèvre, L. Floreano, A. Cossaro, A. Verdini, A. Morgante, Surf. Sci. 601 (2007) 3952; H. Magnan, P. Le Fèvre, D. Chandesris, P. Krüger, S. Bourgeois, B. Domenichini, A. Verdini, L. Floreano, A. Morgante, Phys. Rev. B 81 (2010) 085121.
[66] L. Plucinski, J. Minár, B.C. Sell, J. Braun, H. Ebert, C.M. Schneider, C.S. Fadley, Phys. Rev. B 78 (2008) 035108.
[67] C.S. Fadley, D.A. Shirley, Phys. Rev. Lett. 21 (1968) 980; C.S. Fadley, D.A. Shirley, NBS J. Res. 74A (1970) 543.
[68] Y. Baer, P.-F. Hedén, J. Hedman, M. Klasson, C. Nordling, K. Siegbahn, Solid State Commun. 8 (1970) 517.
[69] M.A. Vicente Alvarez, H. Ascolani, G. Zampieri, Phys. Rev. B 54 (1996) 14703.
[70] F.-C. Tang, X. Zhang, F.B. Dunning, G.K. Walters, Rev. Sci. Instrum. 59 (1988) 504.
[71] R. Frömter, H.P. Oepen, J. Kirschner, Appl. Phys. A 76 (2003) 869–871.
[72] F.U. Hillebrecht, R.M. Jungblut, L. Wiebusch, C. Roth, H.B. Rose, D. Knabben, C. Bethke, N.B. Weber, S. Manderla, U. Rosowski, E. Kisker, Rev. Sci. Instrum. 73 (2002) 1229; J. Graf, C. Jozwiak, A.K. Schmid, Z. Hussain, A. Lanzara, Phys. Rev. B 71 (2005) 144429; T. Okuda, Y. Takeich, A. Harasawa, I. Matsuda, T. Kinoshita, A. Kakizaki, Eur. Phys. J. Spec. Top. 169 (2009) 181–185.
[73] G. Busch, M. Campagna, P. Cotti, H.C. Siegmann, Phys. Rev. Lett. 22 (1969) 597.
[74] H.-J. Kim, E. Vescovo, S. Heinze, S. Blügel, Surf. Sci. 478 (2001) 193.
[75] J. Zegenhagen, C. Kunz (Eds.), Nucl. Inst. Methods A 547 (2005) (special journal issue dedicated to photoemission with hard X-rays).
[76] Programs and abstract archives from three recent hard X-ray photoemission workshops: http://haxpes2006.spring8.or.jp/program.html; http://ssg.als.lbl.gov/ssgdirectory/fedorov/workshops/index.html; http://www.nsls.bnl.gov/newsroom/events/workshops/2009/haxpes/.
[77] K. Kobayashi, Nucl. Inst. Methods A 601 (2009) 32.
[78] R.X. Ynzunza, R. Denecke, F.J. Palomares, J. Morais, E.D. Tober, Z. Wang, F.J. Garcia de Abajo, J. Liesegang, Z. Hussain, M.A. Van Hove, C.S. Fadley, Surf. Sci. 69 (2000) 459.
[79] M. Pickel, A.B. Schmidt, M. Donath, M. Weinelt, Surf. Sci. 600 (2006) 4176.
[80] F. Banfi, C. Giannetti, G. Ferrini, G. Galimberti, S. Pagliara, D. Fausti, F. Parmigiani, Phys. Rev. Lett. 94 (2005) 037601.
[81] A. Landers, T. Weber, I. Ali, A. Cassimi, M. Hattass, O. Jagutzki, A. Nauert, T. Osipov, A. Staudte, M.H. Prior, H. Schmidt-Böcking, C.L. Cocke, R. Dörner, Phys. Rev. Lett. 87 (2001) 013002.
[82] D.F. Ogletree, H. Bluhm, G. Lebedev, C.S. Fadley, Z. Hussain, M. Salmeron, Rev. Sci. Inst. 73 (2002) 3872.
[83] M.B. Salmeron, R. Schlögl, Surf. Sci. Rep. 63 (2008) 169–199.
[84] N. Mannella, A. Rosenhahn, C.H. Booth, S. Marchesini, B.S. Mun, S.-H. Yang, K. Ibrahim, Y. Tomioka, C.S. Fadley, Phys. Rev. Lett. 92 (2004) 166401.
[85] N. Mannella, C.H. Booth, A. Rosenhahn, B.C. Sell, A. Nambu, S. Marchesini, B.S. Mun, S.-H. Yang, M. Watanabe, K. Ibrahim, E. Arenholz, A. Young, J. Guo, Y. Tomioka, C.S. Fadley, Phys. Rev. B 77 (2008) 125134.
[86] F. Offi, N. Mannella, T. Pardini, G. Panaccione, A. Fondacaro, P. Torelli, S. Huotari, M.W. West, J.W. Mitchell, C.S. Fadley, Phys. Rev. B 77 (2008) 174422.
[87] K. Horiba, M. Taguchi, A. Chainani, Y. Takata, E. Ikenaga, D. Miwa, Y. Nishino, K. Tamasaku, M. Awaji, A. Takeuchi, M. Yabashi, H. Namatame, M. Taniguchi, H. Kumigashira, M. Oshima, M. Lippmaa, M. Kawasaki, H. Koinuma, K. Kobayashi, T. Ishikawa, S. Shin, Phys. Rev. Lett. 93 (2004) 236401.
[88] H. Tanaka, Y. Takata, K. Horiba, M. Taguchi, A. Chainani, S. Shin, D. Miwa, K. Tamasaku, Y. Nishino, T. Ishikawa, E. Ikenaga, M. Awaji, A. Takeuchi, T. Kawai, K. Kobayashi, Phys. Rev. B 73 (2006) 094403.
[89] M. VanVeenendaal, Phys. Rev. B 74 (2006) 085118.
[90] F. Offi, T. Pardini, G. Panaccione, C.S. Fadley, unpublished results from the ESRF VOLPE facility.
[91] Y.J. Kim, C. Westphal, R.X. Ynzunza, Z. Wang, H.C. Galloway, M. Salmeron, M.A. Van Hove, C.S. Fadley, Surf. Sci. 416 (1998) 68.
[92] Y.-N. Sun, Z.-H. Qin, M. Lewandowski, E. Carrasco, M. Sterrer, S. Shaikhutdinov, H.-J. Freund, J. Catal. 266 (2009) 359.
[93] M. Treier, P. Ruffieux, R. Fasel, F. Nolting, S. Yang, L. Dunsch, T. Greber, Phys. Rev. B 80 (2009) 081403.
[94] T. Greber, J. Wider, E. Wetli, J. Osterwalder, Phys. Rev. Lett. 81 (1998) 1654.
[95] J. Osterwalder, A. Tamai, W. Auwarter, M.P. Allan, T. Greber, Chimia 60 (2006) A795 (And earlier references therein).
[96] D.P. Woodruff, Surf. Sci. Rep. 62 (2007) 1.
[97] A. Winkelmann, C.S. Fadley, F.J. Garcia de Abajo, New J. Phys. 10 (2008) 113002.
[98] S. Ueda, A. Winkelmann, C. Papp, L. Plucinski, A. Gray, B. Balke, K. Kobayashi, C.S. Fadley, unpublished results from SPring8 beamline 15XU.
[99] M. Kobata, Igor Píš, H. Iwai, H. Yamazui, H.Takahashi, M. Suzuki, H. Matsuda, H. Daimon, K. Kobayashi, to be published.
[100] O.M. Käuttel, R.G. Agostino, R. Fasel, J. Osterwalder, L. Schlapbach, Surf. Sci. 312 (1994) 131.
[101] A. Szöke, in: D.T. Attwood, J. Boker (Eds.), AIP Conf. Proc. Number 147, AIP, New York, 1986, p. 361.
[102] S. Omori, Y. Nihei, E. Rotenberg, J.D. Denlinger, S. Marchesini, S.D. Kevan, B.P. Tonner, M.A. Van Hove, C.S. Fadley, Phys. Rev. Lett. 88 (2002) 5504.
[103] T. Greber, J. Phys.: Condens. Matter 13 (2001) 10561.
[104] M.J. Bedzyk, Encyclopedia Condens. Matter Phys. 6 (2005) 330 (And earlier references therein).
[105] S.-H. Yang, B.S. Mun, C.S. Fadley, Synchrotron Radiat. News 24 (2004) 17.
[106] S.-H. Yang, B.C. Sell, C.S. Fadley, J. Appl. Phys. 103 (2008) 07C519.
[107] S.-H. Yang, specially written computer program for standing-wave photoemission from multilayer structures, available on request, and to be published.
[108] S. Döring, F. Schonbohm, D. Weier, F. Lehmkuhler, U. Berges, M. Tolan, C.S. Fadley, C. Westphal, J. Appl. Phys. 106 (2009) 124906.
[109] B.C. Sell, Ph.D. Thesis, UC Davis, 2007.; B.C. Sell, S.-H. Yang, C.S. Fadley, unpublished results from Advanced Light Source beamline 4.0.2.
[110] S.-H. Yang, B.S. Mun, N. Mannella, A. Nambu, B.C. Sell, S.B. Ritchey, F. Salmassi, S.S.P. Parkin, C.S. Fadley, J. Phys.: Condens. Matter 18 (2006) L259.
[111] B. Klingenberg, F. Grellner, D. Borgmann, G. Wedler, Surf. Sci. 283 (1997) 13.
[112] B. Balke, C. Papp, S. Döring, U. Berges, S.H. Yang, B.C. Sell, D. Buergler, J.B. Kortright, C.M. Schneider, C. Westphal, C.S. Fadley, unpublished results from Advanced Light Source beamline 4.0.2.
[113] C.S. Fadley, Nucl. Inst. Methods A 547 (2005) 24.
[114] S. Döring, F. Schonbohm, U. Berges, C. Papp, B. Balke, M. Gorgoi, D. Buergler, C. Schneider, C.S. Fadley, unpublished results from the BESSY HIKE facility.
[115] C. Papp, B. Balke, S. Ueda, H. Yoshikawa, Y. Yamashita, S.L. He, C. Sakai, K. Kobayashi, D. Buergler, C. Schneider, C.S. Fadley, unpublished results from SPring8, beamline 15XU.
[116] C. Papp, B. Balke, S. Ueda, H. Yoshikawa, Y. Yamashita, K. Kobayashi, G. Conti, C.S. Fadley, unpublished results from Spring8 beamline 15XU.
[117] F. Kronast, R. Ovsyannikov, A. Kaiser, C. Wiemann, S.-H. Yang, D.E. Bürgler, R. Schreiber, F. Salmassi, P. Fischer, H.A. Dürr, C.M. Schneider, W. Eberhardt, C.S. Fadley, Appl. Phys. Lett. 93 (2008) 243116.
[118] A video of standing wave motion in a photoelectron microscope is available at: http://www.physics.ucdavis.edu/fadleygroup/.
[119] F. Kronast, C. Papp, A. Kaiser, C. Wiemann, A. Gray, S. Cramm, B. Balke, R. Schreiber, D. Buergler, C. Schneider, unpublished results from BESSY spin-polarized photoelectron microscope.
[120] A. Gray, S.-H. Yang, C.S. Fadley, unpublished results.
[121] A. Gupta, N. Darowski, I. Zizak, C. Meneghini, G. Schumacher, A. Erko, Spectrochim. Acta 62 (2007) 622.
[122] Z. Hussain, C.S. Fadley, S. Kono, L.F. Wagner, Phys. Rev. B 22 (1980) 3750; R.C. White, C.S. Fadley, M. Sagurton, Z. Hussain, Phys. Rev. B 34 (1986) 5226.
[123] K. Siegbahn, private communication, 2003.
[124] Y. Takata, private communication, 2006.
[125] Z. Yin, W.E. Pickett, unpublished results for Au.
[126] B. Nielsen, Z. Li, S. Lizzit, A. Goldoni, P. Hoffmann, J. Phys.: Condens. Matter 15 (2003) 6919 (and references therein).
[127] A. Yamasaki, A. Sekiyama, S. Imada, M. Tsunekawa, A. Higashiya, A. Shigemoto, S. Suga, Nucl. Inst. Methods Phys. Res. A 547 (2005) 136.
[128] M. Yano, A. Sekiyama, H. Fujiwara, T. Saita, S. Imada, T. Muro, Y. Onuki, S. Suga, Phys. Rev. Lett. 98 (2007) 036405 (and references therein).
[129] N. Kamakura, Y. Takata, T. Tokushima, Y. Harada, A. Chainani, K. Kobayashi, S. Shin, Phys. Rev. B 74 (2006) 045127.
[130] F. Venturini, J. Minar, J. Braun, H. Ebert, N.B. Brookes, Phys. Rev. B 77 (2008) 045126.
[131] J. Braun, Rep. Prog. Phys. 59 (1996) 1267.
[132] C. Papp, J. Minar, L. Plucinski, J. Braun, H. Ebert, C.S. Fadley, unpublished results.
[133] S. Ueda, K. Kobayashi, C. Papp, A. Gray, L. Plucinski, J. Minar, J. Braun, H. Ebert, C.S. Fadley, unpublished results from Spring8 beamline BL15XU.
[134] J. Osterwalder, T. Greber, S. Hüfner, L. Schlapbach, Phys. Rev. Lett. 64 (1990) 2683; G.S. Herman, T.T. Tran, K. Higashiyama, C.S. Fadley, Phys. Rev. Lett. 68 (1992) 1204.
[135] E. Rotenberg, A. Bostwick, private communication, 2005.
[136] L. Plucinski, A. Gray, C.S. Fadley, unpublished results.
[137] T. Schmidt, U. Groh, R. Fink, E. Umbach, Surf. Rev. Lett. 9 (2002) 223.
[138] H. Marchetto, U. Groh, T. Schmidt, R. Fink, H.J. Freund, E. Umbach, Chem. Phys. 178 (2006) 325.
[139] S. Lizzit, G. Zampieri, L. Petaccia, R. Larciprete, P. Lacovig, E.D.L. Rienks, G. Bihlmayer, A. Baraldi, P. Hofmann, http://arxiv.org/abs/1001.4761, submitted to Nat. Mater.
[140] T.D. Thomas, N. Berrah, J. Bozek, T.X. Carroll, J. Hahne, T. Karlsen, E. Kukk, L.J. Sæthre, Phys. Rev. Lett. 82 (1999) 1120.
[141] U. Hergenhahn, O. Kugeler, A. Ru1del, E.E. Rennie, A.M. Bradshaw, J. Phys. Chem. A 105 (2001) 5704.
[142] D. Nordfors, N. Martensson, A. Nilsson, (1986), unpublished results; A. Nilsson, J. Electron Spectrosc. Relat. Phenom 126 (2002) 3 (discussion of Figure 14).
[143] H.J. Ruppender, M. Grunze, C.W. Kong, Surf. Int. Anal. 15 (1990) 245.
[144] A. Baraldi, G. Comelli, S. Lizzit, M. Kiskinova, G. Paolucci, Surf. Sci. Rep. 49 (2003) 169.
[145] R. Denecke, Appl. Phys. A 80 (2005) 977 (and references therein).
[146] H. Bluhm, D. Frank Ogletree, C.S. Fadley, Z. Hussain, M. Salmeron, J. Phys. Condens. Matter 14 (2002) L227.
[147] S. Ghosal, J.C. Hemminger, H. Bluhm, B.S. Mun, E.L.D. Hebenstreit, G. Ketteler, D.F. Ogletree, F.G. Requejo, M. Salmeron, Science 307 (2005) 5709; M.A. Brown, R. D'Auria, I.F.W. Kuo, M.J. Krisch, D.E. Starr, H. Bluhm, D.J. Tobias, J.C. Hemminger, Phys. Chem. Chem. Phys. 10 (2008) 4778.
[148] H. Bluhm, M. Hävecker, A. Knop-Gericke, E. Kleimenov, R. Schlögl, D. Teschner, V.I. Bukhtiyarov, D.F. Ogletree, M.B. Salmeron, J. Phys. Chem. B 108 (2004) 14340.

[149] Y. Enta, Y. Miyanishi, H. Irimachi, M. Niwano, M. Suemitsu, N. Miyamoto, E. Shigemasa, H. Kato, Phys. Rev. B 57 (1998) 6294;
Y. Enta, Y. Miyanishi, H. Irimachi, M. Niwano, M. Suemitsu, N. Miyamoto, E. Shigemasa, H. Kato, J. Vac. Sci. Technol. A 16 (1998) 1716.
[150] Y. Enta, B.S. Mun, Y. Enta, M. Rossi, P.N. Ross, Z. Hussain, C.S. Fadley, K.-S. Lee, S.-K. Kim, Appl. Phys. Lett. 92 (2008) 012110;
M. Rossi, B.S. Mun, Y. Enta, C.S. Fadley, K.S. Lee, S.-K. Kim, H.-J. Shin, Z. Hussain, P.N. Ross Jr., J. Appl. Phys. 103 (2008) 044104.
[151] M.E. Grass, P.G. Karlsson, F. Aksoy, M. Lundqvist, B. Wannberg, B.S. Mun, Z. Liu, Z. Hussain, results from Advanced Light Source beamline 9.3.2, submitted to Rev. Sci. Inst.